Beta-delayed Neutron Emission Spectroscopy in the ^{78}Ni Region and Development of YSO-based Implantation Detector

A Dissertation Presented for the

Doctor of Philosophy

Degree

The University of Tennessee, Knoxville

Maninder Singh

May 2022

© by Maninder Singh, 2022
All Rights Reserved.

It is not the critic who counts; not the man who points out how the strong man stumbles, or where the doer of deeds could have done them better. The credit belongs to the man who is actually in the arena, whose face is marred by dust and sweat and blood; who strives valiantly; who errs, who comes short again and again, because there is no effort without error and shortcoming; but who does actually strive to do the deeds; who knows great enthusiasms, the great devotions; who spends himself in a worthy cause; who at the best knows in the end the triumph of high achievement, and who at the worst, if he fails, at least fails while daring greatly, so that his place shall never be with those cold and timid souls who neither know victory nor defeat.

***********THEODORE ROOSEVELT***********

Acknowledgments

As all good things come to an end, so is the case with my Ph.D. It has been a roller-coaster journey filled with ups and downs. And this would not have been possible without the never-ending love and support of family, friends, and colleagues. I would like to first thank my family (Father: Satnam Singh, Mother: Paramjit Kaur, and Sister: Komal Preet Kaur) for their rock-solid support and love. It would not have been possible without all of it so far away from the homeland. I want to extend my thanks to Dr. Kate Jones-Grzywacz, for listening to me and pointing me in the direction of Dr. Robert K. Grzywacz. I will always be grateful to my adviser Dr. Robert K. Grzywacz for his guidance, professional mentoring, teaching, and constructive criticism throughout my working period. All of it shaped me to be a better professional and researcher.

I want to thank my colleagues, Rin, Shree, and Zhengyu, for helping me with my research projects and keeping the fun quotient alive in me. I want to give a special mention to my friend Larry Hays for his nurturing and unconditional friendship; it has been a blessing to overlap life with him. I want to acknowledge my friend Priya Goyal from India for always listening to my problems and giving solutions. I want to mention Mariah Winslow for her friendship and teaching me the ropes of the American culture. I want to acknowledge the presence of Dr. Cole Woodcox for making time in the USA homelike.

Last but not least, I want to thank Chrisanne Romeo for always looking after me in the department and giving me great advice. This dissertation is a collective effort.

Abstract

Decays of Cu isotopes provide a laboratory to study the properties for nearly doubly-magic nuclei with a significant neutron excess which are also relevant for the r-process models. The beta-decay properties of doubly-magic ^{78}Ni (N=50) are imprinted in the neighboring Cu decay, nuclei with a single proton outside the Z=28 core. The investigated isotopes ^{79,80,81}Cu are strong beta-delayed neutron precursors, suggesting that their decay strength distribution lies above neutron separation energies in ^{79,80,81}Zn daughters.

For decay studies, a segmented scintillator YSO (Y_2SiO_5:Ce doped) based implantation detector was developed at the University of Tennessee, Knoxville. The detector is compact in structure and offers good spatial and timing resolution, crucial for ion-β correlations and time-of-flight (ToF) based β-delayed neutron emission spectroscopy, respectively. The detector was employed as a part of the BRIKEN neutron counter at the Radioactive Isotope Beam Factory (RIBF) at RIKEN Nishina Center in Japan, aiming to measure one- and two-neutron emission probabilities ($P_{n,2n}$) for nuclei around the ^{78}Ni region. Another variant of the detector with a more advanced design was used along with VANDLE (Versatile Array for Neutron Detection at Low Energy) to conduct spectroscopy of β-delayed neutrons in the same region.

Reconstruction of the feeding intensities requires analysis of neutron-gamma cascades, as is suggested by the statistical model. This work reports the first direct measurements of β-decay strength to neutron-unbound states in the decay of ^{81,80,79}Cu. The results from the experiment are compared to shell-model calculations with various sets of single-particle energies and residual interactions. Finally, predictions for ^{78}Ni decay are made based on the model best-describing ^{79}Cu.

Table of Contents

1 Motivation **1**

1.1 Background . . . 1

1.2 Beta Decay Fundamentals . . . 6

1.3 Delayed Neutron Emission . . . 11

1.4 R-process and Nucleosynthesis . . . 12

1.5 Nuclear Shell Structure . . . 15

1.5.1 Shell Evolution of Cu Isotopes . . . 22

1.5.2 Similarity in ^{78}Ni and ^{79}Cu decay . . . 22

1.5.3 Crossing N=50 Shell Gap . . . 24

2 Implantation Detector Development **28**

2.1 Detection of Charged Particles . . . 29

2.2 Neutron Interaction with Materials . . . 31

2.3 YSO-based Implantation Detector . . . 32

2.3.1 Testing . . . 35

2.3.2 YSO Detector for Time-of-Flight Spectroscopy . . . 36

3 Experiments **48**

3.1 Radioactive Isotope Beam Factory (RIBF) at RIKEN . . . 48

3.1.1 BRIKEN Experiment . . . 51

3.2 Neutron Spectroscopy using VANDLE at RIBF, RIKEN . . . 55

3.2.1 Trigger Scheme for the Experiment . . . 56

4 Analysis **63**

4.1 BRIKEN Experiment . . . 63

4.1.1 Half-life Determination . . . 64

4.1.2 Light Quenching in YSO . . . 69

4.2 VANDLE Experiment . . . 73

4.2.1 Particle Identification . . . 73

4.3 YSO . . . 78

4.4 High-resolution Germanium Detectors . . . 81

4.5 Lanthanum Bromide ($LaBr_3$) . . . 91

4.6 VANDLE Analysis . . . 91

4.6.1 Timing . . . 91

4.6.2 Time Calibration . . . 93

4.6.3 Flight-path Correction . . . 97

4.6.4 VANDLE GEANT4 Simulations . . . 98

4.6.5 Response Function . . . 100

4.6.6 Designing Neutron Gate . . . 103

4.6.7 Background Subtraction . . . 104

5 Results **111**

5.1 Beta decay of ^{79,80,81}Cu . . . 111

5.1.1 ^{79}Cu Analysis . . . 111

5.1.2 ^{80}Cu . . . 114

5.1.3 ^{81}Cu . . . 118

6 Discussion **126**

7 Conclusion **137**

Bibliography **140**

Vita **154**

List of Tables

1.1 Possible angluar momentum configuration of neutron-hole 25

2.1 Physical properties of YSO 34

4.1 Sources used for calibrating HPGe detectors 83

4.2 Relative intensity of gamma lines in the decay of ^{84}Ga 88

5.1 Neutron-emitting states and the corresponding neutron transitions 115

5.2 Neutron-emitting states identified in ^{80}Zn 121

5.3 Neutron-emitting states identified in ^{81}Zn 124

6.1 β-decay neutron and proton spin-orbit partners 128

6.2 GT probability ($|M^0_{GT}|^2$) using single particle states. 128

6.3 Neutron and proton single-particle energy states 130

6.4 Neutron and proton single-particle energy states 133

6.5 The possible configurations after the beta-decay of ^{78}Ni to ^{78}Cu 133

List of Figures

1.1 Q_β-S_n for nuclei in the chart of nuclei.. . . . 3
1.2 A schematic showing the decay of a β-delayed neutron precursor 13
1.3 Schematic of the initial population of the daughter nucleus 13
1.4 Nuclei chart showing color-coded regions of stability 14
1.5 Wood-Saxon and square well potential for a nucleus with A = 70 18
1.6 Level scheme of the shell model showing the breaking of degeneracy 18
1.7 Systematics of the 2^+ excitation energy 21
1.8 A graphical demonstration of the monopole interaction between 23
1.9 Systematics of the $5/2^-$ and $3/2^-$ states in odd-even Cu isotopes. 23
1.10 Shell structure of ^{78}Ni showing occupation of neutrons 25
1.11 Shell structure of ^{79}Cu showing occupation of neutrons 26
1.12 Predicted reduced transition probability of GT transitions 27

2.1 A schematic diagram explaining the scintillation 34
2.2 YSO (2" × 2") scintillator with 48 × 48 pixel used for building the detector 39
2.3 The electrical circuit of the Anger logic showing readouts for all 64 40
2.4 Picture of the back of the Vertilon board showing 6 SMB 41
2.5 YSO crystal rotated on the face of the PSPMT highlighting 41
2.6 The response of the PSPMT to the pulser input voltage for five different . . 42
2.7 Range distribution of various ions in YSO. 43
2.8 Continuous slowing down approximation range (CSDA) 44
2.9 The image above shows the YSO crystal and light guide 44
2.10 A graphical depiction of the detector design 45

2.11 Schematic of the setup for YSO timing measurement. 45
2.12 Time difference between the signals having gates 46
2.13 Flat-field image produced using ^{137}Cs source on 46
2.14 Image obtained using a ^{90}Sr source and a 47
2.15 Image obtained using a ^{90}Sr placed at 47

3.1 Layout of the RIBF showing various accelerators 50
3.2 Schematic of the BigRIPS separator 52
3.3 A diagram showing the instrumental setup for the 53
3.4 Particle identification plot for ions stopped in YSO 54
3.5 A diagram depicting the construction of a VANDLE bar 57
3.6 A picture of the experiment hall showing the BRIKEN neutron counter . . . 58
3.7 Photograph showing the site of the experimental setup 59
3.8 Photograph showing the 3D-printed implantation box containing 60
3.9 Selected portion of the nuclei chart, showing the region explored 60
3.10 Division of the 5 YSO signals into low- and high-gain branches 61
3.11 Triggering scheme adopted for the experiment. 62

4.1 A graphical representation of the algorithm devised to identify ion-beta . . . 65
4.2 YSO x-y images of (a) β events and (b) implantation events correlated . . . 65
4.3 Decay of a hypothetical nucleus (X1), capable of β-delayed neutron 66
4.4 Decay curve of ^{74}Co fitted using Bateman Equations 70
4.5 Energy-loss distribution of ^{82}Zn ions in the YSO 70
4.6 a) Correlation between Clovers ($E_{\gamma,clover}$) and the YSO ($E_{channel,YSO}$) 72
4.7 Correlation between calibrated high- and low-gain branches 72
4.8 Energy-loss distribution of ^{82}Zn 74
4.9 Light quenching factors obtained for various isotopes stopped 74
4.10 Implementation of a “cut” in the data 77
4.11 T_{sum} for the sum of one of the plates of PPAC at F3. 77
4.12 Ratio of 5th and 4th anode signal for the MUSIC detector. 79
4.13 Cuts implemented on the data obtained from the MUSIC detector. 79

4.14 Calibrated and cleaned Particle Identification (PID) at the F7 83
4.15 Images of ion and beta position distribution gated on the activity 84
4.16 Distance between the pixels of ion and beta images. 84
4.17 Transformed images to pixel space. 85
4.18 A schematic of the algorithm adopted to achieve ion-beta correlations 85
4.19 Decay curve of ^{74}Co obtained using the transformed 86
4.20 Decay curve of ^{79}Cu fitted using the Bateman Equations 86
4.21 Beta-detection efficiency of the YSO detector for ^{79}Cu 88
4.22 Calibrated HPGe spectrum in singles mode, gated on the decay 89
4.23 Design of a 3D-printed source holder matching the dimensions of the YSO . 89
4.24 Count rate of the background peak during the source measurements. 90
4.25 Measured and simulated efficiency for all source positions. 90
4.26 Comparison of the add-back and singles efficiency of HPGe detectors 92
4.27 Calibrated $LaBr_3$ spectrum gated on ^{83}Ga 92
4.28 T_{diff} distribution for each VANDLE bar after time calibration. 95
4.29 A diagram showing the cause of walk in timing for signals 95
4.30 Gamma flash in ToF spectrum bent right due to time walk. 96
4.31 Walk characteristic of signals from right PMT of a VANDLE bar fitted with 96
4.32 Gamma flash in ToF spectrum straightened after walk-correction 99
4.33 Count rate of the background peak during the source measurements 99
4.34 ToF spectrum of neutron events before (blue) and after(red) 105
4.35 Geometry of the complete experiment imported into the GEANT4 106
4.36 VANDLE response to 2-MeV neutrons for the experiment setup. 107
4.37 Scattering of neutrons as seen from the frame of reference of 107
4.38 Scattering of neutrons as seen along the z-axis. 108
4.39 Calibration of VANDLE QDC using ^{241}Am phototpeak 108
4.40 Neutron-detection efficiency of a single medium VANDLE 109
4.41 Neutron-detection efficiency of the VANDLE array setup 109
4.42 QDC versus ToF parameterization obtained from simulation 110
4.43 Decay curve of ^{80}Cu with timing windows for sampling 110

5.1 Expected decay path of ^{79}Cu and the schematic of neutron emission 112
5.2 ToF neutron spectrum of ^{79}Cu obtained from VANDLE 112
5.3 ToF spectrum of neutrons in coincidence with the 730-keV transition 113
5.4 Beta-gated γ-ray spectrum of ^{79}Cu obtained from Clovers 113
5.5 Absolute intensity (top) and calculated *log(ft)* (bottom) 116
5.6 Decay curve gated on the 4153-keV line in the β-decay 116
5.7 Various scenarios for the placement of the 4153-keV line 117
5.8 Reduced transition probability B(GT) to neutron-unbound states 119
5.9 Expected decay path of ^{80}Cu and a schematic of neutron emission 119
5.10 β-gated neutron spectrum of ^{80}Cu fitted using 120
5.11 γ-ray spectrum of ^{80}Cu obtained 120
5.12 Reduced transition probability B(GT) to neutron-unbound states 121
5.13 Expected decay path of ^{81}Cu and a schematic of neutron emission 123
5.14 Beta-gated neutron ToF spectrum of ^{81}Cu deconvoluted 123
5.15 Beta-gated γ-ray spectrum of ^{81}Cu obtained 124
5.16 Reduced transition probability B(GT) to neutron-unbound 125

6.1 Model of beta decay of Cu isotopes in the shell-mdoel framework for N>50. . 128
6.2 Shell-model calculations for the decay of ^{78}Ni 130
6.3 Shell-model calculations for the decay of ^{78}Ni 131
6.4 Shell-model calculations for the decay of ^{78}Ni 131
6.5 Shell-model calculations performed for the decay of 133
6.6 Shell-model calculations performed for the decay of 134
6.7 Comparison of cumulative BGT from the experiment 134
6.8 Comparison of cumulative strength distribution 136
6.9 Shell-model calculations for the decay of ^{81}Cu. 136

Chapter 1

Motivation

1.1 Background

The atomic nucleus consisting of neutrons and protons offers insights into the nature of subatomic interactions. These interactions decide how nucleons form a nucleus and how it decays. The well-known decay mechanisms of a nucleus include β-decay, α-decay, γ-decay, and neutron or proton emission. There are also two-step radioactive decays for example, a combination of β-decay and neutron emission called β-delayed neutron emission.

β-delayed neutron emission was first discovered in nuclear fission by R.B. Roberts *et al.,* 1939[1]. It is a process observed in nuclei lying on the neutron-rich side of stability line on the chart of nuclei. Neutron emission is possible when the Q-value (Q_β) value of the decay exceeds the neutron separation energy (S_n) close to the neutron drip line. As we approach the neutron drip line, we expect increased chances of beta-delayed neutron emission due to an increase in β decay Q_β and decrease in S_n. When moving towards the neutron-rich region of the chart of nuclei, βn-decay becomes dominant. This occurs when the daughter nucleus formed post β^--decay is in an excited state and unstable against particle emission. The daughter nuclei, instead of deexciting through γ-ray emission, may emit neutrons. Figure 1.1 illustrates this effect showing the energy window (Q_β-S_n) for known nuclei which keeps increasing when more neutrons are added. Furthermore, excited states can be populated in the daughter nuclei above the two-neutron separation energy (S_{2n}), enabling the emission of two neutrons.

Over the years, a number of nuclei were seen to exhibit this phenomenon. There are currently just over 200 nuclei with measured emission probability (P_{xn}) values [2] for x neutrons. However, a large number of nuclei are expected to engage in beta-delayed neutron emission as suggested by recent work of Moller *et al.,* 2019 [3], here (P_{xn}) values for nuclei spanning the entire chart of nuclei are predicted. The first observation of multi-neutron emission was seen for ^{11}Li, which was identified to be a 2n emitter. β2n emission is mainly seen in nuclei lighter than Fe ranging from Li to K. ^{86}Ga [4, 5] stands as the strongest 2n emitter to date with measured 2n emission branching ratio of $\sim$ 16.2(9)%. ^{100}Rb was known to be the heaviest β2n emitter with P_{2n} value equal to 0.16(8)%. Recent measurements for nuclei in A $\geq$ 100 have resulted in identifying ^{136}Sb [6] as a 2n emitter with a small P_{2n} value of 0.14(13)%. ^{134}In has been identified as strong two-neutron emitter with P_{2n} value of 9(2)%, provided by M. Piersa *et al.,* 2021 [7], and ^{135}In is predicted to be a strong β2n emitter. Beta-delayed three-neutron emission is theoretically predicted in the A$\geq$100 region of the nuclei chart [3] but has never been experimentally measured. The P_{1n} values are scarce for nuclei in the heavy mass region A$\geq$ 150.

Study of delayed neutrons is essential to several fields ranging from nuclear structure and astrophysics to nuclear energy. With the advancement in the beam facilities enabling synthesis of nuclei in the unknown regions of nuclear chart, coupled with advanced detectors and electronics, the study of such exotic nuclei is now possible. The β-decay properties of these radioactive isotopes give valuable information on nuclear structure/shell evolution in the regions far-off stability and provide input for astrophysical nucleosynthesis calculations.

The β-decay strength function S_β(E) is one of the most important characteristics of the beta decay of a nucleus. It is the distribution of the squared modulas of the β-decay matrix elements as a function of the nuclear excitation E. The strength in the decay of nuclei on the very neutron-rich side can be attributed to the Gamow-Teller (GT) transitions which involve states with the same angular momentum quantum numbers (Δl=*0*) with no change of parity, and they are the leading order contributors of the nuclear beta-decay transition elements. However, transitions with Δl=*1* are also possible which are called First-forbidden (FF) transitions. These transitions are second-order contributors to the nuclear beta-decay transitions and are much smaller in magnitude compared to the allowed transitions. The

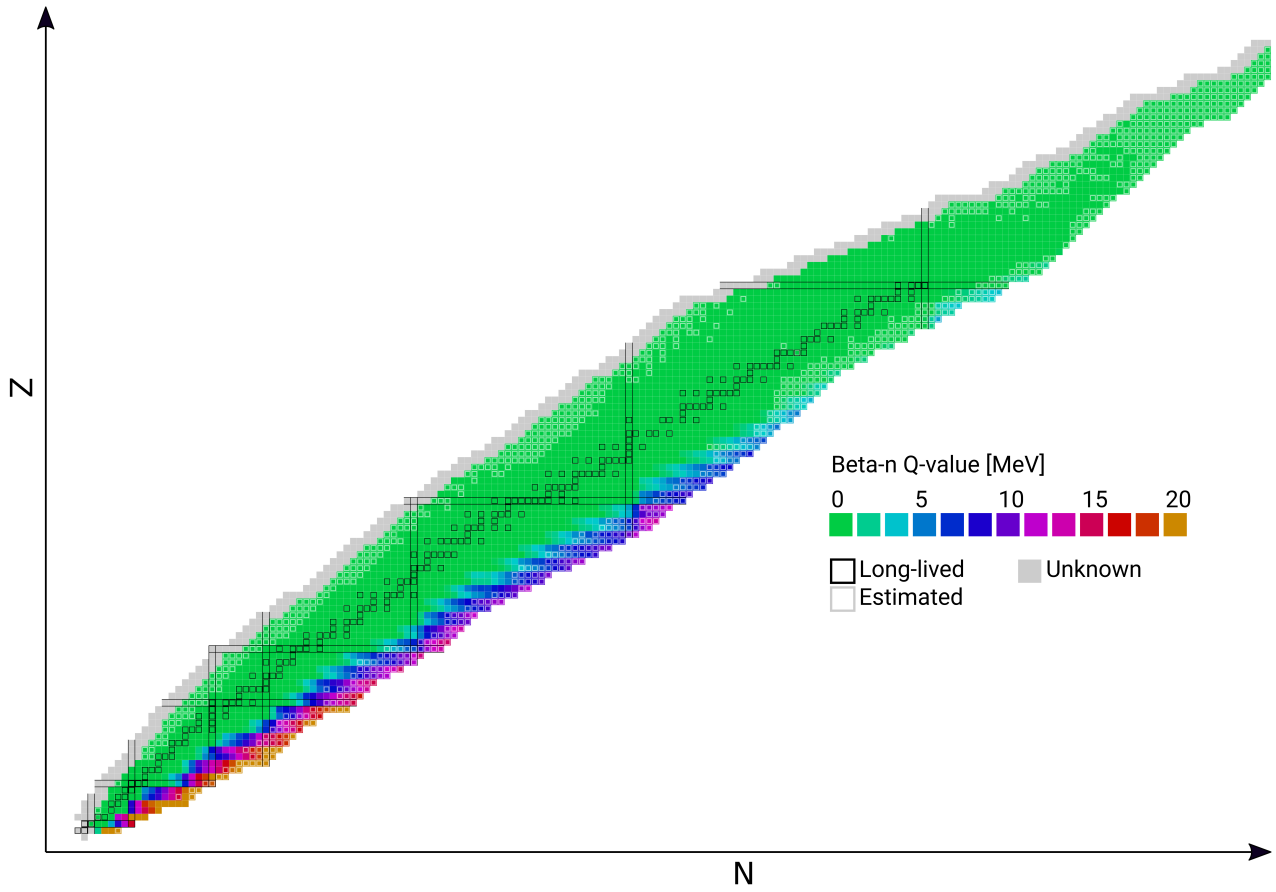


Figure 1.1: Q_{β}-S_n for the known isotopes in the nuclear landscape. A higher value is seen for nuclei with a large N/Z ratio far-off stability. Source: *https://people.physics.anu.edu.au/∼ecs103/chart/*

probability of beta decay is decided by the strength and the phase-space density factor ($\propto {E_{fi}}^5$), where E_{fi} is the energy difference between the states in the daughter and parent nuclei.

From S_β(E) various inferences can be drawn about the structure of a nucleus. Delayed neutron emission spectroscopy of ^{83,84} Ga [8] using VANDLE [9] revealed that all the GT beta strength is concentrated around S_n and is due to conserved shell structure, which can be pictured as ^{78}Ni core decay. The βn-emission probabilities contain information about the structure of involved states and their excitation energies. For nuclei with a large A/Z asymmetry FF transitions involve neutron and proton states near the Fermi surface and populate low-lying states in the daughter nucleus with a large decay rate ($\propto {E_{fi}}^5$) and can start to compete with GT transitions irrespective of their large nuclear decay transition matrix element. For the medium and heavy nuclei, the P_n values may show sensitivity to the competition between allowed GT and FF β-transitions caused by the ordering of the single-particle shell model states. The data regarding delayed-neutron branching ratios are also helpful to test the robustness of nuclear structure models far-off stability. The nuclei at and around shell gaps, e.g., in the doubly magic ^{78}Ni region, are an excellent testing and development ground for a variety of nuclear models. Many of the r-process [10] nuclei are expected to be β-delayed neutron emitters, but the competition between β1n and β2n decay modes is not yet understood. The quantitative modeling of this effect requires the knowledge of the β-decay strength distribution, as well as a statistical model treatment of one- and two-neutron emission from the excited states in the daughter nucleus. A part of the proposed experiment was to measure direct βn branching ratio in the decay of ^{78}Ni, which is the only doubly-magic nucleus emitting β-delayed neutrons. A competition between one- and two-neutron emission has been addressed by Yokoyama *et al.* [4] in the study of ^{87}Ga. Results from the experiments at RIKEN are consistent with these measurements and show previously implemented cut-off model of the shell-model calculations to reproduce the $P_{1n,2n}$ values. The large decay strength deduced from the observed intense neutron emission is a signature of Gamow-Teller transformation. This observation was interpreted as evidence for allowed β decay to ^{78}Ni core-excited states, leaving the nucleus in the highly excited

state because of the N = 50 shell gap. Further, there is great interest in β-delayed neutron-emission branching ratios measurements of neutron-rich nuclei, because they influence the final isotopic abundances of heavy isotopes during the late stages of rapid neutron capture r-process [11, 12]. A detailed study on the neutron energy and branching ratios can be a stepping stone to understanding the abundance patterns intensifying around the shell closures. Accurate and precise measurements of β-delayed neutron precursors are required to help improve nuclear physics inputs to modern r-process simulations with the aim of constraining the astrophysical site of the r-process. Detailed spectroscopy of nuclei can explain P_{xn} for a r-process nuclei.

To summarize, beta-delayed neutron emission is the dominant process for nuclei with a large neutron-to-proton asymmetry. For nuclei with large P_{xn}, the majority of the beta-decay strength is located above the neutron separation energy (S_n). To understand the decay of these nuclei, it is important to measure the details of β-decay strength distribution above (S_n) and that requires measuring the energy of the delayed neutrons. The focus of the present work is to study β-decay of nuclei in the ^{78}Ni region and extract $S_\beta(E)$ to understand neutron-emission mechanisms in these nuclei. In order to perform these measurement, a position-sensitive detector using YSO crystal is developed to enable precision neutron time-of-flight measurements. The detector was successfully employed with both the BRIKEN neutron counter and the VANDLE array at the Radioactive Ion Beam Facility (RIBF) at RIKEN Nishina Center, Japan.

The focus of this work is on the VANDLE experiment performed at the Radioactive Isotope Beam Factory (RIBF) present at RIKEN Nishina Center, Japan, to measure β-decay strength distribution to neutron-unbound states for the isotopes in the ^{78}Ni region. The BigRIPS fragment separator present at the facility was used to filter out the reaction products of the 345 MeV/u ^{238}U with ^{9}Be target. The experiment is the first endeavor to conduct neutron spectroscopy in the ^{78}Ni region. The measurements from the VANDLE experiment will enable the determination of the feeding intensity to the excited states in the daughter nucleus and compute the associated beta strength. The dissertation reports on the experimental study of β-decay of neutron-rich ^{79,80,81}Cu isotopes and compares the

experimental data to theoretical calculations. The dissertation also describes the details of the experiments and analysis methods developed in the pursuit of the measurements.

1.2 Beta Decay Fundamentals

β-radioactivity was discovered as one component of natural radioactivity (with α and γ components) at the turn of the 20th century by Ernest Rutherford. The first experimental observations of this process were electrons emitted from radioactive sources. Further studies showed that the electron energy spectrum was continuous and that β-decay seemed to violate conservation laws of nuclear physics (in particular energy, spin, and parity). The experimental observations convinced W. Pauli in 1930 to propose the emission of a second particle simultaneously with the electron, with negligible mass, no electrical charge, spin 1/2 and positive parity [13]. This particle was later called the neutrino, and its existence was experimentally verified in 1956 [14]. β-decay is generally described as a process where a nucleus having Z protons and N neutrons decays to a nucleus having the same mass number A but with (Z $\pm$1, $N\mp$ 1). A β^--decay may be regarded as the transformation of one of the protons to a neutron, and β^+-decay as that of one of the neutrons to a proton.

$$\beta^- \textbf{ decay} : A(Z,N) \rightarrow A(Z+1,N-1) + e^- + \overline{\nu}_e \tag{1.1}$$

$$\beta^+ \textbf{ decay} : A(Z,N) \rightarrow A(Z-1,N+1) + e^+ + \nu_e \tag{1.2}$$

Electron capture is another possibility where a nucleus captures an atomic electron. This process thereby changes a proton to a neutron and simultaneously causes the emission of an electron neutrino.

$$\textbf{Electron capture} : e^- + A(Z,N) \rightarrow A(Z-1,N+1) + \nu_e \tag{1.3}$$

Electron capture is mainly in competition with β^+ decay and its probability is proportional to Z^3, owing to the increased Coulomb field and small electronic radius with

increasing proton number in atoms. The Q value of a reaction is defined as the difference between the total kinetic energy before and after the reaction.

$$Q = T_{\mathrm{f}} - T_{\mathrm{i}} \tag{1.4}$$

Q values can further be expressed in terms of the atomic mass difference between parent and daughter nuclei. The expressions for Q-value for various decay types are listed as follows:

$$\beta\_decay : Q_{\beta^-} = [M(Z,N) - M(Z-1,N+1)]c^2 \tag{1.5}$$

$$\beta_+ decay : Q_{\beta^+} = [M(Z,N) - M(Z+1,N-1)]c^2 - 2m_{\mathrm{e}}c^2 \tag{1.6}$$

The $2m_ec^2$ term is used to compensate for the energy required to create a positron emitted and the atomic electron that must be ejected in going from a neutral atom of Z electrons to one with Z-1 electrons

$$Q_{\mathrm{EC}} = (M(Z,N) - M(Z+1,N-1))c^2 - B_{\mathrm{e}} \tag{1.7}$$

where B_e is the ionization energy of the captured electron.

Nuclear β-decay was explained by Enrico Fermi [13] in 1933. The transition rate (λ) for β-decay can be calculated using the Fermi's golden rule formulation, where a transition rate depends upon the strength of the coupling between the initial and final state of a system and upon the number of ways the transition can happen (*i.e.*, the density of the final states)

$$\lambda = \frac{2\pi}{\hbar}|\langle\phi_k(r)|H^{'}|\phi_o(r)\rangle|^2\rho(E_f) \tag{1.8}$$

where ρ (E_f) is the density of final states, and $H^{'}$ is the nuclear matrix operator $\phi_{\mathrm{k}}(r)$ and $\phi_{\mathrm{o}}(r)$ describing the entire final and initial states of the system, respectively. The quantum mechanical problem can be broken into two parts: first, to identify the matrix elements involved, and second, to determine the density of final states.

The initial state is characterized by the properties of the parent nucleus (spin, parity), and we assume it to be at rest and can be written as follows:

$$|\phi_o(r)\rangle = |J_i M_i \zeta\rangle. \tag{1.9}$$

The final state is a combination of three particles, a neutral lepton (neutrino/antineutrino), a charged lepton (electron/positron), and the daughter nucleus.

The final wave function can be written as follows:

$$|\phi_k(r)\rangle = \frac{1}{\sqrt{V}} e^{ik_e \cdot r} \frac{1}{\sqrt{V}} e^{ik_\nu \cdot r} |J_f M_f \zeta\rangle, \tag{1.10}$$

where $|J_f M_f \zeta\rangle$ is the wave function of the daughter nuclear state. The two factors of $V^{-1/2}$ are there for normalizing wave functions of the two leptons. The product of the two plane waves can be expanded in the form of spherical harmonics. The final wave function can be written as follows:

$$|\phi_k(r)\rangle = \frac{1}{V}\{1 + i\sqrt{\frac{4\pi}{3}}(kr)Y_{10}(\theta, 0) + O((kr)^2)\}|J_f M_f \zeta\rangle \tag{1.11}$$

The nuclear transition matrix element by considering only the leading order terms of the spherical harmonics can be written in the following form:

$$\langle \phi_k(r)|H^{'}|\phi_o(r)\rangle = \frac{G_V}{V} \sum_{\mu M_f} \{\langle J_f M_f \zeta| \sum_{j=1}^{A} \tau_{\pm}(j)|J_i M_i \zeta\rangle + g_A \langle J_f M_f \zeta| \sum_{j=1}^{A} \sigma(j)\tau_{\pm}(j)|J_i M_i \zeta\rangle\} \tag{1.12}$$

In the equation 1.12, $g_A = G_A/G_V$ denotes the ratio of axial (G_A) and polar (G_V) vector coupling constants, $\tau_{\pm}$ denotes the isospin raising or lowering operator, and σ is the intrinsic spin operator. The equation only represents allowed decays containing only the leading order terms in the spherical harmonics. The first term in the equation is generally referred to as Fermi decay and carries zero angular momentum. The second term represents Gamow-Teller decay and carries a unit of angular momentum. Matrix elements for transitions with angular

momentum greater than one are smaller in value and represent higher-order terms of the operator with a complicated wave function.

Considering all the prior statements, the β decay rate can be written in the form of an integral as follows:

$$\lambda = \frac{g^2|M_{fi}|^2}{2\pi^3\hbar^7c^3}\int_0^{p_{max}} F(Z_D, p_e)p_e^2(Q - T_e)^2 dp_e. \tag{1.13}$$

Here $|M_{fi}|^2$ is a nuclear matrix element representing the overlap between the initial and final nuclear states, g is the strength parameter, p_e is the electron momentum, and T_e is the electron kinetic energy. β^+-particles will be repelled by the nucleus, and the higher energy spectra are shifted to the higher energy side, whereas β^--particles will be attracted and slowed down. These effects are incorporated by implementing the coulomb distorted wave functions and are contained in a spectrum distortion expression called the Fermi function, $F(Z_D, p_e)$, where Z_D is the atomic number of the daughter nucleus. Equation 1.13 can be written in a simplified way by writing the integral term as $f(Z_D, p_e)$, known as the Fermi Integral.

$$\lambda = \frac{g^2|M_{fi}|^2m_e^5c^4}{2\pi^3\hbar^7}f(Z_D, p_e) \tag{1.14}$$

or in terms of the partial half-life of the parent nucleus, t as:

$$ft = \ln 2\frac{2\pi^3\hbar^7}{g^2|M_{fi}|^2m_e^5c^4} \tag{1.15}$$

The left-hand side of this equation is called the comparative half-life or *ft-value*, because this value can be measured in experiments and should only depend on the nuclear matrix elements and the β-decay strength constant. Typical *ft* values vary from 10^3 s to 10^{22} s; therefore, the base-ten logarithm of this value or *logft* is usually given in the literature.

Allowed Transitions

The notation J^{π} is used in the following, where J is the total spin of the nucleus or particle, and π is the parity associated with that state.
The selection rules for allowed transitions are as follows:

1. Leptons $L_l \rightarrow 0$ (no angular momentum carried by the leptons)

2. Nucleus $\pi_i \pi_f = +1$ (no parity change)

Since the two leptons can couple to a total intrinsic spin S, and given the condition that they do not carry angular momentum, the change in the total angular momentum of the nucleus is dictated by how the spins of the two emitted leptons couple with each other. When the spins of the leptons are anti-parallel, the total spin $\vec{S_l} = 0$, and only $\Delta\vec{J} = 0$ is possible (which is a singlet state). The corresponding transitions are called *Fermi* transitions or *vector* transitions. On the other hand, if the spins of the two leptons are aligned $\vec{S_l} = 1$, leading to ΔJ = 0, $\pm$1 (triplet state). This type of transition is called Gamow-Teller (GT) or *axial* transitions.

Transitions where the spins of the final and initial states are $J_f = J_i = 0$ ($0 \rightarrow 0$) are pure Fermi transitions. Alternatively, transitions with ΔJ = $\pm$1 are called pure GT transitions. A particular case of Fermi transition occurs when the nucleon involved in the β-decay process does not change any of its quantum numbers. This corresponds to $0^+ \rightarrow 0^+$ transitions, which are experimentally observed near the N = Z region. These transitions are labeled as *super-allowed* due to very small observed *log(ft)* values.

Forbidden Transitions

Forbidden transitions follow at least one of the following selection rules:

1. Leptons $\rightarrow \vec{L_l} > 0$, (angular momentum carried by leptons) or,

2. Nucleus $\pi_i \pi_f$ = -1 (change of parity).

These transitions are called forbidden because they are highly suppressed compared to allowed transitions. These transitions are represented by a second-order contribution of

the nuclear matrix element from a complicated wave function. Since the matrix element is squared in the determination of the decay constant, each unit of l that has to be carried by the leptons will suppress the decay constant by approximately a factor of 10^{-4} compared to the case with $l = 0$.

1.3 Delayed Neutron Emission

Several techniques are used to predict the P_n values, including phenomenological [15], shell model [16], and macroscopic-microscopic models with strength from QRPA or Gross-Theory[17]. Models help to provide information on how to plan experiments for nuclei far-off the reach of beam facilities. In cases where the experiments are feasible, the theoretical predictions can be tested against the experimental measurements, thus allowing for validation of the approximations used in constructing the theoretical model; improvements can be made to the models when the discrepancies are observed between predicted and observed results.

β-delayed neutron emission is a multistage process, as shown in Figure 1.3. The first stage is the β-decay of the precursor (A, Z) nucleus, which results in feeding the excited states of the emitter nucleus (A, Z+1). In the second stage, it is followed by the γ de-excitation to the ground state or neutron emission to an excited state or to the ground state of the final nucleus (A-1, Z+1), where Z is the atomic number, and A is the mass number of the precursor. The modeling scheme can also be broken into various steps to achieve the final delayed neutron energy spectrum or emission probabilities. Theoretically, the two important β-decay quantities, $T_{1/2}$ and P_n, are determined by the β-strength function $S_\beta(E)$,

$$1/T_{1/2} = \sum_{0 \le E_i \le Q_\beta} S_\beta(E) \times f(Z, R, Q_\beta - E_i) \tag{1.16}$$

where R is the nuclear radius, Q_β is the maximum β-decay energy, and $f(Z, R, Q_\beta - E_i)$ is the Fermi function. From this definition, $T_{1/2}$ may contain information about the average β feeding of a nucleus. However, since transition rates to the low-lying states are strongly enhanced by the phase-space factor [18] of β-decay, f$\sim (Q_\beta - E_i)^5$, the largest contribution to $T_{1/2}$ may originate from low-energy portion of $S_\beta(E_i)$. As a general view of the β decay,

Figure 1.2 shows the decay of a nucleus, and how a convolution of phase-space factor and $S_\beta(E_i)$ decides beta-decay feeding intensity (I_β).

The β-delayed neutron emission probability (P_n) was often defined as

$$P_n = \frac{\sum_{S_n}^{Q_\beta} S_\beta(E) \times f(Z, R, Q_\beta - E_i)}{\sum_{0}^{Q_\beta} S_\beta(E) \times, f(Z, R, Q_\beta - E_i)} \tag{1.17}$$

which defines P_n as the ratio of the integral β intensity to states above the neutron separation energy, S_n, to the total β intensity. The formulation to calculate the P_n values in the equation above is described as the *cutoff* method. However, in cases where two-neutron emission is energetically possible, competition between 1n and 2n channels must be included. In order to explain the 1n/2n competition, Mumpower *et al.* [19] implemented the Hauser-Feshbach (HF) statistical model with Quasiparticle Random Phase Approximation (QRPA). The calculations are achieved by first calculating the β-decay intensities to accessible states in the daughter nucleus using QRPA. The subsequent decay from the states in the daughter nucleus by neutron or γ-ray emission is then treated by the statistical HF theory.

1.4 R-process and Nucleosynthesis

The synthesis of nuclei beyond iron is attributed to the capture of neutrons by seed nuclei, and it can only happen under extreme conditions. The processes known to play an essential part in this phenomenon are designated as r-process (rapid) and s-process (slow) [11], where neutron-capture reaction rates are relative to the β-decay time scales. For r-process $\tau_n \ll \tau_\beta$, whereas for s-process, the opposite case occurs with $\tau_n \gg \tau_\beta$. Considering the time scales, the neutron capture path in the s-process is close to the line of stability, and the nuclei involved in the due course can be easily studied experimentally. R-process, on the other hand, will proceed into the very neutron-rich side, far from the line of stability, which consequently leads to the production of nuclei with a large N/Z asymmetry. Once the neutron flux is exhausted in the process, the unstable nuclei will decay back to the line of stability and thereby form stable nuclei. Figure 1.4 shows the r-process pathway and the abundance peaks around magic numbers.

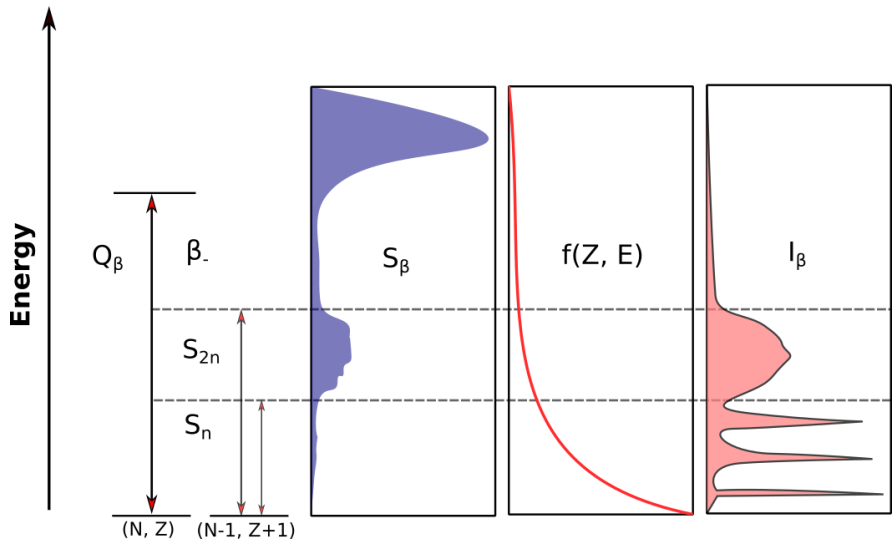


Figure 1.2: A schematic showing the decay of a β-delayed neutron precursor and the associated strength at the corresponding excitation energy. The phase-space factor curtails I_β at high excitation energies and augments it at lower energy.

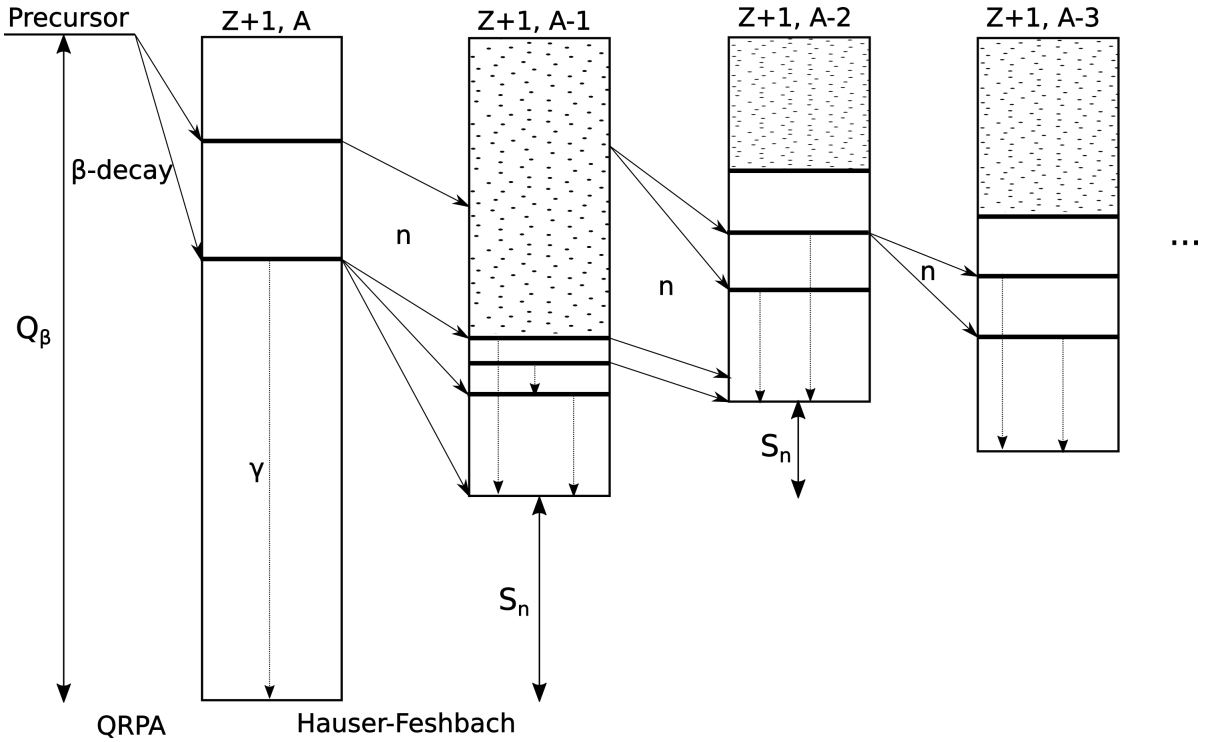


Figure 1.3: Schematic of the initial population of the daughter nucleus (Z+1, A). Delayed neutron and γ-ray emissions are handled in the HF framework and shown by solid and dotted lines, respectively. The statistical decay is followed until all available excitation energy is exhausted, denoted by trailing dots. Schematic adopted from reference [19].

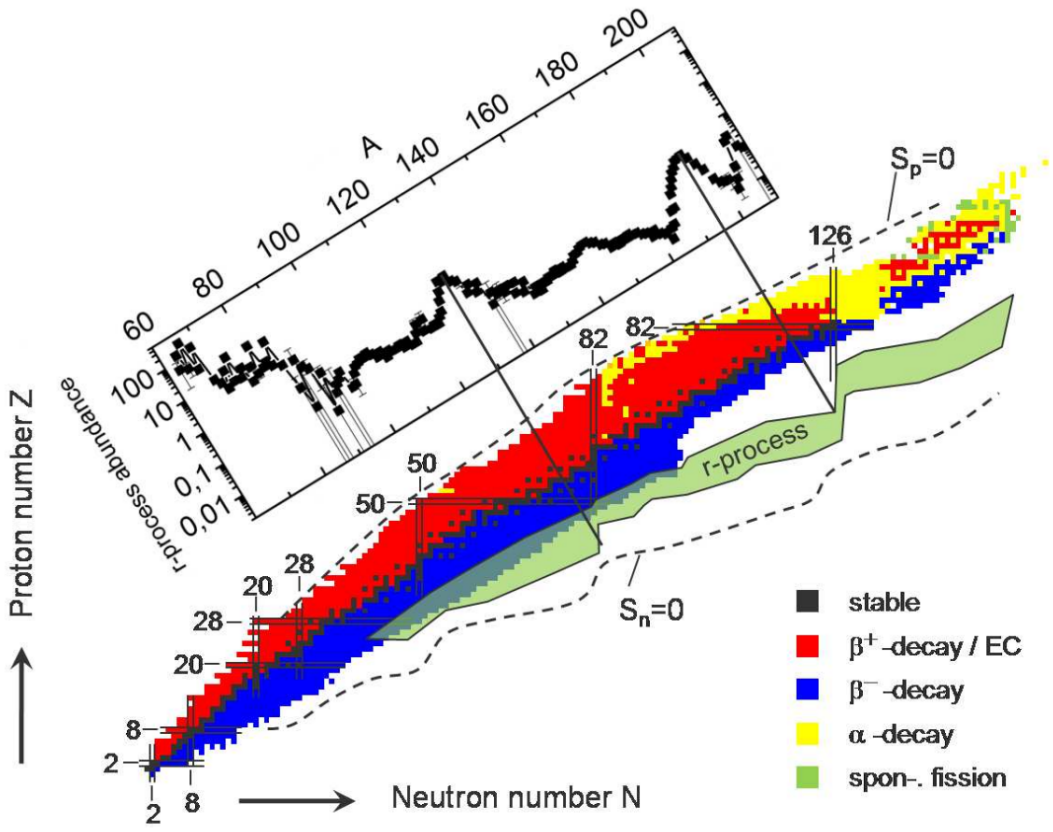


Figure 1.4: Nuclei chart showing color-coded regions of stability, β-decay, α-decay, and the r-process path. The r-process nuclei abundance pattern overlaid on the top-left demonstrates the peaks near closed nuclear shells (Magic numbers) [20].

The r-process pathway in Figure 1.4 connects the isotopes with the maximum abundance in each isotopic chain. β^--decays transfer nuclei from one isotopic chain to the next and determine the speed of the process. Abundance peaks occur due to long β-decay half-lives where the flow path comes closest to stability (closed neutron shells). The knowledge of S_n and β-decay half-lives is helpful in determining the shape of the abundance curves. Given the conditions conducive to r-process nucleosynthesis, experimental measurements are very challenging. The experimental bottleneck of synthesizing nuclei in the unexplored region of the chart of nuclei has been recently unblocked by a few facilities, thereby opening a whole new window to a plethora of information regarding mass and half-lives about the participating nuclei.

One of the significant current challenges is the determination of the site or sites for the r-process synthesis and therefore the identification of the origin of more than half of all the elements heavier than iron. The answer is complex and highly intermingled between the astrophysics describing the conditions of the relevant scenarios and the physics of nuclei that operate in those scenarios. The sites of the r-process have not been unambiguously identified, but a large number of neutrons required in short time scales suggest a requirement for large neutron densities, which are seen in explosive environments. The two leading candidates are type II (core-collapse) supernova explosions and neutron star mergers. A recent observation of a binary neutron star merger GW170817 [21] in various regions of the electromagnetic spectrum helps to narrow r-process sites. The observations from the merger suggest that the later part of the light curve produced by the post-merging supernova is due to the radioactivity of lanthanides produced in the r-process.

1.5 Nuclear Shell Structure

The models used to define the structure of a nucleus are broadly classified into two categories, collective and independent particle models. Collective models assume that nucleons interact strongly in the nucleus, and their mean free path is small, whereas independent particle models assume that the nucleons interact under the realm of the Pauli principle. Models such as the liquid-drop model [22] (collective) provide a good description of average behavior,

such as the occurrence of binding energy pertaining to the odd-even behavior. But these models do not explain the appearance of magic numbers in nucleons. This is mainly due to the structure of shells that cannot be obtained by the liquid-drop model. Hence, there is a need to treat the nucleus as a quantum system to provide a justification for this behavior.

The Fermi Gas Model [23, 24], which falls under the category of independent models, is based on the notion of nucleons moving freely in the nucleus, governed by the Pauli principle. A nucleon in the nucleus feels the force of attraction created by all the nucleons around it. The situation can be imagined as similar to a box, inside of which nucleons can move freely but occupy different energy states. The Fermi gas model, despite its simplicity, explains many of the nuclear properties; it explains the lesser number of protons compared to neutrons as we go from low A to high A nuclei, which is due to shallowing of the proton well because of the Coulomb repulsion between protons. Another characteristic explained by the Fermi Gas Model is the high abundance of even-even nuclei compared to odd-odd nuclei. This is explained by the possibility of an isolated neutron or proton (each in their respective potential wells) in odd-odd nuclei to crossover to the well of the other via β-emission, returning to stability.

The Shell Model [25, 26] also follows the idea of nucleons moving independently of each other in the nucleus, similar to the Fermi gas model. The difference here from the Fermi Gas Model is the introduction of a central potential, similar to the potential that acts on electrons in an atom. The central potential is the average potential created by all the nucleons in a nucleus. A nucleon is thus under the influence of a potential created by the rest of the nucleons in the nucleus. The potential should be determined in such a way to best produce the experimental results.

To give a mathematical formulation of the shell model, the Hamiltonian of a system consisting of A-bodies can be written as

$$H = \sum_{i}^{A} T_i(r_i) + V(r_1, ..., r_A), \tag{1.18}$$

where T is the kinetic energy operator and V is the potential function. Now, if the interaction is restricted to two bodies, the Hamiltonian assumes the mathematical form as follows:

$$H = \sum_{i}^{A} T_i(r_i) + \frac{1}{2} \sum_{ji} V_{ij}(r_i, r_j). \tag{1.19}$$

In the shell model construct, a nucleon i is influenced not only by the potential $\sum_j V_{ij}$, but a central potential $U(r_i)$, which depends only on the coordinates of the nucleon i. This potential can be introduced in the Hamiltonian as follows:

$$H = \sum_{i}^{A} T_i(r_i) + \sum_{i}^{A} U(r_i) + H_{res}, \tag{1.20}$$

H_{res} is called the residual interaction, which is the part of the potential V not incorporated in the central potential U:

$$H_{res} = \frac{1}{2} \sum_{ji} V_{ij}(r_i, r_j) - \sum_{i}^{A} U(r_i). \tag{1.21}$$

The H_{res} term is generally anticipated to have a very small/negligible contribution to the *Shell Model Hamiltonian.*

The shape of the central potential should capture the features of the nucleus, *i.e.*, the potential being maximum at the core and gradually decreasing closer to the nuclear perimeter. A potential called the "Woods-Saxon" form is generally used to capture the features mentioned [27], and a schematic is shown in Figure 1.5. It is mathematically defined as

$$U(r) = \frac{U_0}{1 + exp(\frac{r-R}{a})}, \tag{1.22}$$

where U_0, $\mathbf{R}$, and $\mathbf{a}$ represent potential well depth, the radius of the nucleus, and surface thickness, respectively. The Schrodinger equation with the Hamiltonian H can be solved numerically by providing wave functions of protons and neutrons characterized by the shell (n), orbital (l), and total angular momentum (j) quantum numbers.

A considerable improvement in matching the results with the experimental measurements was provided upon the addition of a spin-orbit interaction term to the Hamiltonian. The spin-orbit interaction term removes the degeneracy in the total angular momentum state j. A schematic of shell structure with the filling of levels is shown in Figure 1.6.



Figure 1.5: Wood-Saxon and square well potential for a nucleus with A = 70, U_0=50 MeV, and a = 0.5 fm. The plot demonstrates the shape of the Wood-Saxon potential (blue) compared to a square well potential (red).

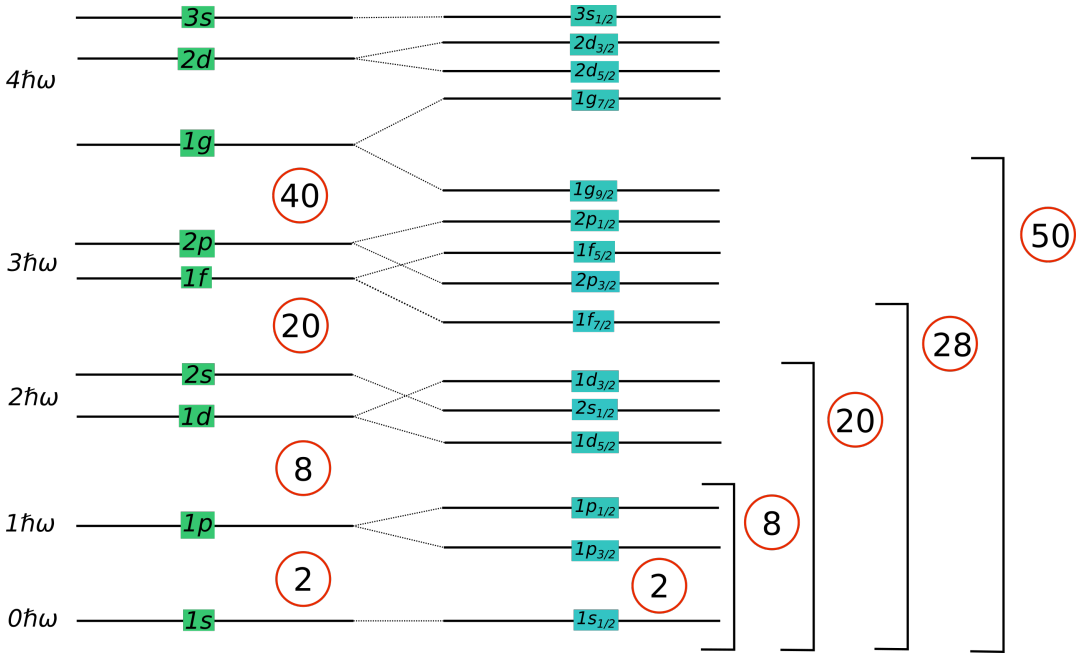


Figure 1.6: Level scheme of the shell model showing the breaking of degeneracy in the energy levels due to the spin-orbit interaction term. There is an emergence of some new magic numbers in the shell closing, such as 28 and 50. The level scheme is not concrete and is expected to change as per the nuclear potential chosen. [28]

After the discussion on the structure of an atomic nucleus using the Shell Model, we can re-state that an atomic nucleus is a quantum many-body system whose constituent nucleons (protons and neutrons) are subject to complex nucleon-nucleon interactions that include spin- and isospin-dependent components. For stable nuclei, the seemingly emerging patterns in some observations, such as the shell closure for neutrons or protons in nuclei: N, Z = 8, 20, 28, 50, 82, 126 can be explained with great success using shell-model calculations.

The testing of the shell model was originally developed to explain stable nuclei and their neighboring isotopes. The dynamics of nucleon interaction start to take a different turn with the addition of more neutrons/protons, mainly due to the N/Z ratio deviating heavily from one. The picture of nuclear structure is quite different for nuclei far-off from the stability; these nuclei are also termed as *exotic*. These exotic nuclei imply atomic nuclei with an unbalanced N/Z ratio as compared to stable ones, thus losing binding energy due to a large difference in Z and N [22]. Relatively smaller binding energies mean that β-decay channels open up, proceeding towards more N/Z balanced systems and resulting infinite (often short, sub-second, milliseconds) lifetimes. The asymmetry in the N/Z ratio along with an interplay of nuclear forces can lead to the emergence of new shell closures and shape deformations. The phenomenon of change in the orientation of nuclear orbitals with the addition of more neutron/protons in stable isotopes is called "Shell Evolution."

As an example of shell evolution, the systematic of the first 2^+ levels are shown in Figure 1.7. Part (a) of the figure shows the appearance of the magic numbers as predicted by the Shell Model, having higher first 2^+ excitation energy. Part (b) of the figure shows the data for nuclei measured until 2016, highlighting relatively high 2^+ excitation energy not predicted by the Shell Model, and displays the effects of shell evolution. The questions surrounding patterns in structure beyond stability can be answered by exploring various types of nuclear forces. The effects of nuclear forces on the shell structure can be studied in terms of their monopole component. The monopole matrix element of an interaction, $\hat{V}$ is defined as

$$v_{\mathrm{m;j,\ j'}} = \frac{\sum_{k,k'} \langle jkj'k'|\hat{V}|jkj'k'\rangle}{\sum_{k,k'} 1}, \tag{1.23}$$

where j and j' denote the single-particle angular momentum quantum numbers with k and k' denoting their respective magnetic sub-state, and quantity $\langle ...|\hat{V}|...\rangle$ is anti-symmetric in nature as per the Pauli exclusion principle. Equation 1.23 shows the averaging over all possible orientations of two interacting particles in orbitals j and j'. The monopole component of $\hat{V}$ is written, for $j \neq j'$, as

$$\hat{v}_{m;j,j'} = v_{m;j,j'}\hat{n}_j\hat{n}_{j'}, \tag{1.24}$$

where the $\hat{n}_j(\hat{n}_{j'})$ is the number operator of the orbits j (j'). The monopole component of the operator $\hat{V}$ is the average of all effects of $\hat{V}$, and it depends only on the occupation number of the orbits involved. Using the neutron-proton scheme, monopole interaction can be used with the convention: n_j and $n_{j'}$ as the occupation number for protons and for neutrons in the orbits, respectively.

The shift in the single-particle energy (SPE) of proton orbits (j) with the addition of neutrons in orbits (j') due to the monopole interaction can be written as

$$\Delta\epsilon_j = v_{m;j,j'}n_{j'}. \tag{1.25}$$

Due to the linearity of the monopole interaction, the effect of the monopole interaction can be magnified to a large degree with the increase in occupation of nucleons in valence orbit j', when we move away from stability towards the neutron-rich side. As an example, Figure 1.8 depicts the monopole interactions that can take place as we keep filling neutrons in the $1g_{9/2}$ (N>40) state, lying above the N=40 core. Single-particle proton states for Z > 28 can be filled in $2p_{3/2}$, $1f_{5/2}$, and $2p_{1/2}$.

The residual interaction can also have contributions from the spin-isospin interaction [30], which explain the appearance of magic numbers at Z=14 and N = 16. The tensor force [30] due to pion exchange is another contribution to the residual interaction that has been explored for some nuclei.

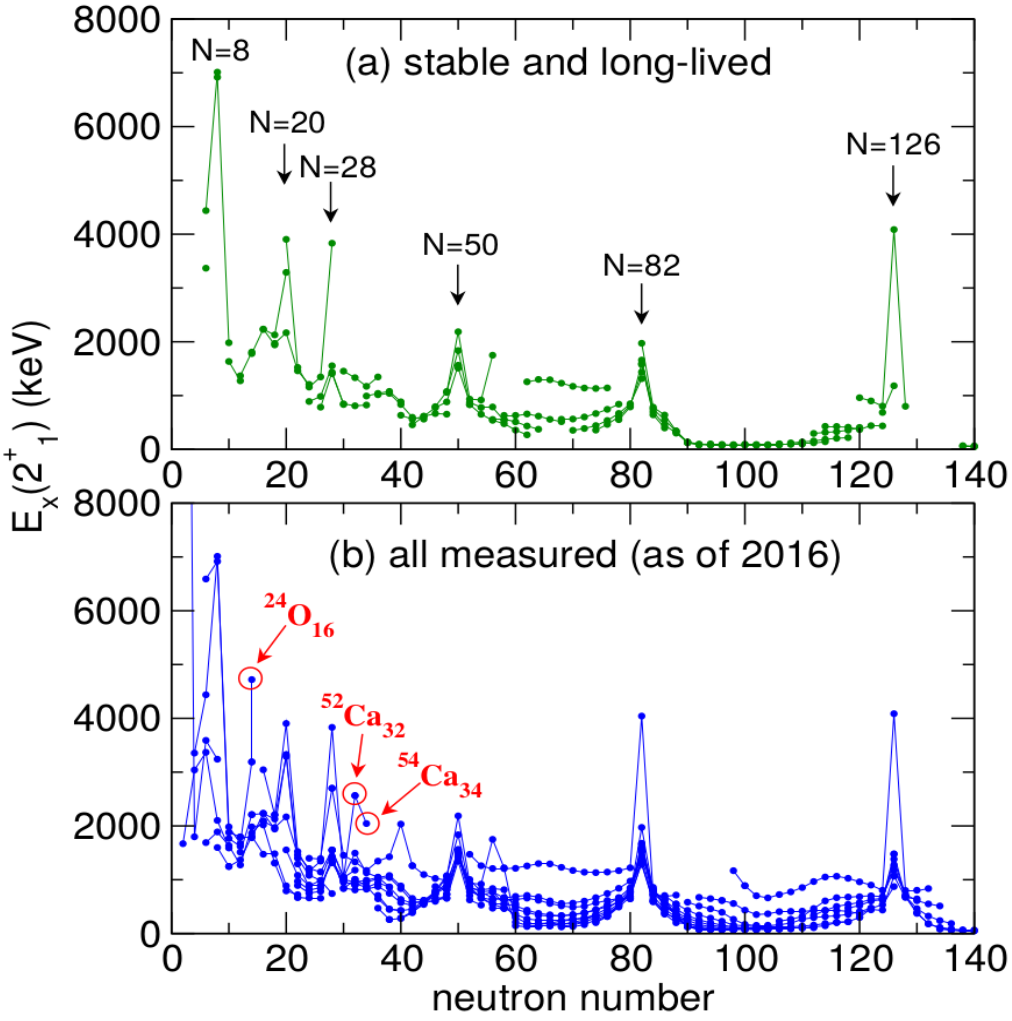


Figure 1.7: Systematics of the 2^+ excitation energy for a) stable istopes and b) all nuclei measurements up to 2016. [29]

1.5.1 Shell Evolution of Cu Isotopes

The sections above lay the basic foundation of the structure of a nucleus and its evolution upon filling it with more and more neutrons due to the monopole component of the nuclear forces. Here, we discuss the shell evolution of Cu isotopes. Copper isotopes contain just one proton above the Z=28 shell gap, offering a simple scenario to study nuclei close to magicity. Copper isotopes display a great deal of shell migration due to the monopole interaction and also display competition between single-particle and collective modes at low excitation energies [31, 32, 33]. The idea of migration of states was solidified with the observation of the lowering of the $5/2^-$ in ^{73,71}Cu [34]. This led to a belief that $5/2^-$ may eventually become the ground-state in ^{75}Cu. $5/2^-$ was later confirmed as the ground state in ^{75}Cu via magnetic moment measurements in the copper chain [33]. The inversion was also predicted to be prevalent in ^{77,79}Cu. Figure 1.9 shows the change in the energy of the $5/2^-$ and $3/2^-$ states with the increase in neutron number. The observed change in the energy of the low-lying state could be indicative of weakening of the Z=28 shell gap. So far there has been no experimental evidence of the reduction in the Z=28 shell gap. However, studies mentioned in [35, 36] suggest a weakening of the Z=50 shell gap, but the idea could not be substantiated with experimental measurements. Measurement of γ-rays from the ^{80}Zn$(p,2p)^{79}$Cu reaction at RIBF ascertained the persistence of the Z=28 shell gap [37]. The results from the experiment suggest treating ^{79}Cu as consisting of ^{78}Ni core with a valence proton. ^{78}Ni was identified to be doubly magic with its 2^+ state lying at 2.6 MeV [38] using in-beam γ-ray spectroscopy of ^{80}Zn$(p,3p)^{78}$Ni reaction. In this work, the beta-strength function to neutron-unbound states in the β-decay of ^{79}Cu will be deduced by measuring the intensity and energy of the neutrons emitted from ^{79}Zn. For N$\geq$50 Cu isotopes, the measurements of beta-strength will confirm the presence of the expected shell-gap between $g_{9/2}$ and $d_{5/2}$ orbital.

1.5.2 Similarity in ^{78}Ni and ^{79}Cu decay

Figures 1.10 and 1.11 show the nuclear shell structures of ^{78}Ni and ^{79}Cu, respectively. In the figures, a case of GT β-decay transition is also shown, where a neutron in $p_{3/2}$ state transforms

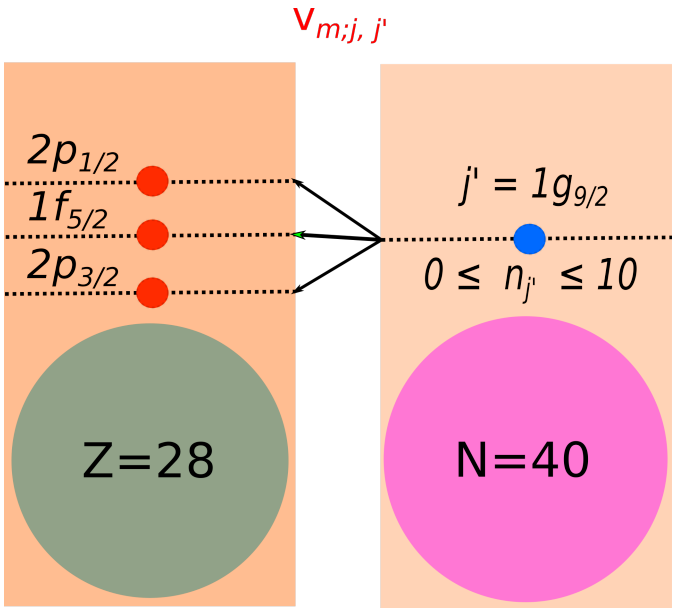


Figure 1.8: A graphical demonstration of the monopole interaction between the neutron single-particle state $1g_{9/2}$ and the proton single-particle states $2p_{3/2}$, $1f_{5/2}$, and $2p_{1/2}$. The shift in the energy of the state $1f_{5/2}$ is larger compared to the shift for $2p_{3/2}$ and $2p_{1/2}$ due to a large radial overlap ($\Delta l = 1$) between the f and g shells.

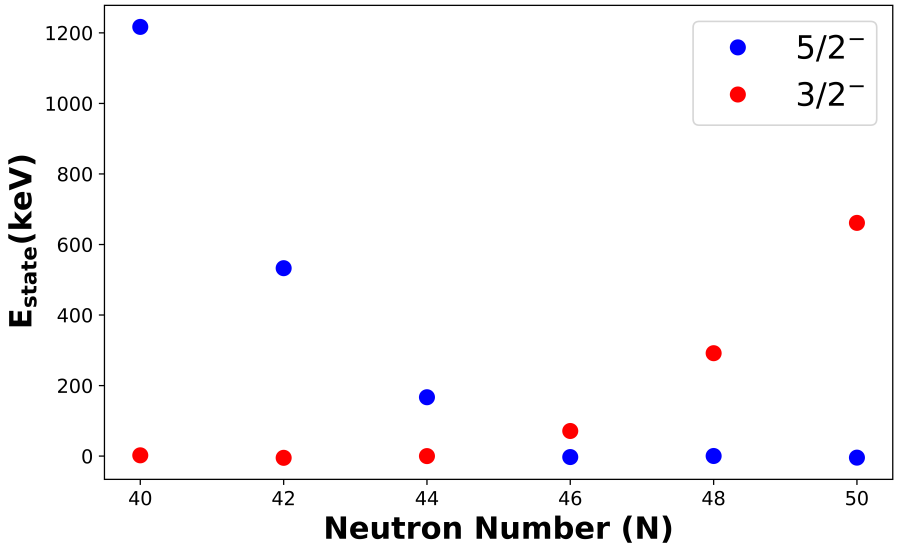


Figure 1.9: Systematics of the $5/2^-$ and $3/2^-$ states in the odd-even Cu isotopes. Data were taken from Refs.[39, 40, 41, 42, 43, 44].

into a proton in $p_{3/2}$ single-particle state. In the decay of ^{78}Ni, the total angular momentum configuration (J^{π}) of the daughter nucleus ^{78}Cu is decided by the coupling of various possible neutron (J^{π}_{n}) and proton angular momenta (J^{π}_{p}) after the β-decay. Various possible cases of neutron and proton angular momentum states formed in the daughter nucleus after the beta decay are shown in table 1.1. All of these configurations carry information about the structure of the nucleus at various occupancy levels in the parent nucleus. The β-decay of ^{79}Cu is similar to the β-decay of ^{78}Ni with the addition of a single proton occupying $p_{3/2}$ shell, as shown in the Figure 1.11. The addition of a single proton leads to more configurations in the daughter nucleus on top of the configurations present in the decay of ^{78}Ni. Thus, beta-decay strength obtained in the decay of ^{79}Cu can highlight major beta-decay transitions seen in the decay of ^{78}Ni.

1.5.3 Crossing N=50 Shell Gap

For Cu nuclei with N>50, the allowed Gamow-Teller transitions transform neutron states below the N=50 shell gap to proton spin-orbit partners above the Z=28 shell gap. These transitions can also be viewed as ^{78}Ni core excitations. These transitions may lead to high neutron-emission probabilities after the beta decay of the parent nucleus. Also, the presence of the Z=50 shell gap can affect the distribution of the beta-decay strength with excitation energy [8]. The decay of these nuclei is expected to be similar to the decay of ^{79}Cu but with the possibility of First-Forbidden transitions due to the presence of neutron $d_{5/2}$ and the available proton states above the Z=28 shell gap. The shell model NuShellX [45] does predict a shift in the beta-decay strength to a higher excitation energy when the N=50 shell gap is crossed. Figure 1.12 shows predicted reduced transition probability elements for Gamow-Teller transitions in the decay of $^{78-81}$Cu. The calculations predict the beta-decay strength function of ^{80,81}Cu at higher excitation energy relative to ^{79}Cu.

Table 1.1: Possible angular momentum configuration mixing of neutron-hole states with proton states with single occupancy after the beta decay of ^{78}Ni.

Sr. No.	Configuration
1	$\nu {p_{3/2}}^{-1} \otimes \pi {f_{5/2}}^{+1}$
2	$\nu {p_{1/2}}^{-1} \otimes \pi {p_{3/2}}^{+1}$
3	$\nu {p_{1/2}}^{-1} \otimes \pi {p_{1/2}}^{+1}$
4	$\nu {f_{5/2}}^{-1} \otimes \pi {p_{5/2}}^{+1}$
5	$\nu {p_{3/2}}^{-1} \otimes \pi {p_{3/2}}^{+1}$
6	$\nu {p_{3/2}}^{-1} \otimes \pi {p_{1/2}}^{+1}$
7	$\nu {f_{5/2}}^{-1} \otimes \pi {p_{3/2}}^{+1}$
8	$\nu {f_{7/2}}^{-1} \otimes \pi {f_{5/2}}^{+1}$
9	$\nu {g_{9/2}}^{-1} \otimes \pi {g_{9/2}}^{+1}$

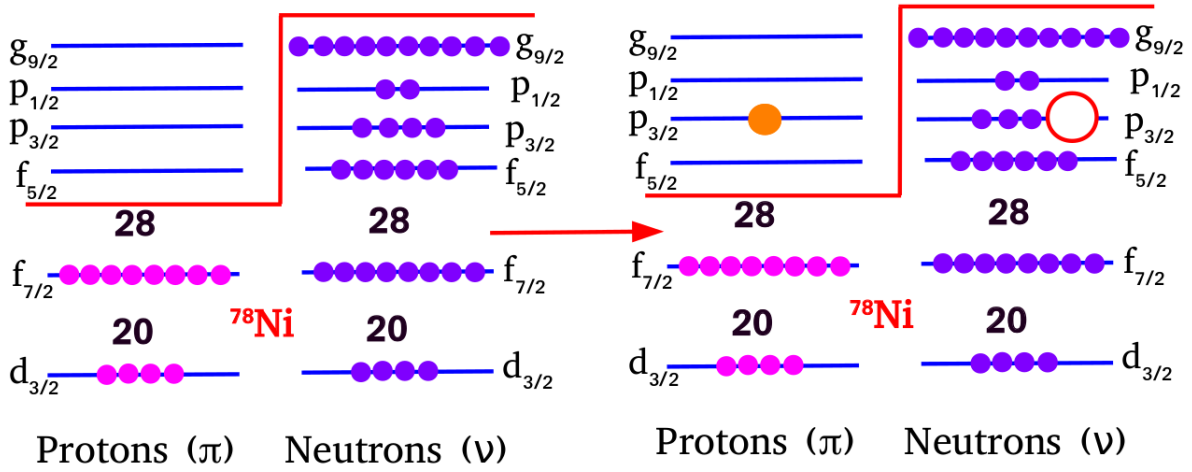


Figure 1.10: Shell structure of ^{78}Ni showing occupation of neutrons and protons in their respective shells. Shown is the scenario of ^{78}Ni GT beta decay, where a neutron in the $p_{3/2}$ orbital is transformed into a proton in the $p_{3/2}$ state.

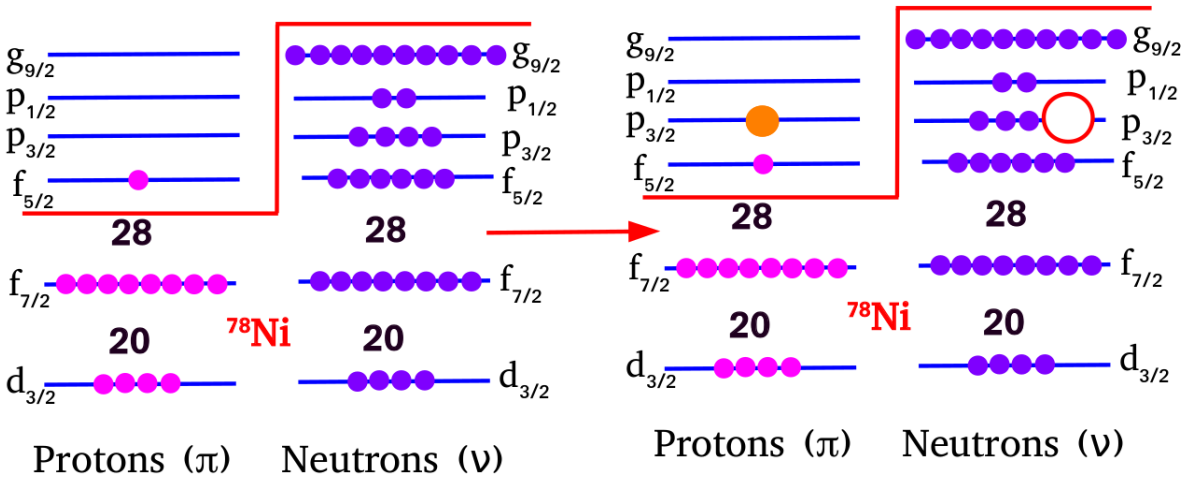


Figure 1.11: Shell structure of ^{79}Cu showing occupation of neutrons and protons in their respective shells. Shown is the ^{79}Cu (^{78}Ni+1p) GT beta decay, where a neutron in the $p_{3/2}$ orbital is transformed into a proton with occupation in the $p_{3/2}$ state.

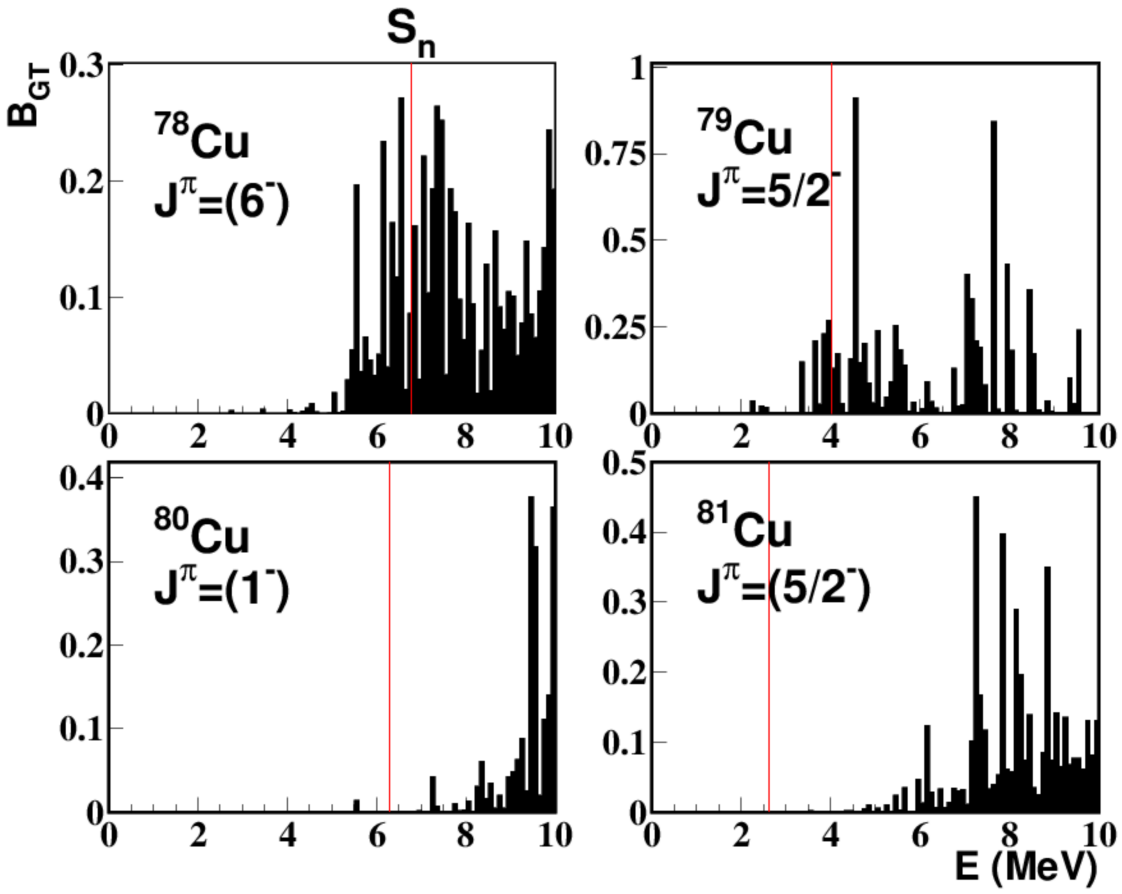


Figure 1.12: Predicted reduced transition probability of GT transitions in the beta decay of $^{78-81}$Cu using NuShellX [45]. The vertical red line in all the panels represents the S_n of the respective daughter nucleus.

Chapter 2

Implantation Detector Development

This chapter first explains the principle of detecting charged particles and neutrons using scintillators. The concepts are used in the construction of the YSO-based implantation detector. The design and image reconstruction of the detector are also discussed following the theory of scintillation.

Scintillators are some of the oldest materials to be used for particle detection. Scintillator use dates back to the early 1900s. Ernest Rutherford discovered α-particles with the aid of a scintillator called Zinc sulfide (ZnS) [46]. In the following years, huge strides were made in the development and implementation of these materials in various sectors of research and industry. The basic concept behind particle or incident gamma-ray detection using a scintillator is the conversion of the energy absorbed in the material into light, which is emitted in the visible band of the electromagnetic spectrum.

Scintillators are broadly categorized as organic and inorganic scintillators. The scintillation mechanism is different for the two classes. Here, the focus is on inorganic scintillators (halides, oxides, chalcogenides, and glasses). In luminescence, only a small fraction of atoms, called emission centers or luminescence centers, emit light. In inorganic scintillators, these inhomogeneities in the crystal structure are usually created by the addition of a trace amount of dopants, impurities called activators. A graphical depiction of the scintillation mechanism in a crystalline scintillator is shown in Figure 2.1. The ionizing radiation upon interaction leaves the system in a state of non-equilibrium, and the tendency to reach a state of equilibrium is led by a multitude of elementary processes, such as the

creation of primary electronic excitation which will produce an avalanche of secondary particles including electrons, holes, photons, and plasmons. These electronic excitations produce numerous thermalized electron-hole (e-h) pairs and low energy excitons which ultimately transform into light photons, i.e., scintillation. The following steps can broadly describe the scintillation process:

1. Absorption of the ionizing radiation and creation of primary electrons and holes.
2. Relaxation of the primary electrons and holes, thereby producing many secondary electrons, holes, protons, plasmons, and other electronic excitations.
3. Thermalization of the low-energy secondary electrons (holes) resulting in a number of e-h pairs with energy roughly equal to the band-gap energy E_g.
4. Energy transfer from e-h pairs to the luminescence centers and their excitation.
5. Emission from the luminescence centers.

2.1 Detection of Charged Particles

A charged particle dissipates its kinetic energy in its passage through a material. The interactions (excitation and ionization of atoms present in the material) depend on the charge and mass of the particle. Fast charged particles moving through matter interact with the electrons of atoms in the material. These kinds of energy losses are labeled as ionization losses. On the other hand, electrons can also lose energy via Bremsstrahlung, in addition to ionization losses.

What we observe through the energy loss of most of the charged particles is a statistical average of the two (excitation and ionization) processes occurring as the particle slows down. The stopping power S (dE/dx) of the material is determined concerning the energy lost (dE) by the particle within an infinitesimal distance (dx): the higher the stopping power, the shorter the range into the material the particle can penetrate. The quantity S is also referred to as *specific ionization loss*. The average ionization losses of a relativistic charged heavy particles are given by the well known Bethe-Bloch formula [47] as follows

$$-\frac{dE_{ion}}{dx} = \frac{4\pi N_A Z^2 e^4}{m_e V^2}\frac{z}{a}\left[ln\left(\frac{2mV^2}{\overline{I}(1-\beta^2)}\right) - \beta^2\right],, \tag{2.1}$$

Where z, m, and V are the charge, mass, and velocity of the particle, respectively; x (cm^2/g) is the path of the particle into the matter; Z and A are the atomic and mass number of the matter, respectively; N_A is the Avogadro number, and $\overline{I}$ is usually obtained empirically, but some estimates are made using the relation $\overline{I} = 13.5$ Z (eV). The Bethe formula is only valid for high enough energies, so the charged particles do not carry any atomic electron. At smaller energies or low velocity, the probability of ions carrying an electron from atoms in the matter reduces their effective charge and thus reducing its stopping power. At low energy, shell corrections are needed in Equation 2.1.

Following Equation 2.1, it can be inferred that the ionization power of a heavy charged particle (proton, α particle, multiply ionized atoms, etc.) is z^2 times greater than the ionization power of an electron of the same velocity. The mean range of a particle can be calculated by integrating the reciprocal of stopping power over energy as follows:

$$\Delta x = \int_0^{E_o} \frac{1}{S(E)} dE, \tag{2.2}$$

where E_o is the initial kinetic energy of the particle. The energy loss is characterized primarily by the square of the nuclear charge, Z, and the inverse square of the particle velocity, V. This gives a peak in energy loss at very low energies, as seen in *Bragg Curve*, a curve that plots the energy loss of ionizing radiation during its travel through matter.

The light output of the scintillator depends not only on the energy losses but also on the density of ionization. In spite of ionization losses increasing with the increasing charge and mass of the particles, there is a decline in the light output of the scintillator. The light produced in the scintillating material by highly ionizing particles (heavy ions) is lower than that produced by electrons of the same energy. Therefore, the signal generated by the ions will be seen at lower voltages than their real values for a scintillator calibrated with electrons or γ-rays due to the presence of light-quenching for heavy ions. A knowledge of these transformation factors is very important when it comes to detecting and interpreting heavy ions. Light yield dL is proportional to the energy-loss (dE) by the particle in the

scintillator

$$dL = SdE, \tag{2.3}$$

where S is the absolute scintillation factor. In differential form, the above equation is written:

$$\frac{dL}{dx} = S\frac{dE}{dx}. \tag{2.4}$$

The suppression of the light yield for the heavy ions is suggested by the Birks Relation [48]

$$\frac{dL}{dx} = S\frac{\frac{dE}{dx}}{1 + kB\frac{dE}{dr}}, \tag{2.5}$$

where $B\frac{dE}{dx}$ denotes the density of excitation centers along the track, k is the quenching factor; kB is known as the Birks Factor. The quenching factor ($Q_i(E)$) for ions is defined as the ratio of the light yield of ions relative to that of electrons at the same energy.

$$Q_i(E) = \frac{L_i(E)}{L_e(E)} \tag{2.6}$$

2.2 Neutron Interaction with Materials

Neutrons interact strongly with the nuclei in a given material. The interaction of neutrons with a matter is mainly through elastic scattering or they can also be absorbed by the nuclei of the material. The elastic scattering cross-section of neutrons at low energy is given as

$$\sigma_n = 4\pi(1.4 \cdot 10^{-13} A^{1/3})^2. \tag{2.7}$$

Usually B-, Li-, and Cd-based crystals are used as scintillators for detecting low-energy neutrons because of a high cross-section of these elements for neutrons. Neutrons transfer energy to nuclei of the atoms in a detector via elastic scattering, leading to the creation of ions or recoil-protons. The energy loss of the created charged particles in the material leads to scintillation, as discussed in Section 2.1.

2.3 YSO-based Implantation Detector

Implantation detectors are employed at beam facilities primarily to stop/detect the nuclei of interest. The general design of these detectors consists of stopping the ions in a material and then measuring the induced energy loss in the material. At present, most facilities around the world are using silicon-based detectors, such as AIDA [49], and WAS3ABi [50] at RIBF, RIKEN. These detectors work well overall but their timing resolution is insufficient for measurements using Time-of-Flight (ToF) methods. There is also a room for improving the beta-detection efficiency, which stands at $\sim$ 50 % for silicon-based detectors.

For ToF measurements, fast timing can be attained using selected scintillators. The neutron-rich nuclei impinged on the scintillator, by eventually coming to rest via energy loss, undergo radioactive decays emitting beta particles, γ-rays, alpha particles, and neutrons. The first step to study the decay kinematics of a nucleus using an implantation detector is to establish ion-beta correlations, *i.e.*, associating a parent nucleus to its corresponding electron partner from beta decay. The observables available for establishing correlations using an implantation detector are the average position of the interaction of ions and electrons in the scintillator and the timing information of each ion and beta event. The correlations are also crucial for determining the decay half-lives and developing a decay cascade of the precursor nuclei into subsequent daughter nuclei. In this work, for the construction of the implantation detector, Yttrium Orthosilicate (YSO) was used as the scintillator. YSO (Y_2SiO_5:Ce) has higher stopping power than Si, requiring lesser material thickness for stopping highly-energetic ions and also providing high light yield. A finer segmentation ($\sim$ 1 mm) is achievable using the YSO crystals for the desired position resolution. All the physical properties of the YSO scintillator are listed in Table 2.1.

YSO crystal offers a good combination of properties characterizing an implantation detector. The YSO emission spectrum peaks at a wavelength of 420 nm (refractive index = 1.8) and couples well with a multi-anode position-sensitive photo-multiplier (PSPMT) by Hamamatsu for maximum light collection. It also has the advantage of high light yield, good timing-resolution, short decay time, non-hygroscopic, and all-around stable physical

and chemical properties [51]. Figure 2.2 shows the YSO crystal used for constructing the detector.

Using the crystal, a new segmented scintillator-based detector was developed at the University of Tennessee, Knoxville. The detector unit consists of a segmented (2" x 2") YSO crystal. Each pixel, as well as the face and the sides of the crystal, are covered in Enhanced Specular Reflector (ESR) material to minimize any light leak. The crystal has a thickness of 5 mm and is coupled with a flat panel PSPMT (Hamamatsu, H12700). A 2-mm-thick quartz light diffuser is placed between the YSO crystal and the PSPMT to achieve sub-anode position resolution by spreading the light from one pixel onto several anodes of the PSMT. The crystal is coupled with PSPMT using organic adhesive material, Sylgard, to provide mechanical rigidity to the final detector. This design was used for BRIKEN [52] Fall 2017 campaign for commissioning.

The voltage signals induced by the scintillation light in the 64 anodes of the PSPMT were fed to a voltage dividing resistor network array provided by Vertilon, as shown in Figure 2.4. The voltage generated by each anode of the Photo-multiplier Tube (PMT) is divided by the resistor circuit into four outputs (V1, V2, V3, and V4). The four signals from the Vertilon board are decoded into a position array by calculating the *centroid* of the signal voltage, using the concept known as *Anger Logic*, named after Hal Anger [54]. The idea behind Anger Logic is conceptualized as follows: if the voltage signal of a photomultiplier is made proportional to its position, the "centroid" of the voltages produced by a particle will determine where the particle originated. The four dynode signals from the Vertilon board were processed using the following equations:

$$X = 0.5 * \frac{(X_a + Y_b)}{(X_a + X_b + Y_a + Y_b)}, Y = 0.5 * \frac{(X_a + X_b)}{(X_a + X_b + Y_a + Y_b)}. \tag{2.8}$$

Figure 2.5 shows the images from the detector reconstructed using Anger logic. The dynode signal from the Vertilon board is used for measuring energy. Figure 2.3 shows the resistor network readout of the 64 PMTs in the PSPMT.

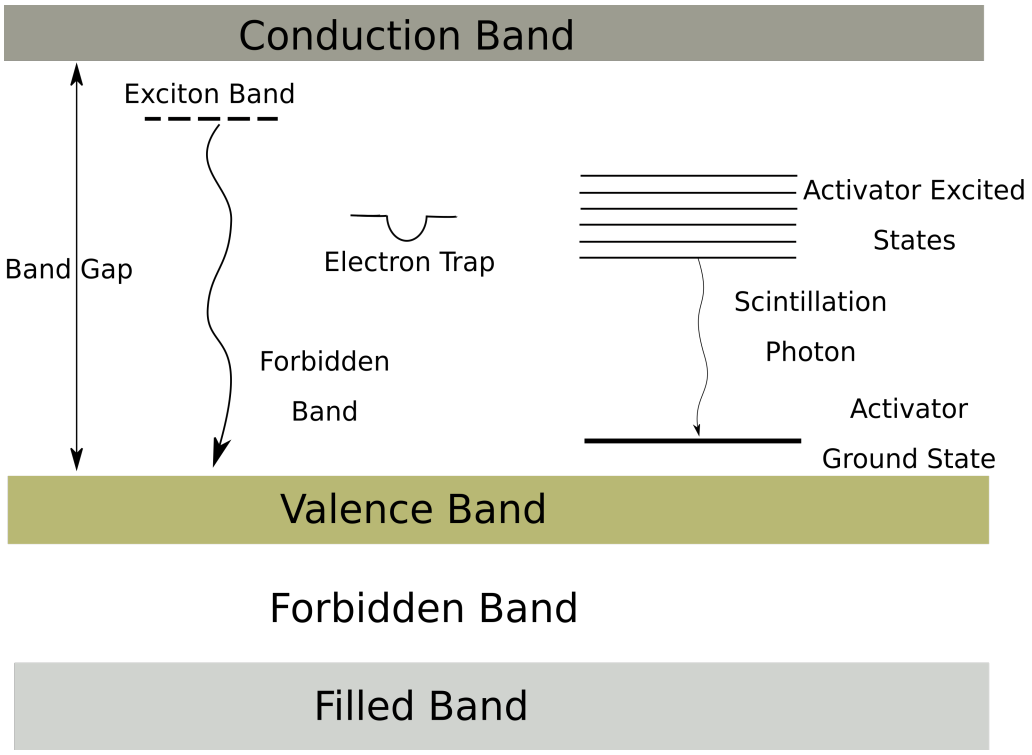


Figure 2.1: A schematic diagram explaining the scintillation mechanism in inorganic scintillators. Adapted from: *http://atlas.physics.arizona.edu/*

Table 2.1: Physical properties of YSO: Data Source: X-Z Lab [51]

Effective Z	39
Density	4.44 g/cm^3
Decay Constant	50-70 ns
Wavelength of Maximum Emission	420 nm
Melting Point	2273 K
Refractive Index of Emission	1.8 @420 nm
Hygroscopic	No

2.3.1 Testing

A number of tests were performed to examine the quality of position resolution, response of the PSPMT, and the dynamic range estimates. The height of voltage signals expected from the energy loss of heavy ions in the scintillator can be examined by using a light pulser. The estimate is needed to adjust the dynamic range in the software during the experiment. For testing the dynamic range, the entrance window of the PSPMT was illuminated with a Light Emitting Diode (LED) pulser to achieve maximum irradiance. The response of the PSPMT was tested using an LED pulser. The height of the pulser signal mimics the possible irradiance expected from heavy ions. The pulser voltage was increased in steps, and the dynode output voltage from the PSPMT was measured using an oscilloscope. The PSPMT was biased at different voltages and the results of the tests are shown in Figure 2.6. The plots show the response of the PSPMT dynode as the biasing voltage of the signal is ramped up. The input voltage is the voltage of the signal from the pulser measured using an oscilloscope. The plot shows that the saturation is reached by the PSPMT for a lower pulser voltage at a higher biasing voltage.

Range Distribution of Ions and Electrons in YSO

Isotopes present in the beam are highly energetic, with energy of the order of GeV. An estimate of the range of these ions in the YSO crystal is important from the point of view of the experiment, so that all the isotopes of interest are fully stopped in the crystal. These estimates are also important for detector design, since they are helpful in choosing the right thickness of the scintillating material. LISE++ [55] is a software program that has been developed to calculate the transmission and yields of fragments produced and collected in a spectrometer. The LISE++ code may be applied at medium-energy and high-energy facilities (fragment- and recoil-separators with electrostatic and magnetic selections). In a number of facilities, like A1900 and S800 at NSCL, LISE3, SISSI/LISE3, and SPEG at GANIL, FRS and SuperFRS at GSI, RIPS and BigRIPS at RIKEN, based on the separation of projectile-like and fission fragments, fusion residues are included or might be easily added to the existing optical configuration files. The range estimates of ions produced can be

deduced for any material by providing chemical properties of the material to LISE. Figure 2.7 shows the range distribution of various ions implanted in the YSO crystal.

Secondary ionization electrons created by the primary electron originating from the beta decay β^--decay of radioactive ions can have energy as low as a few keV or as high as a few MeV. Information about the range of electrons of various energies is also vital from the ion-β correlation perspective. It is helpful in designing and optimizing the position gates around the implant positions. These range estimates were produced using an online program called ESTAR [56]. Details about the chemical composition and density are the input parameters to the program. The program calculates stopping power, density effect parameters, range, and radiation yield tables for electrons in various materials. Figure 2.8 shows the range of electrons stopped in the YSO crystal with different electron energies.

2.3.2 YSO Detector for Time-of-Flight Spectroscopy

A YSO implantation detector with revised design and specifications was developed for performing ToF-based spectroscopy of β-delayed neutrons using VANDLE [9]. The detector acts as a fast β-trigger along with recording implanted ion positions.

Detector Design and Construction

The detector consists of a 7.5 cm $\times$ 7.5 cm segmented array of YSO crystals with a 2-mm pitch, coupled with a PSPMT by Hamamatsu, H12700B-03 (48.5 mm $\times$ 48.5 mm effective area), via a tapered and pixelated acrylic light guide shown in Figure 2.9. The light guide is used to guide the light produced through scintillation in the YSO array onto the entrance window of the PSPMT. A one-to-one correspondence between the pixels of the crystal and the light guide is ensured by UV curing the two with each other. The combined crystal and light guide system is coupled with the PSPMT using Sylgard, providing optical coupling and mechanical stability. A schematic of the completely assembled detector is shown in Figure 2.10.

The sides of the connection are sealed with epoxy glue to ensure stronger support. This variant of the implantation detector has a larger area to capture a more divergent beam spot

expected at the point of implantation at the facility. Neutron ToF to be measured is defined as follows:

$$ToF = T_{\mathrm{n}} - T_{\beta}, \tag{2.9}$$

where T_{n} is the time stamp of the neutron events recorded in VANDLE, and T_{β} is the time stamp of the beta events triggering YSO detector.

The energy of the neutrons can be deduced by the relation as follows:

$$E = \frac{1}{2} m_n \left(\frac{L}{ToF} \right)^2, \tag{2.10}$$

where $\mathrm{m_n}$ is the neutron mass, ToF is the Time of Flight, and L is the flight path. The uncertainty in the measured energy E is given by the ΔE as follows:

$$\frac{\Delta E}{E} = \sqrt{\left(\frac{2\Delta L}{L} \right)^2 + \left(\frac{2\Delta t}{t} \right)^2}, \tag{2.11}$$

where ΔL has contributions from the uncertainty in position measurement of electrons in YSO and neutrons in VANDLE [9], Δt is the timing-jitter, which is given by the root mean square of the timing resolution of YSO and VANDLE. Δt in total encompasses contributions from jitter induced by the transit-time variance of the photons in the scintillator, PSPMT response, digital electronics, intermediate noise, and timing algorithms. From equation 2.11, the uncertainty in the measured energy arises from the uncertainty in the position and timing measurements in both YSO and VANDLE.

The position uncertainty for betas in YSO is of the order of *mm*, but in contrast, the position uncertainty for neutrons is of the order of 4-5 *cm* in VANDLE. Thus, VANDLE position uncertainty dominates in determining energy uncertainty. The timing resolution of the VANDLE is of the order of *ns*, and the timing resolution for the YSO implant detector needs to be measured. For timing, measurements were performed to deduce the timing resolution of the YSO detector for signals representing various energy ranges.

Timing Performance

Tests were performed to ensure a good timing resolution for the actual experimental run. The setup for the timing measurement is shown in Figure 2.11. For time resolution measurements, a ^{60}Co source was used. ^{60}Co beta decays to the stable isotope ^{60}Ni. The excited ^{60}Ni emits two gamma rays with energies of 1.17 and 1.33 MeV. The two gamma rays are in coincidence with each other enabling timing resolution measurements. The criteria for measuring the timing resolution of the YSO detector involved getting the time stamp of the coincident gamma event in two similar YSO detectors using a ^{60}Co source and plotting the distribution of the difference in time recorded in the two detectors. The distribution can be approximated to be Gaussian. The Full-Width Half-Maximum (FWHM) of the distribution gives an estimate of the timing resolution for both detectors combined. Single detector resolution can be deduced, assuming an equal uncertainty contribution for both the detectors. Scenarios with different biasing voltages were also explored. The detector, on average, has a timing resolution better than $\sim$ 600 ps for signals representing energy $\geq$ 1 MeV. Several other tests were performed to check the image quality, quality of coupling, and position resolution. Figure 2.12 shows the results from the measurement where a sub-nanosecond resolution is determined. Figures 2.13, 2.14, and, 2.15 show the images from the detector with various sources.

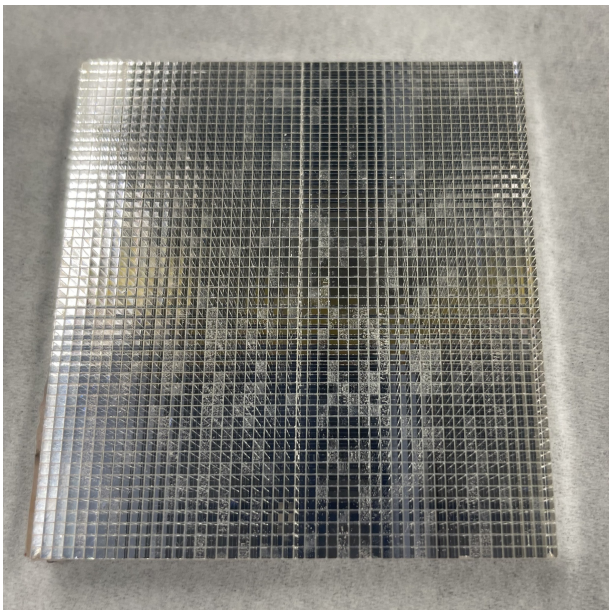


Figure 2.2: 48 × 48 pixel YSO scintillator used for building the detector. A faded line running through the crystal is the joint between two segments (24 × 48) joined together to form a larger array. The segmented crystal array is manufactured by Agile Technologies, Inc. [53]

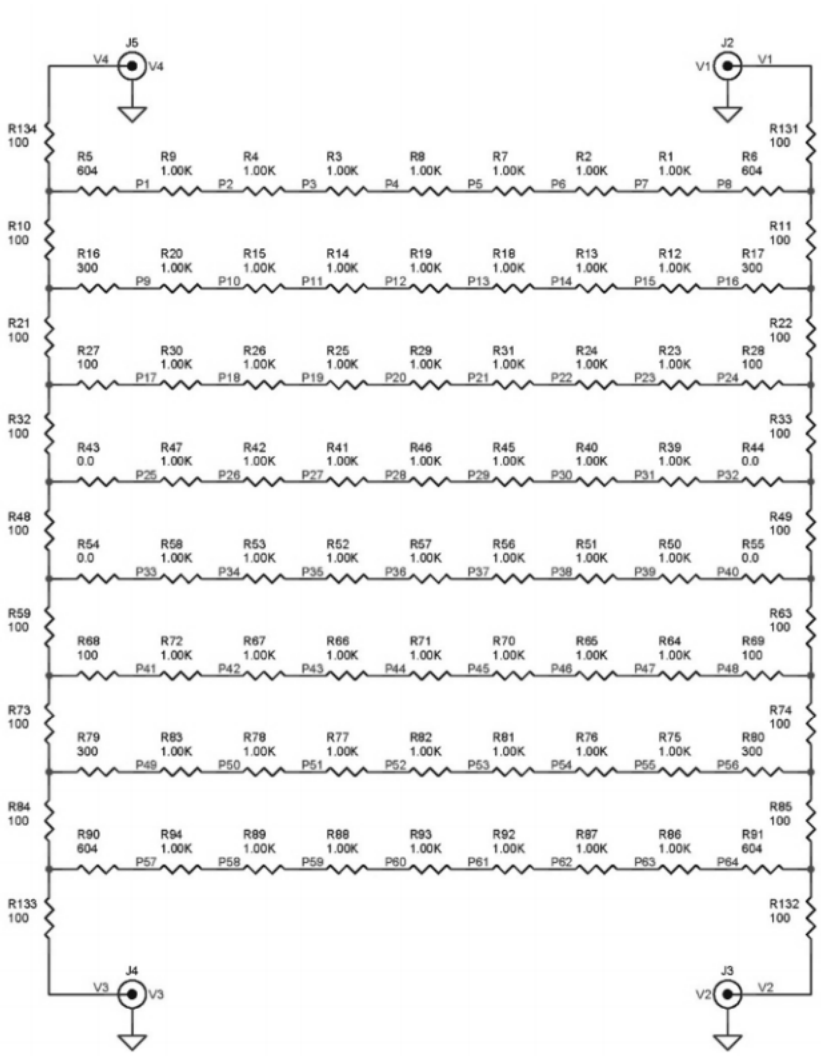


Figure 2.3: The electrical circuit of the Anger logic showing readouts for all 64 anodes (P1..P64) from the PSPMT and four output signals for position reconstruction.

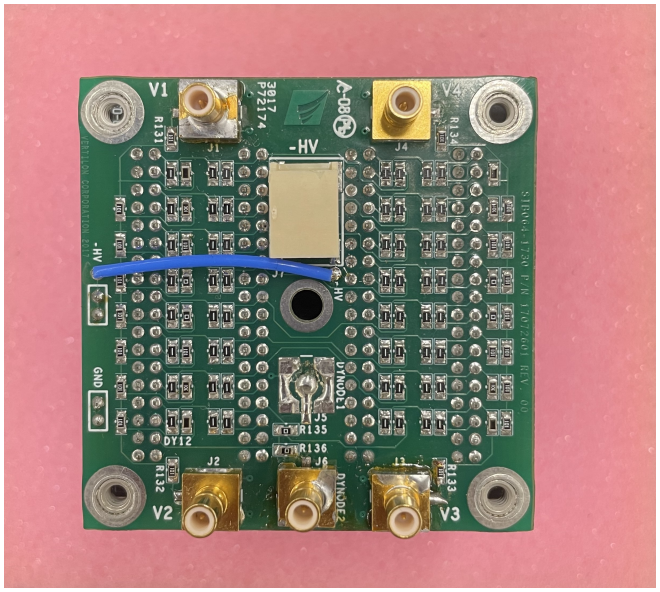


Figure 2.4: Picture of the back of the Vertilon board showing 6 SMB (SubMiniature version B) connectors for output readout. V1, V2, V3, and V4 are the anode signals and are outputs of the anger logic circuit onboard.

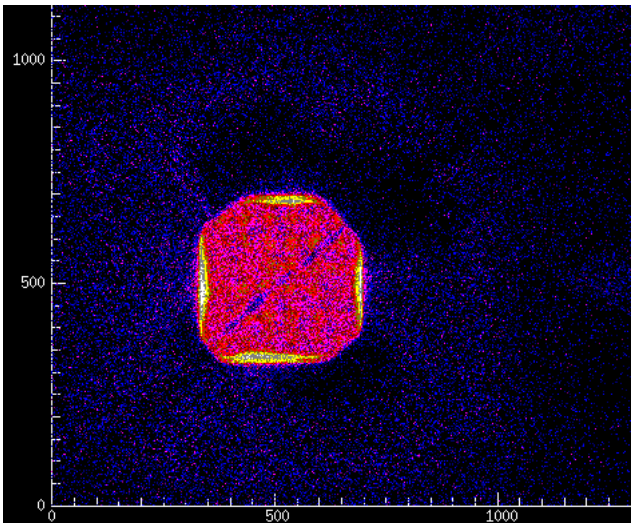


Figure 2.5: YSO crystal rotated on the face of the PSPMT, highlighting the joint in the YSO scintillator array.

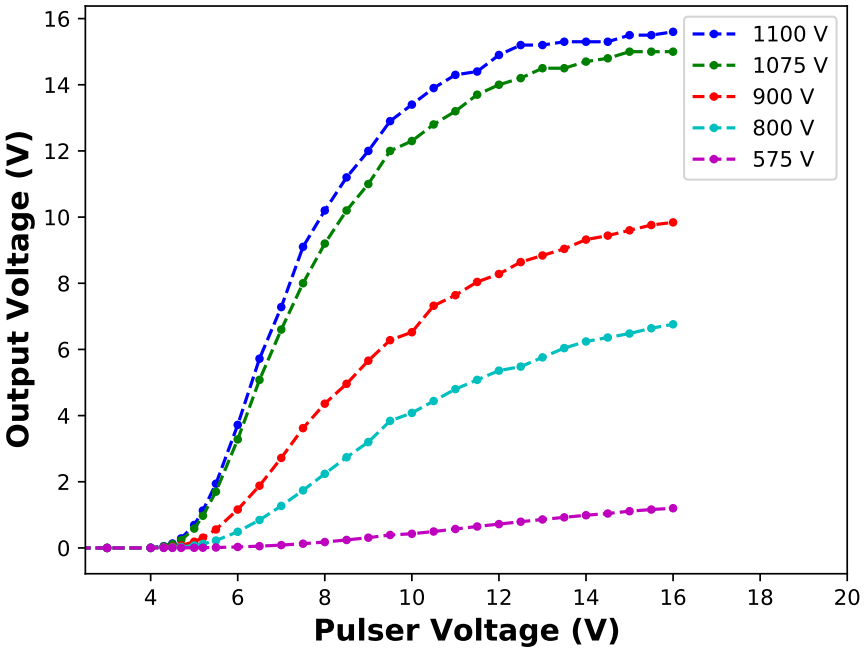


Figure 2.6: The response of the PSPMT to the pulser input voltage for five different biasing voltages from 575 V to 1100 V.

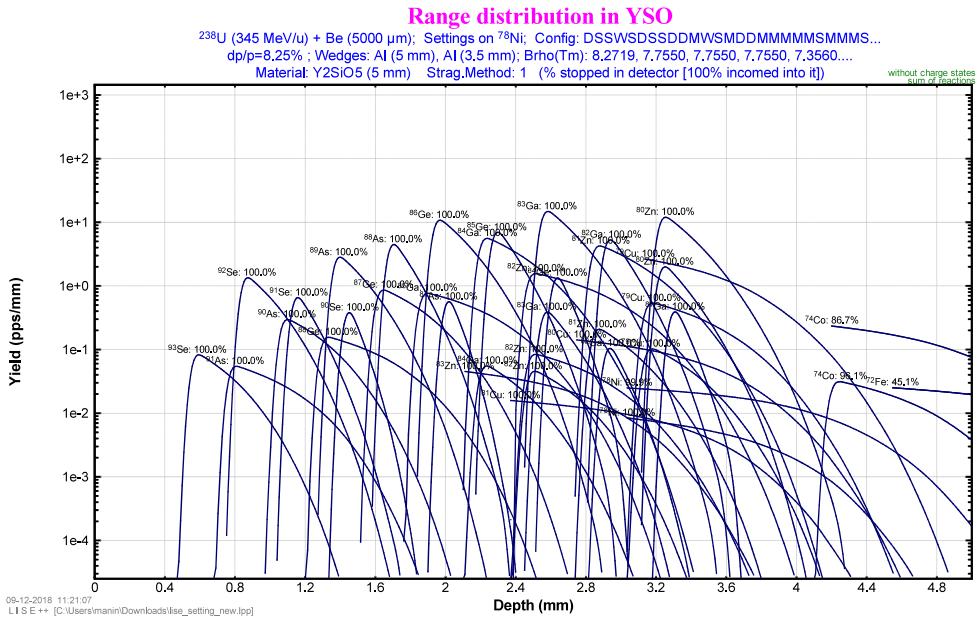


Figure 2.7: Range distribution of various ions in YSO. The configuration for the calculations is identical to the setup available at RIBF, RIKEN. The heaviest ions are implanted shallower with full absorption, while lighter ions have relatively deeper implantation, requiring proper energy degraders for total absorption in YSO.

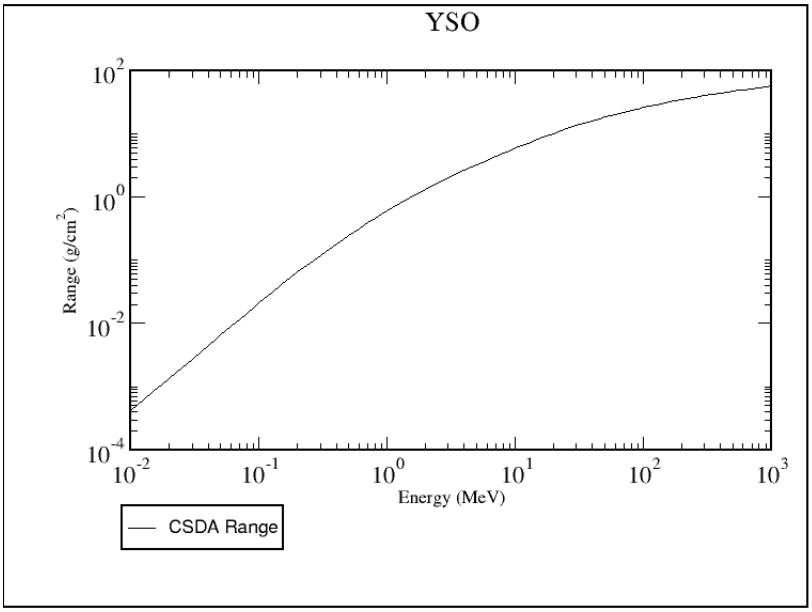


Figure 2.8: Continuous slowing down approximation range (CSDA) of electrons in YSO computed using ESTAR.

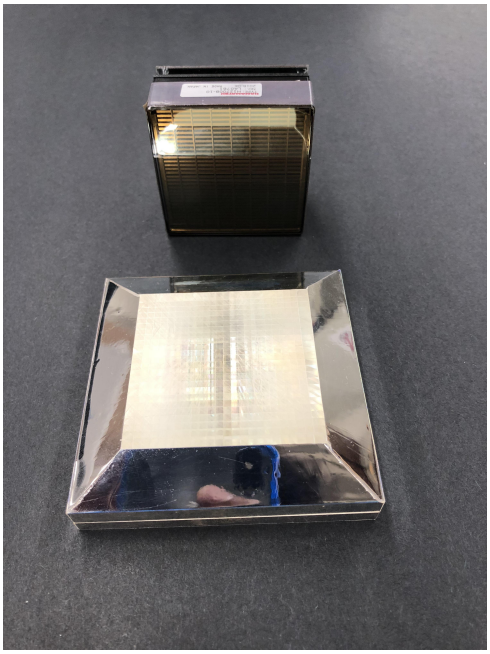


Figure 2.9: The image above shows the YSO crystal and light guide combination and the PSPMT used. The sides of the light guide are covered with ESR to ensure that the light loss is minimum.

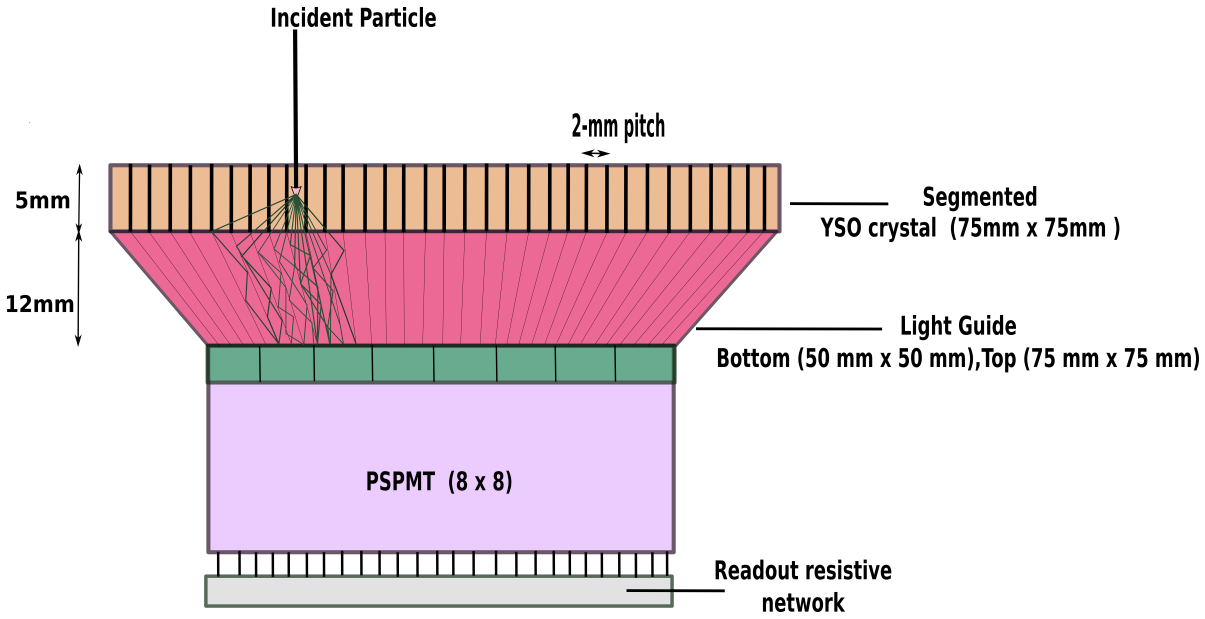


Figure 2.10: A graphical depiction of the detector design, showing the placement of the YSO crystal and light guide on the PSPMT. The pathway of photons on their way to the sensor through the light guide is shown using green-colored lines.

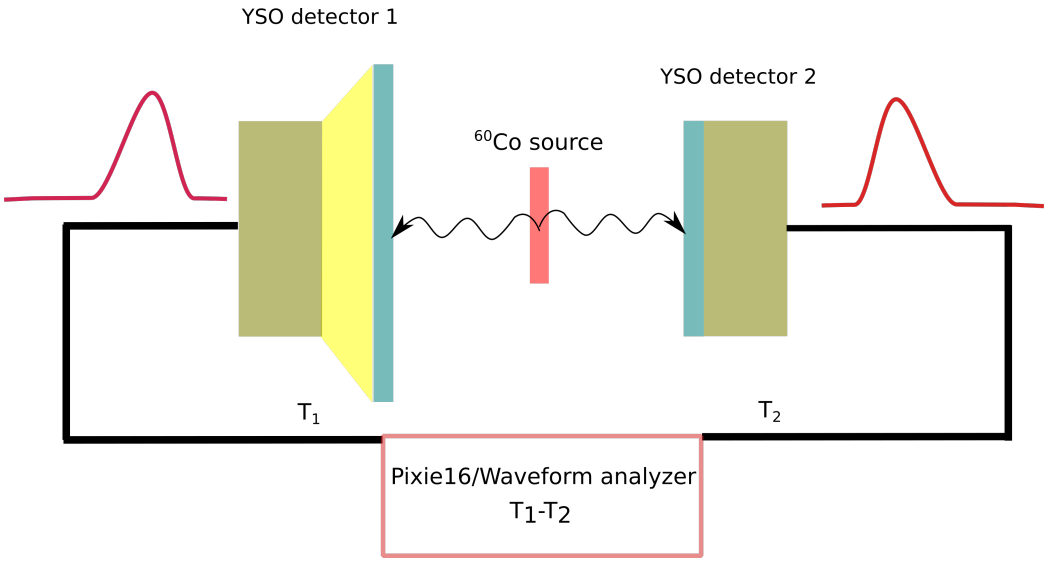


Figure 2.11: Schematic of the setup for YSO timing measurement.

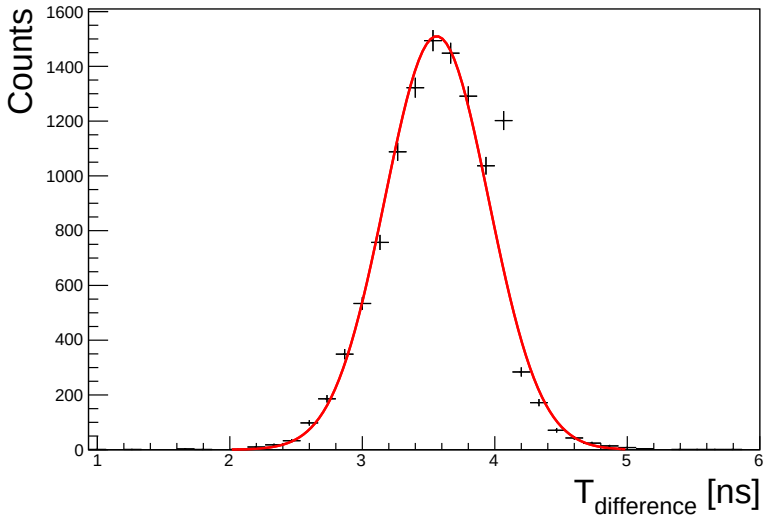


Figure 2.12: Time difference between the signals having gates for energy above the Compton edge of ^{60}Co. The distribution has a FWHM of 922 ps. This configuration offers a timing resolution of $\sim$ 650 $(922/\sqrt{2})$ ps at 600 V.

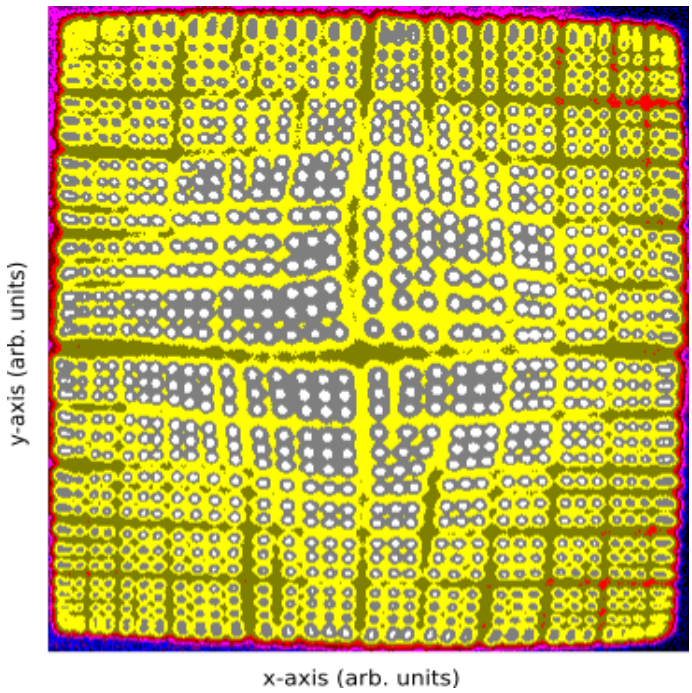


Figure 2.13: Flat-field image produced using ^{137}Cs source on an x-y plane (arbitrary scaling) showing each pixel well-illuminated. The crystal is 7.5 cm $\times$ 7.5 cm, with each pixel having a dimension of 2 mm $\times$ 2 mm. The gaps are present in the image because of how the light guide is constructed out of four different sections and joined together. The pixels on the corner are more crowded because of the relatively greater tapering of the light guide along the z-axis for the edges than for the center.

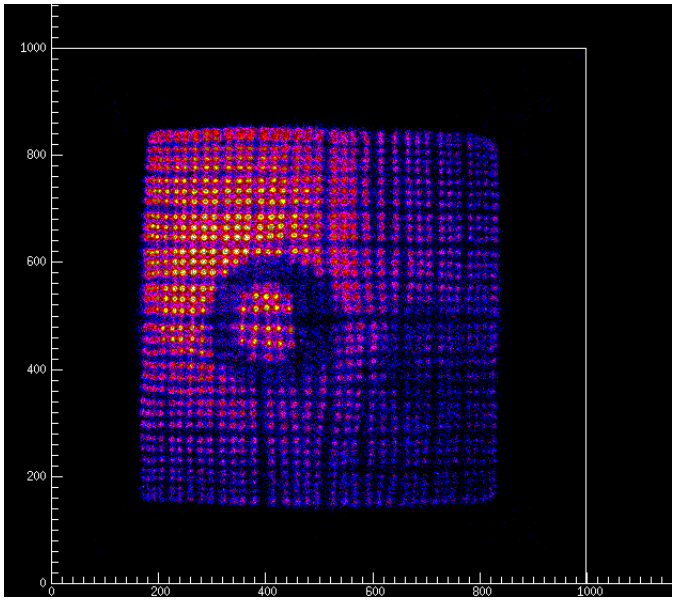


Figure 2.14: Image obtained using a ^{90}Sr source and a washer to see the shadow effects. ^{90}Sr is useful for checking YSO image resolution for electrons.

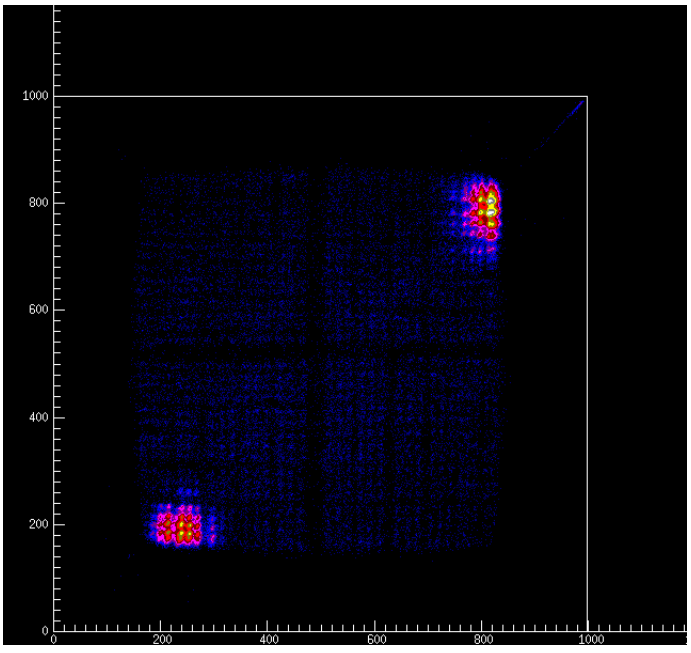


Figure 2.15: Image obtained using a ^{90}Sr placed at the corners to check for coupling, imperfections, and edge effects.

Chapter 3

Experiments

This chapter contains the details of the Radioactive Isotope Beam Factory(RIBF) at RIKEN Nishina Center, Japan. The mechanism of beam production at the facility and the setup of experiments using the BRIKEN counter and the VANDLE array at the facility will be explained.

3.1 Radioactive Isotope Beam Factory (RIBF) at RIKEN

The RIBF is a world-class facility using heavy-ion fragmentation as a primary method of radioactive ion-beam production. Figure 3.1 shows a schematic view of the facility. The RIBF consists of accelerators used in a 25-year-old facility (since 1986) and new systems completed more recently. The old facility used the heavy-ion accelerator complex consisting of a K540-MeV ring cyclotron (RRC) and its two injectors: a variable-frequency heavy-ion linac (RILAC) and a K70-MeV AVF cyclotron (AVF). These accelerators have been providing a lot of users in various research fields with the worlds most intense ion beams over the whole range of elements. The RILAC provides a heavy-ion beam with energy up to 6 MeV/nucleon. The AVF provides protons up to 14 MeV and Ca ions up to 5.6 MeV/nucleon. The RRC can provide protons up to 210 MeV, heavy ions such as C, O and Ne ions up to 135MeV/nucleon, Ar ions up to 95 MeV/nucleon, and Bi ions up to 15 MeV/nucleon. Moreover, the projectile-fragment separator at the RRC (RIPS) provided the world's most intense low-atomic mass (<60) RI beams. The RIBF added new dimensions to the facility's

capabilities: a new high-power heavy-ion booster system consisting of three-ring cyclotrons with K=570 MeV (fixed frequency, fRC), 980 MeV (intermediate stage, IRC), and 2500 MeV (superconducting, SRC), respectively, can boost energies of the output beams from the RRC up to 440 MeV/nucleon for light ions and 350 MeV/nucleon for very heavy ions. The goal of the available intensity was set to be 1 pμA, which is restricted due to the radiation shielding power around a primary-beam dump. The superconducting isotope separator, BigRIPS, converts these energetic heavy-ion beams into intense RI beams via the projectile fragmentation of stable ions or the in-flight fission of uranium ions. The combination of the SRC and the BigRIPS expands the range of delivered isotopes dramatically for experimental studies.

BigRIPS is an in-flight RI beam separator available at RIBF for the production of intense RI beams with a wide range of masses and isospin. Figure 3.2 shows the components of the BigRIPS separater. The characteristic features of the BigRIPS separator are large ion-optical acceptances and a two-stage structure. The angular acceptances are $\pm$40 mrad horizontally and $\pm$50 mrad vertically, and the momentum acceptance is $\pm$3 %, allowing efficient collection of fragments produced by not only projectile fragmentation but also in-flight fission of a ^{238}U beam. The large acceptances are achieved by the use of superconducting quadrupoles with large apertures. The two-stage structure allows delivery of tagged RI beams and two-stage isotope separation. The first stage of the BigRIPS separator is used for the production, collection, and separation of RI beams with an energy degrader, while particle identification of RI beams (separator-spectrometer mode) and/or further isotope separation with another energy degrader (separator-separator mode) is performed in the second stage. The particle identification is based on the TOF-Bρ -ΔE method, in which the time of flight (TOF), magnetic rigidity (Bρ), and energy loss (ΔE) are measured to deduce the atomic number (Z) and the mass-to-charge ratio (A/Q) of RI beams. Such in-flight particle identification is an essential requirement for delivering tagged RI beams, making it possible to perform various types of experiments, including secondary reaction measurements. Since the total kinetic energy is not measured in this scheme, and consequently A and Q cannot be determined independently, the resolution in A/Q must be high enough to identify the charge state Q of

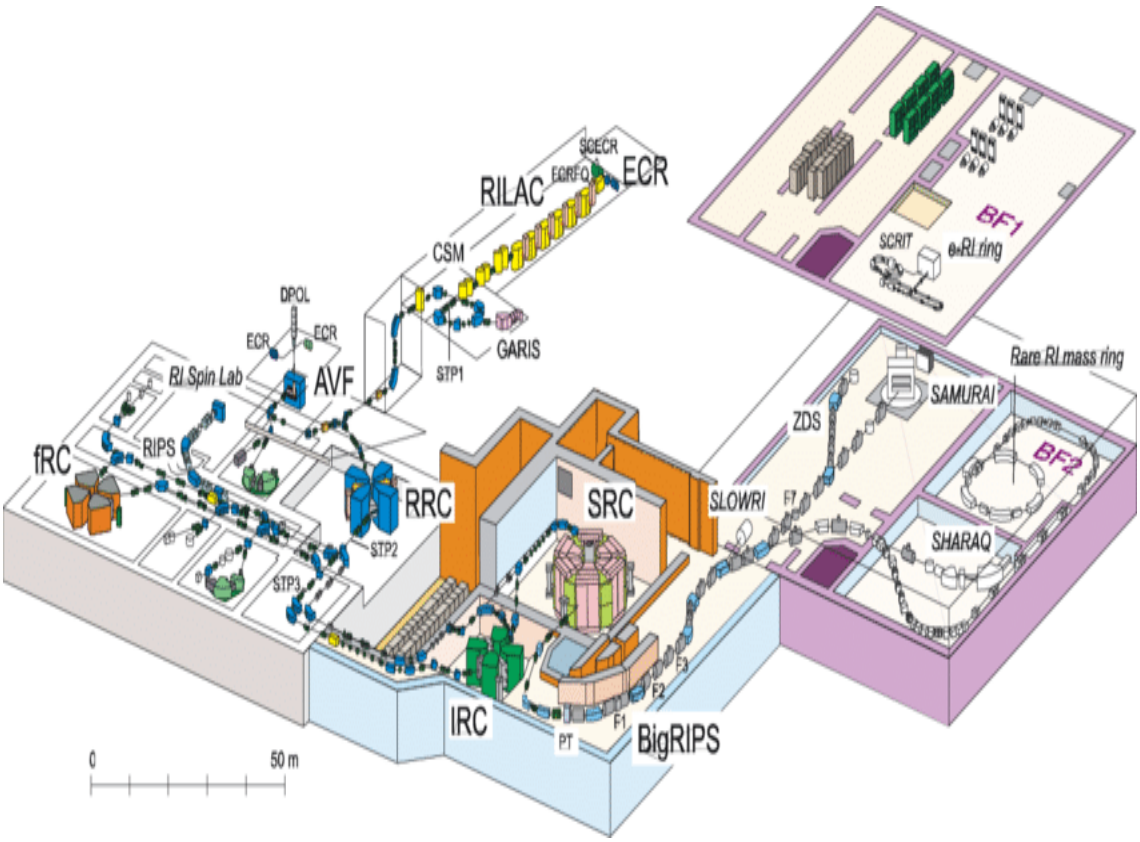


Figure 3.1: Layout of the RIBF showing various accelerators and the BigRIPS ion separator [57].

RI beams. Furthermore, the flight path is fairly long (46.6 m) for ToF measurements used for ion identification.

3.1.1 BRIKEN Experiment

The YSO detector was used for the first time at RIBF, RIKEN in two consecutive experiments. It was implemented as a part of the BRIKEN [52] neutron counter already present at the facility. The experiments involved accelerating ^{238}U primary beam to 345 MeV/nucleon with a charge state of (86+) which is the primary beam, followed by hitting a 4-mm-thick rotating target of ^{9}Be. The reaction leads to the synthesis of a gamut of exotic isotopes which are tagged and separated by the BigRIPS facility on an event-by-event basis. This tagged secondary beam of ions provided by the BigRIPS facility was implanted onto the detector with a particular combination of aluminum degraders required to monitor the energy and range of ions. The secondary beam used in the first experiment was centered around ^{82}Cu, and the second experiment itself involved two mass settings. The first setting involved nuclei around ^{115}Nb, and the second setting provided nuclei centered around ^{100}Br. The YSO detector was used as one of the implant detectors along with WAS3ABI and AIDA. The PSPMT of the YSO detector was optimized to operate at a biasing voltage of 575 V to get the desired dynamic range for the ions and betas with minimum saturation. The five signals (four positions and one energy) from the detector were split and used with different gain settings. One set of signals was devoted to implant position and energy measurements with no amplification. The other set was used for calculating the energy and position of the betas, with an amplification of $\sim$ 10 for obtaining a good signal-to-noise ratio leading to better estimates of energy and position. Figure 3.3 shows the layout of the experiment, and Figure 3.4 shows the particle identification of the ions stopped in the YSO crystal.

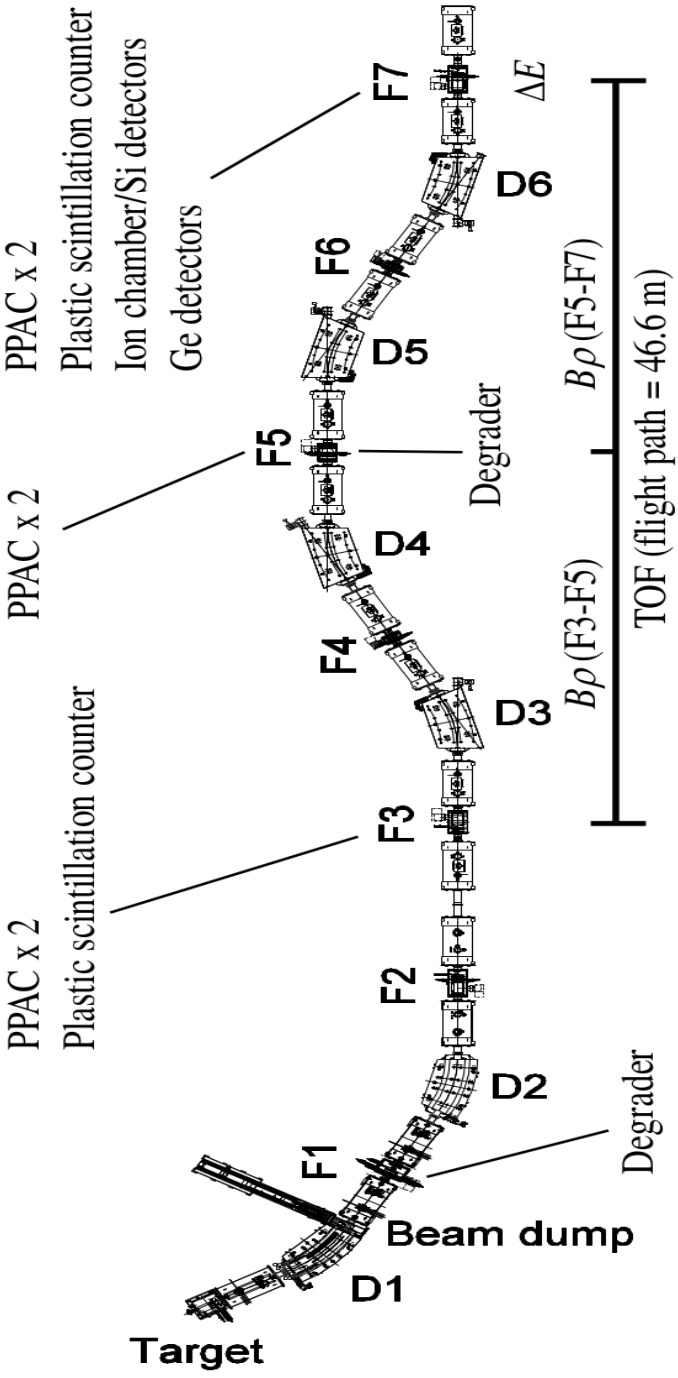


Figure 3.2: Schematic diagram of the BigRIPS separator at RIBF. The first stage includes the components from the production target (F0) to F2, while the second stage spans those from F3 to F7 [58].

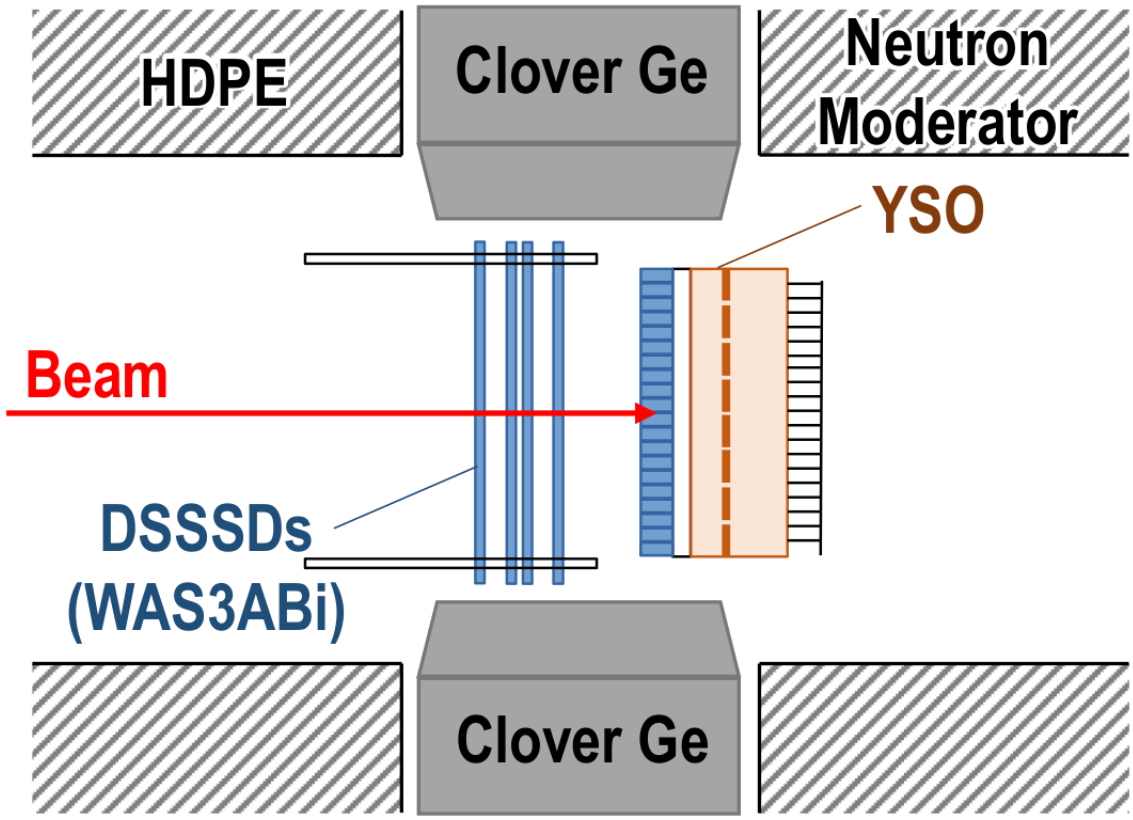


Figure 3.3: A diagram showing the instrumental setup for the experiment as viewed from above. WAS3ABi and YSO are placed in a cavity at the center of the BRIKEN neutron detector, approximately 2-cm apart. This position geometrically ensures the detection of maximum possible neutrons (prompt and delayed) by the neutron counter. The High-Density Polyethylene (HDPE) is used to moderate energetic delayed neutrons, advancing them in a region of high interaction cross-section with the ^{3}He tubes comprising the BRIKEN neutron counter. Two High-purity Germanium (HPGe) clover detectors were employed to record the β-correlated γ-rays.

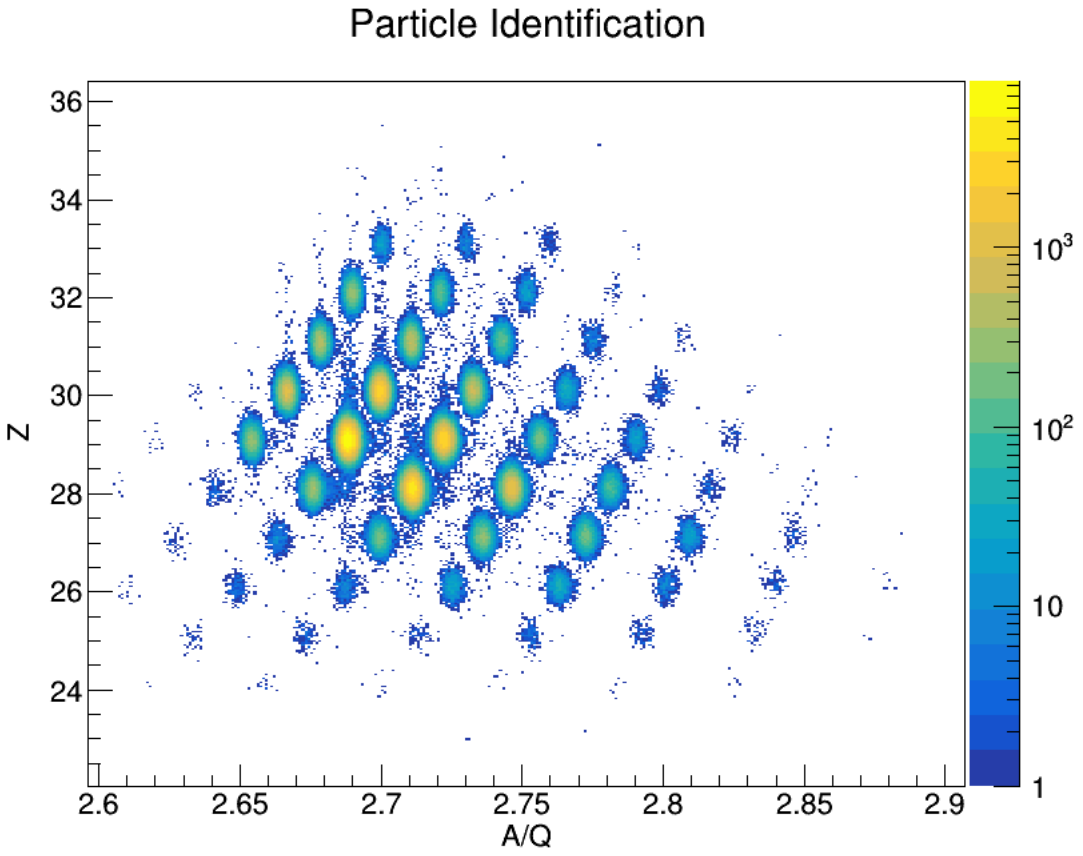


Figure 3.4: Particle identification plot for ions stopped in YSO. This information is provided by the BigRIPS facility and is important for ion-specific analysis.

3.2 Neutron Spectroscopy using VANDLE at RIBF, RIKEN

Versatile Array of Neutron Detectors at Low Energy (VANDLE) comprises a set of elongated neutron detectors capable of detecting neutron energy ranging from $\sim$ 100 keV to 8 MeV. Each individual neutron detector is made up of an Eljen-EJ200 organic scintillator bar, coupled to a Photomultiplier Tube (PMT) on both sides to collect the light produced. Figure 3.5 depicts the construction of a VANDLE bar. Based on the dimension of the scintillator used, the individual detectors are classified as small, medium, and large. VANDLE offers good timing and spatial resolution [9] for measuring neutron energy. For the experiment, a set of 48 medium ($3\times$ 6 $\times$ 180 cm^3) bars arranged in a semi-circular fashion with a diameter of 210 cm was used. Figure 3.6 shows the placement of the detector setup in the experiment hall. The figure also shows the BRIKEN neutron counter through which the beam passes on its way to the YSO detector.

Alongside VANDLE and YSO, two High-Purity Germanium Detectors (HPGe) and a total of 10 $LaBr_3$ detectors were placed around an implantation box to detect γ excitations. The implantation box is a 3D-printed plastic box containing the YSO-based (75 $\times$ 75 $\times$ 5 mm^3) implantation detector, an EJ200 plastic (75 $\times$ 75 $\times$ 5 mm^3) detector with four SiPM readouts as front VETO, and another EJ200 plastic (75 $\times$ 75$\times$ 6 mm^3) detector with two SiPM readouts as back VETO. The placement of the detectors relative to each other in the implantation box is shown in Figure 3.8. Signals from all the detectors were monitored and recorded using digital electronics modules called Pixie-16 [59] by XIA. Each module has 16 channels with four Field Programmable Gate Arrays (FPGA) and a fast sampling analog-to-digital converters, digitizing the signal at a rate of 250 Mega samples per second with 12-bit precision. A closer view of the setup is shown in Figure 3.7. The setup was further downstream of the F11 focal plane. The beam production method at RIBF is explained in Section 3.1.1. The fission fragments were selected to be in the vicinity of ^{78}Ni by the BigRIPS [58]. The whole experimental campaign lasted for about 5.5 days. The region of isotopes implanted in YSO during the experiment is shown in Figure 3.9.

3.2.1 Trigger Scheme for the Experiment

Figure 3.10 shows how signals from the YSO detector were used in low (ions)- and high (beta)- gain settings. The signals for the low-gain branch were attenuated and fed to Pixie-16 channels with a low-gain ($\times$ 0.25) input setting. On the other hand, signals for the high-gain branch were amplified using a Philips amplifier and were plugged into pixie-16 channels with a high-gain ($\times$ 1) input setting. The dynode signal from the high-gain branch was further split into two. One of these signals was used in a triple-coincidence with the signals from the left and right PMTs of the VANDLE. The triple-coincidence trigger method prevents noise accumulation in the VANDLE bars and reduces the amount of data collected. Figure 3.11 shows the schematic of the triggering scheme implemented for all the detectors in the experiment.

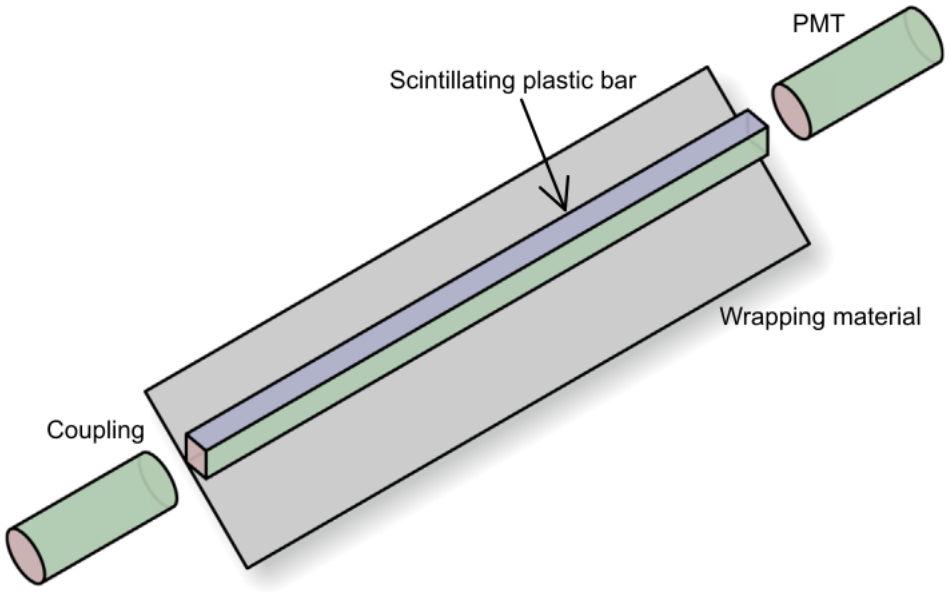


Figure 3.5: A diagram depicting the construction of a VANDLE bar, showing the Mylar wrapping and the coupled PMTs at both the ends [9].

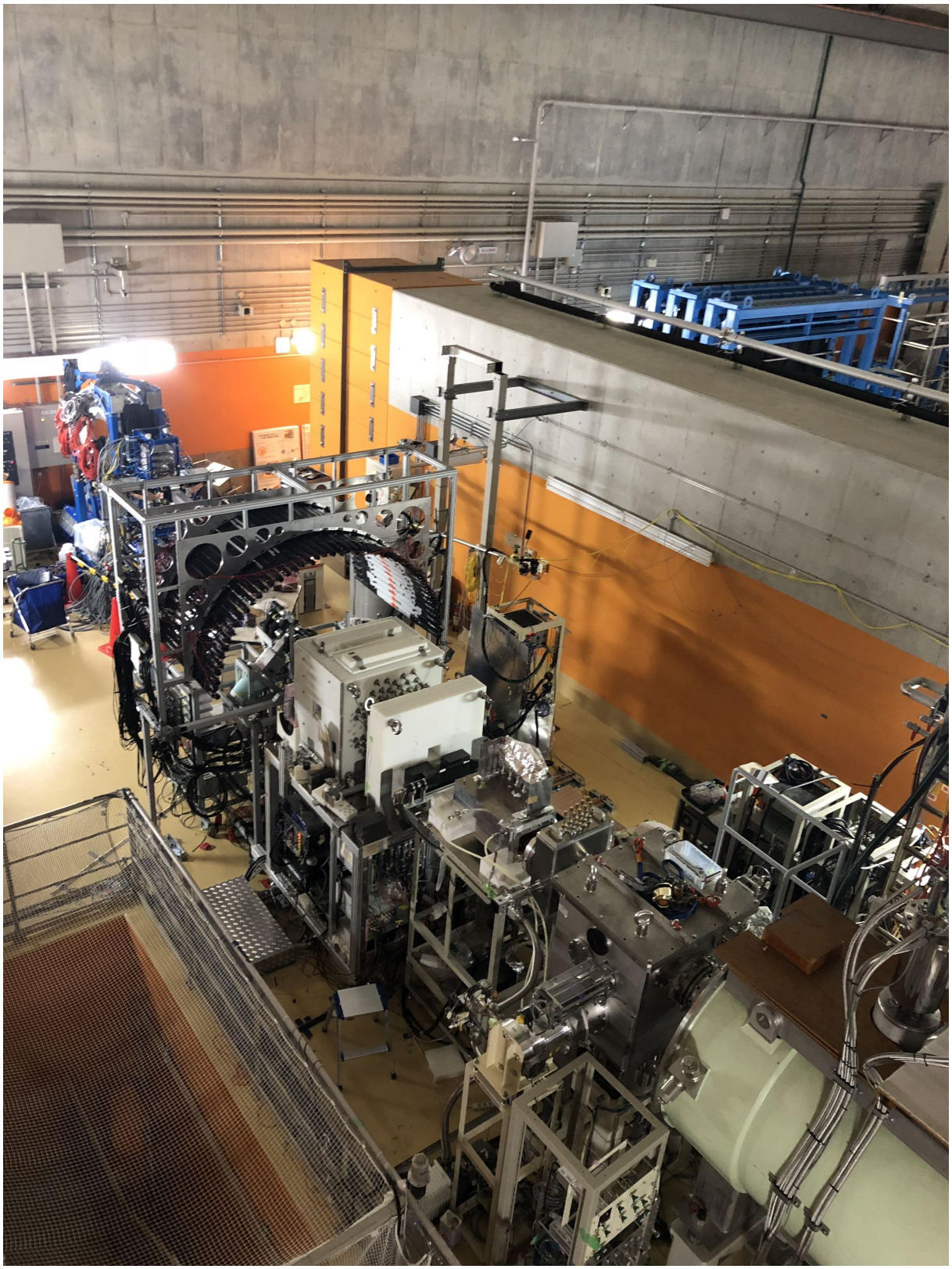


Figure 3.6: A picture of the experiment hall showing the BRIKEN neutron counter and the setup for the VANDLE experiment.

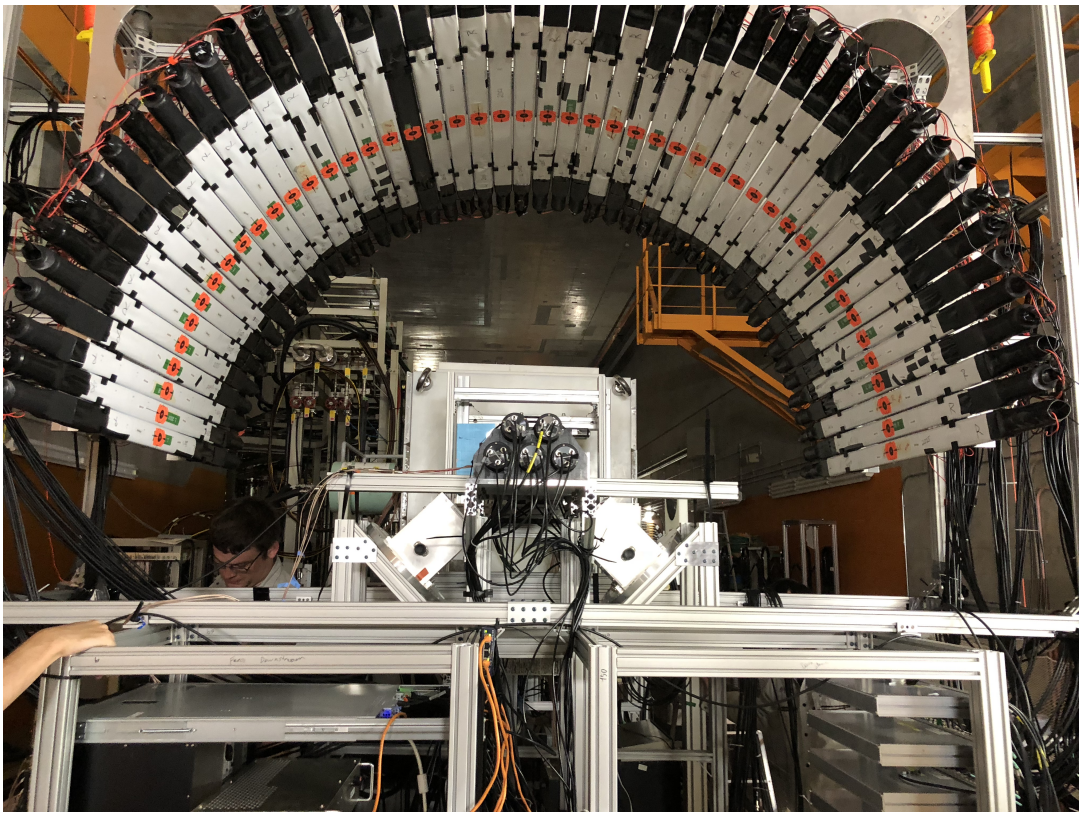


Figure 3.7: The picture shows the site of the experimental setup at RIBF, RIKEN, for the experiment employing VANDLE. The setup consists of 48 VANDLE bars, an implantation box, two High-purity Germanium detectors setup at 90 degrees angle to each other, and 10 $LaBr_3$ detectors.



Figure 3.8: Photograph showing the 3D-printed implantation box containing the front plastic detector, YSO implantation detector, and VETO detector.

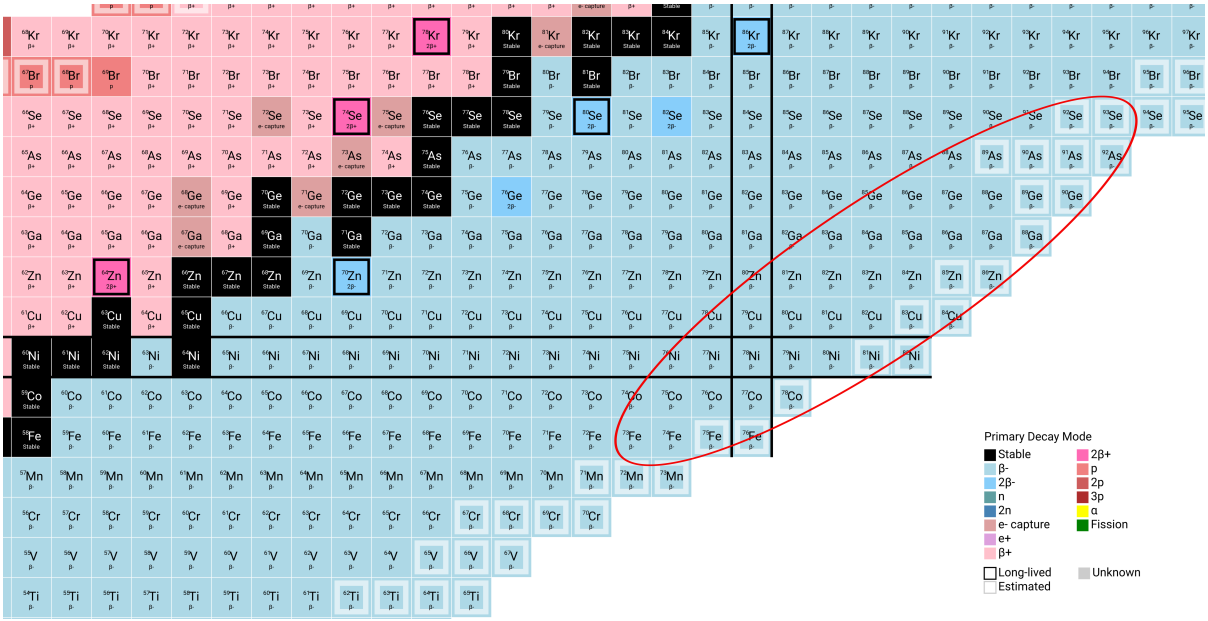


Figure 3.9: Selected portion of the nuclei chart, showing the region explored in the experiment, demarcated by a red ellipse.

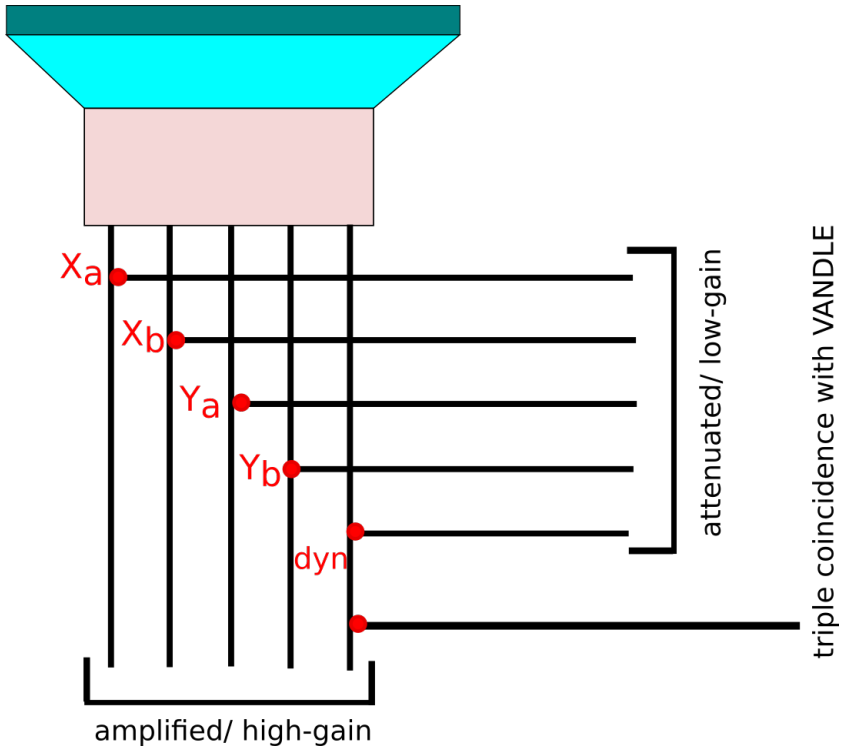


Figure 3.10: Division of the 5 YSO signals into low- and high-gain branches. A red dot denotes a split in the signal.

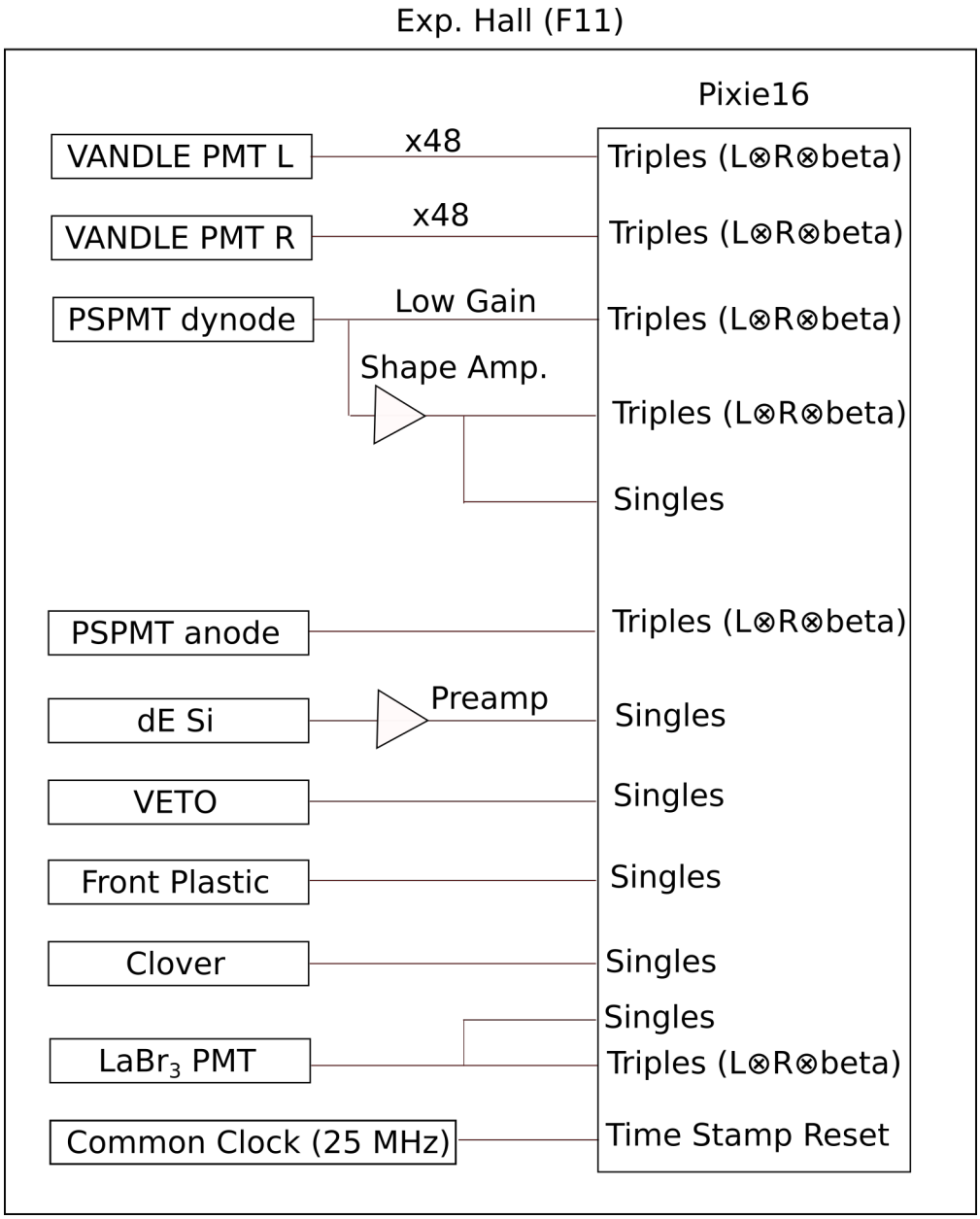


Figure 3.11: Triggering scheme adopted for the experiment.

Chapter 4

Analysis

This chapter describes the methods developed and implemented for analyzing data from the BRIKEN and VANDLE experiments. The analysis can be broadly categorized as image reconstruction of ion and beta images using YSO, efficiency determination of High-purity Germanium Detectors (HPGe), and neutron-detection efficiency and the response of the VANDLE array.

4.1 BRIKEN Experiment

Ion-β Correlations

The essential purpose of the YSO implantation detector in this experiment is to establish the correlations between implanted ions and the corresponding β-decay electrons. These correlations are implemented by using a position-gate around the position of the implanted ion in the x-y plane. Figure 4.1 depicts the algorithm adopted for establishing ion-beta correlations. The gate is optimized to achieve high beta-detection efficiency. The correlations are used to calculate half-lives of various isotopes and to further investigate the decay chains involving neutron emission or γ-ray excitation. The implementation of the correlation methodology was verified by calculating the half-lives of known isotopes.

To implement the correlations in the software, a pixel-location finding algorithm was used for both beta and ion images. A position map was constructed containing pixel ID, position

co-ordinates (X_β, Y_β) of a pixel in the beta image, and position co-ordinates (X_{ion}, Y_{ion}) of the same pixel in the ion image. The ion and beta events that satisfied the following criterion:

$$\sqrt{(X_\beta - X_{ion})^2 + (Y_\beta - Y_{ion})^2} < r, \tag{4.1}$$

were correlated. In the equation, r is the correlation radius that can be optimized for high beta-detection efficiency. Figure 4.2 shows the correlations between β and implantation events. The correlation is manifested in the form of a hot spot in the implant image in the vicinity of the β-event on the image scale.

4.1.1 Half-life Determination

The decay curve obtained from the ion-beta correlations not only contains the activity of the parent nucleus but also of the descendants. During the process of establishing ion-beta correlations, the beta events from the decay of the daughter or the granddaughter nuclei may also be correlated with the activity of the parent nucleus, if the decay of the descendants takes place within the chosen correlation radius and the chosen ion-beta timing window (T). The number of beta events correlated from the decay chains also depends on the half-lives of these nuclei. The nuclei in the ^{78}Ni region have half-lives of the order of *ms* with considerable $P_{n,2n}$ values. To calculate the half-life of any given nucleus, it is important to take into account these beta-delayed neutron decay channels alongside β decay channels, when the decay curve is analyzed for fitting and counting β events corresponding to the parent nucleus. To demonstrate, Figure 4.3 shows the decay channels of a hypothetical nucleus capable of β-delayed neutron emission and decay of which leads to radioactive products.

Figure 4.3 shows a scenario where a nucleus possesses βn and β2n decay modes. The subsequent decay products are also radioactive leading to further β decay or neutron emission. The decay of a nucleus involving such multiple decay mechanisms can be understood by solving the Bateman Equations [61] describing abundance and activity in a decay chain as a function of time. If we start with a parent nucleus $X1$ with initial activity $X1_0$ and decay constant λ_1, the number of disintegrations of $X1$ in a unit time is given as

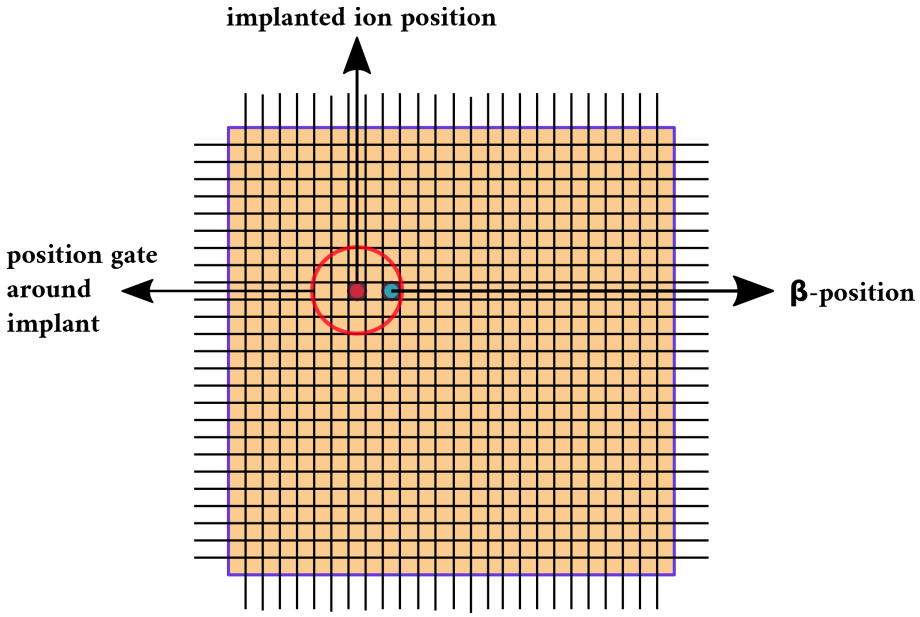


Figure 4.1: A graphical representation of the algorithm devised to identify ion-beta correlations, showing a valid association. The diagram shows ion and beta positions with red and blue shaded circles, respectively.

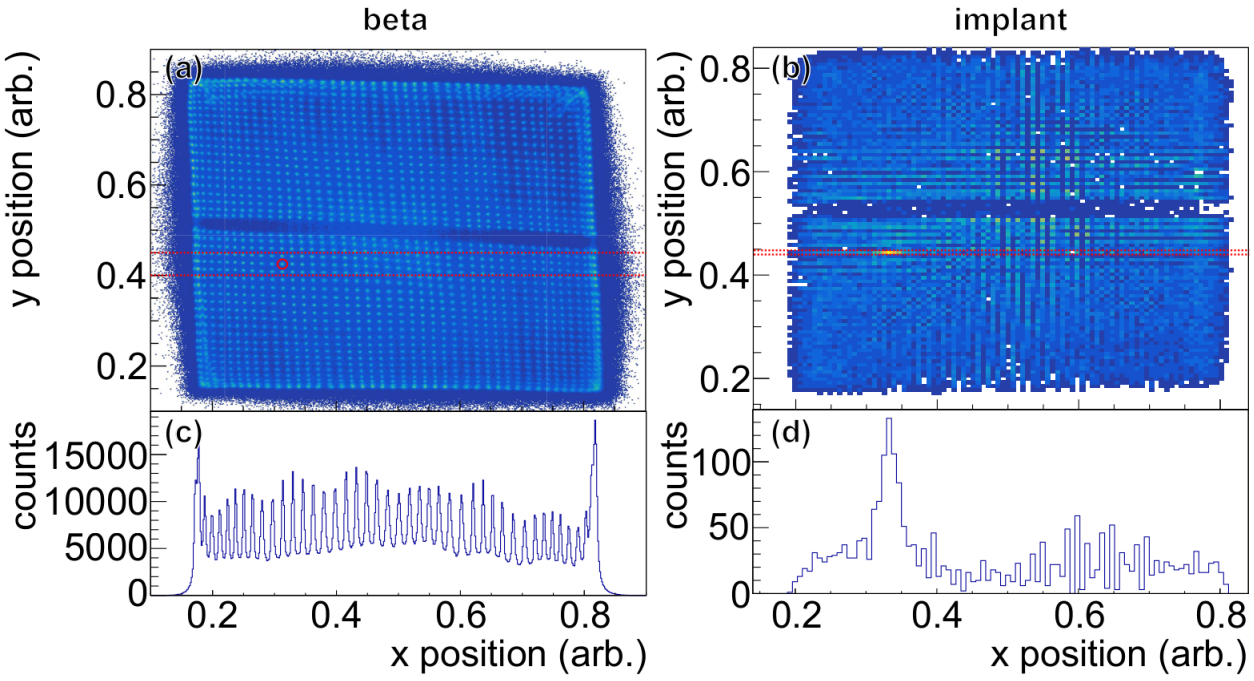


Figure 4.2: YSO x-y images of (a) β events and (b) implantation events correlated to the β events in a segment shown in the red circle in panel (a). (c) and (d) are the projection of (a) and (b), respectively, onto the x-axis in the cut shown by the red dashed lines [60].

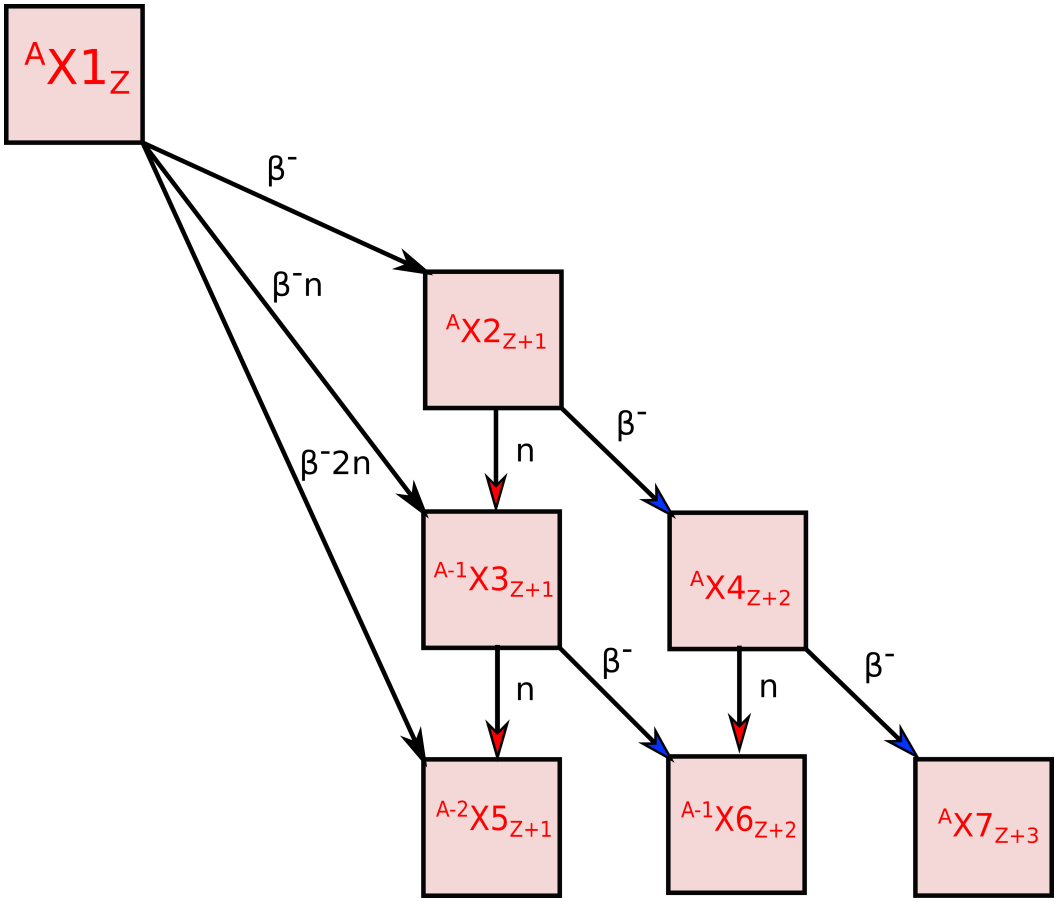


Figure 4.3: Decay of a hypothetical nucleus (X1), capable of β-delayed neutron emission and decay of which leads to radioactive products ($X2, X3, X4, X5, X6$, and $X7$) contributing to the decay curve.

$$\frac{dX1(t)}{dt} = -\lambda_1 X1(t). \tag{4.2}$$

Similarly for daughter and granddaughter nuclei, the Equations are as follows:

$$\frac{dX2(t)}{dt} = -\lambda_2 X2(t) + \lambda_1 P_{\beta 1} X1(t), \tag{4.3}$$

and

$$\frac{dX4(t)}{dt} = -\lambda_4 X4(t) + \lambda_2 P_{\beta 2} X2(t), \tag{4.4}$$

where $\lambda_{2,4}$ are the decay constants of daughter ($X2$) and granddaughter ($X4$), respectively. $P_{\beta 1,2}$ are the β decay branching ratios of $X1$ and $X2$, respectively. Equations 4.2, 4.3, and 4.4 are coupled differential equations and are solved with given initial conditions ($X1(t=0) = X_o$; $X2(t=0) = X4(t=0) = 0$). The solutions are as follows:

$$X1(t) = X_o \exp(-\lambda_1 t), \tag{4.5}$$

$$X2(t) = X_o P_{\beta 1} \left(\frac{\lambda_1}{\lambda_2 - \lambda_1} \right) \left(\exp(-\lambda_1 t) - \exp(-\lambda_2 t) \right), \tag{4.6}$$

and

$$X4(t) = X_o P_{\beta 1} P_{\beta 2} \lambda_1 \lambda_2 \left(\frac{\exp(-\lambda_1 t)}{(\lambda_2 - \lambda_1)(\lambda_4 - \lambda_1)} + \frac{\exp(-\lambda_2 t)}{(\lambda_1 - \lambda_2)(\lambda_4 - \lambda_2)} + \frac{\exp(-\lambda_4 t)}{(\lambda_1 - \lambda_4)(\lambda_2 - \lambda_4)} \right). \tag{4.7}$$

We can write a similar set of Equations for βn decay channel.

$$\frac{dX3(t)}{dt} = -\lambda_3 X3(t) + \lambda_1 P_{\beta n} X1(t), \tag{4.8}$$

$$\frac{dX5(t)}{dt} = -\lambda_5 X5(t) + \lambda_1 P_{\beta 2n} X2(t), \tag{4.9}$$

and

$$\frac{dX6(t)}{dt} = -\lambda_6 X6(t) + \lambda_3 P_{\beta 3} X3(t) + \lambda_2 P_{\beta n_2} X2(t) \tag{4.10}$$

Where λ_i is the decay constant of Xi nucleus, and $P_{\beta n}$ and $P_{\beta 2n}$ are one- and two-neutron emission branching ratios, respectively, of nucleus $X1$. $P_{\beta n_2}$ is the one-neutron emission branching ratio of the $X2$ nucleus.

Substituting Equations 4.5-4.7 in the differential Equations 4.8-4.10, we obtain the solutions as follows:

$$X3(t) = X_o P_{\beta n} \left(\frac{\lambda_1}{\lambda_3 - \lambda_1} \right) \left(\exp(-\lambda_1 t) - \exp(-\lambda_3 t) \right), \tag{4.11}$$

$$X5(t) = X_o P_{\beta 2n} \left(\frac{\lambda_1}{\lambda_5 - \lambda_1} \right) \left(\exp(-\lambda_1 t) - \exp(-\lambda_5 t) \right), \tag{4.12}$$

and

$$\begin{aligned} X6(t) = X_o P_{\beta 1} P_{\beta n_2} \lambda_1 \lambda_2 \left(\frac{\exp(-\lambda_1 t)}{(\lambda_2 - \lambda_1)(\lambda_6 - \lambda_1)} + \frac{\exp(-\lambda_2 t)}{(\lambda_1 - \lambda_2)(\lambda_6 - \lambda_2)} + \frac{\exp(-\lambda_6 t)}{(\lambda_1 - \lambda_6)(\lambda_2 - \lambda_6)} \right) + \\ X_o P_{\beta n} P_{\beta 5} \lambda_1 \lambda_3 \left(\frac{\exp(-\lambda_1 t)}{(\lambda_3 - \lambda_1)(\lambda_6 - \lambda_1)} + \frac{\exp(-\lambda_3 t)}{(\lambda_1 - \lambda_3)(\lambda_6 - \lambda_3)} + \frac{\exp(-\lambda_6 t)}{(\lambda_1 - \lambda_6)(\lambda_5 - \lambda_6)} \right). \end{aligned} \tag{4.13}$$

The number of β decays per unit time as a function of time is given by the equation:

$$\frac{dN_\beta}{dt} = -\sum_i Xi.\lambda_i + B, \tag{4.14}$$

where the summation is over all the nuclei considered in the decay chain for a given correlation window (T) and B denotes the constant background due to random correlations in the YSO. The half-life of the parent nucleus $X1$ is obtained by fitting the decay curve with the equation for $\frac{dN_\beta}{dt}$. The input parameters to the fitting equation include the decay constants (λ_i) and neutron-emission probabilities. These values can be taken from the literature or can be given as free parameters if unknown. A Maximum likelihood fitting library provided by the ROOT Cern package was used to fit the decay curve of ^{74}Co using the Bateman equations. Figure 4.4 shows the fit and various components of the decay deconvolved in the decay of ^{74}Co.

4.1.2 Light Quenching in YSO

The idea of quenching can be restated as the amount of light produced by ions relative to the amount of light produced by electrons at the same energy. To quantify the quenching of light produced by ions in the YSO crystal, it is important to have an estimate of the total energy implanted by the ions in the YSO. The energy distribution of the impinging beam on the YSO detector is estimated using LISE++. The inputs to LISE++ include slit setting, thickness of the degraders and beam detectors in the beam path, Bρ values of the magnets, and every material encountered by the beam on its way to the F11 focal plane. The program provides the energy-loss distribution of the ions stopped in the YSO crystal. The energy-loss spectrum provides an estimate of the end-point energy, *i.e.*, maximum energy carried by ions in the distribution. Figure 4.5, as an example, shows the energy-loss spectrum of ^{82}Zn stopped in the YSO as calculated using LISE++.

The quenched energy-loss distribution produced by the YSO detector was established using the energy calibration procedure of β particles in the low-gain branch. These beta induced signals are recorded at low QDC part in the low-gain branch. The presence of the electrons at the low-QDC allows the verification of the calibration of the ions. The calibration provides us with the energy of the ions in units of electron equivalents. The procedure for the calibration is not straightforward, the steps taken for calibration are listed as follows:

1. Calibration of the high-gain energy branch using ^{137}Cs source

2. Calibration of the low-gain branch using correlation with calibrated high-gain branch

The energy spectrum from the YSO detector is limited in resolution to accurately identify the photo peak from a standard source [62]. To calibrate the high-gain (β) spectrum of YSO, the energy-loss correlation of γ-rays shared between calibrated (High-purity Germanium) HPGe and the YSO was used. For the measurement, a ^{137}Cs source was placed at the center of the YSO. The γ-rays (E_γ = 661 keV) emitted by the source, share energy between HPGe and the YSO. The process is explained by the following equations:

$$E_{\gamma,clover} + E_{\gamma,YSO} = 661keV \tag{4.15}$$

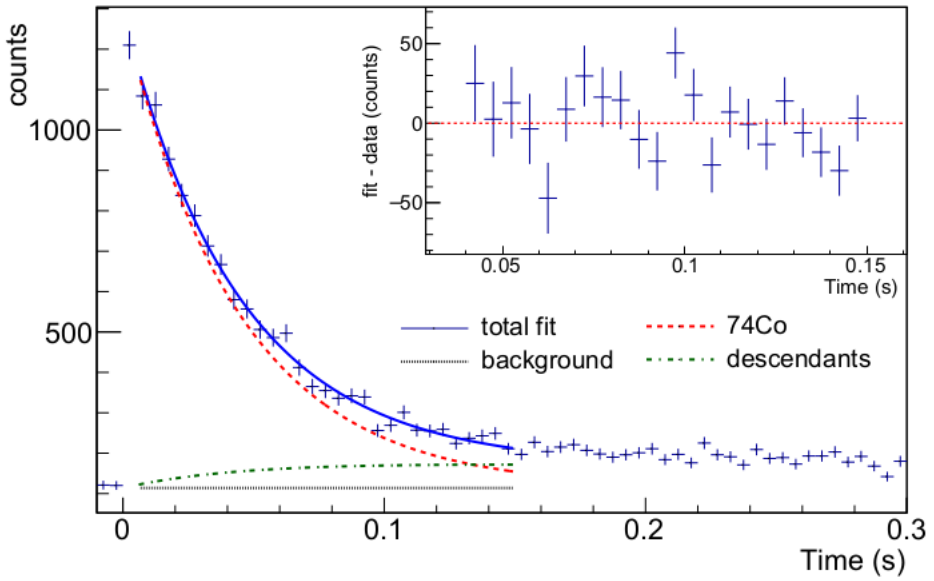


Figure 4.4: Decay curve of ^{74}Co fitted using Bateman Equations [60].

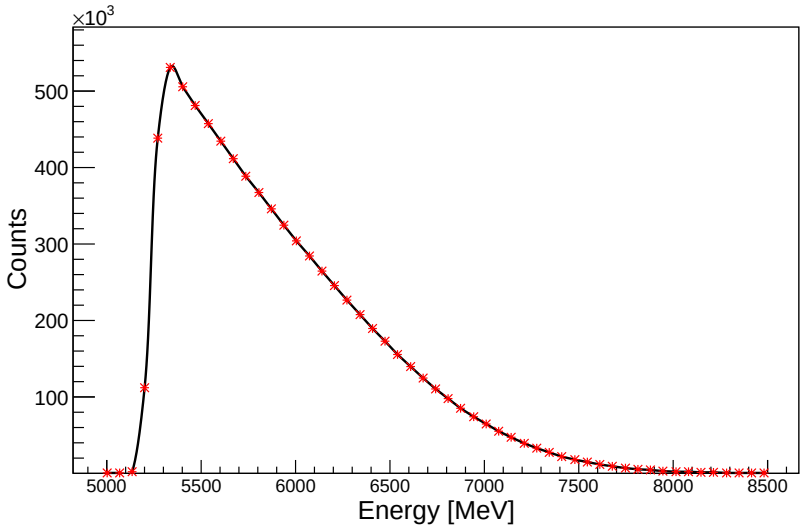


Figure 4.5: Energy-loss distribution of ^{82}Zn ions in the YSO, estimated using LISE++. The end-point energy is estimated to be $\sim$ 8 GeV from the distribution.

where,

$$E_{\gamma,YSO} = a * E_{channel,YSO} + b, \tag{4.16}$$

and $E_{\gamma,clover}$ and $E_{\gamma,YSO}$ denote the energy deposited by a 661-keV γ-ray in HPGe and YSO, respectively. Figure 4.6 shows the correlations between YSO and HPGe detectors. In Equation 4.16, $E_{channel,YSO}$ is the energy deposited by γ ray in arbitrary units, while a and b are the calibration parameters, assuming a linear calibration function. The energy spectrum of the low-gain (ions) branch was calibrated using the correlation between the low-gain and high-gain branches. Figure 4.7 shows the correlation between the two branches after calibration. The low-qdc part of the correlation is due to the signals from beta particles simultaneously recorded in both the branches with different gain settings.

Figure 4.8 shows the calibrated energy-loss distribution of ^{82}Zn in the YSO and shows the end-point energy. Similar distributions were obtained for all the ions fully stopped in the YSO. This gives an estimate of the end-point energy of the histograms in the YSO. An estimate of the quenching factor for each of the isotopes stopped in YSO can be obtained using the following relationship:

$$\text{Quenching Factor (QF)} = \frac{\text{End-point energy from Lise in MeV}}{\text{End-point energy from the data in MeV}}. \tag{4.17}$$

Figure 4.9 has the quenching factors determined using the procedure for various ions stopped in the YSO crystal. Error in the estimate of quenching is due to an uncertainty ($\sim$10 %) in the calibration factor for ions and the error in the estimation of energy from LISE++. The knowledge of light quenching is important for designing experiments with YSO. The estimates of the quenching are important to adjust the dynamic range for ions with different Z in the software. For Z>>28, the light quenching is expected to be more severe and the dynamic range of the ions would be shorter compared to the ones in the vicinity of ^{78}Ni. Whereas, the quenching is expected to be smaller for a region of isotopes with Z<<28, requiring a broader dynamic range if ions of similar energy distribution as in ^{78}Ni impinge into YSO.

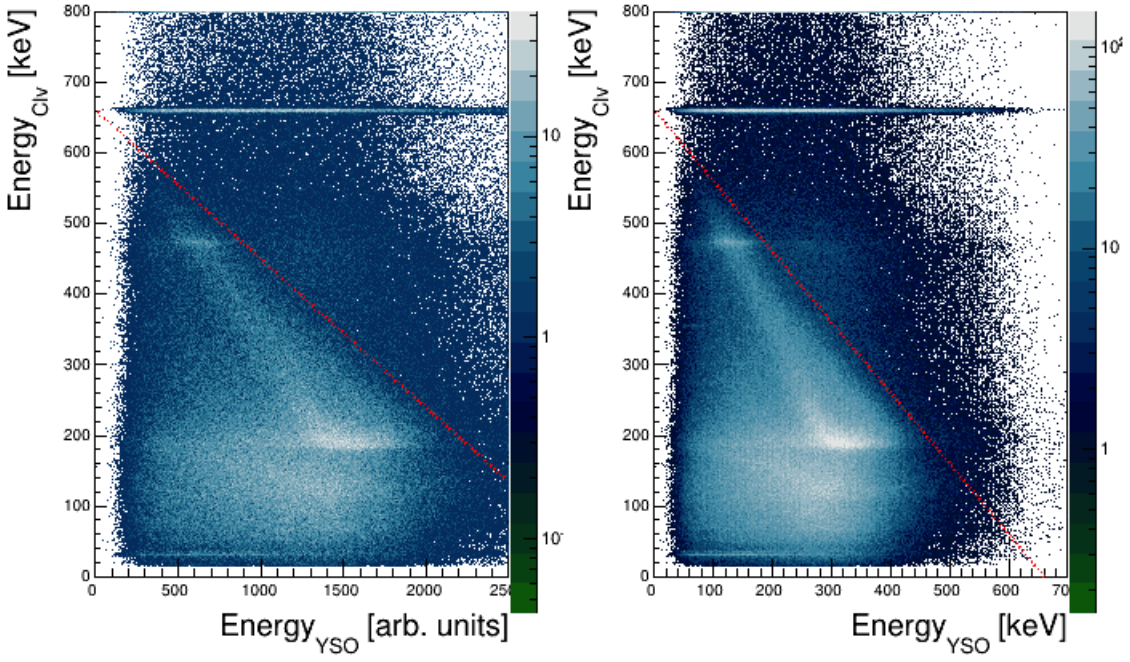


Figure 4.6: a) Correlation between Clovers ($E_{\gamma,clover}$) and the YSO ($E_{channel,YSO}$) high-gain branch. The slope of the correlation provides the calibration parameters. b) Correlation between Clovers ($E_{\gamma,clover}$) and the calibrated YSO ($E_{\gamma,YSO}$) high-gain branch. The red line running through the correlation has a slope of 1, showing the quality of the calibration.

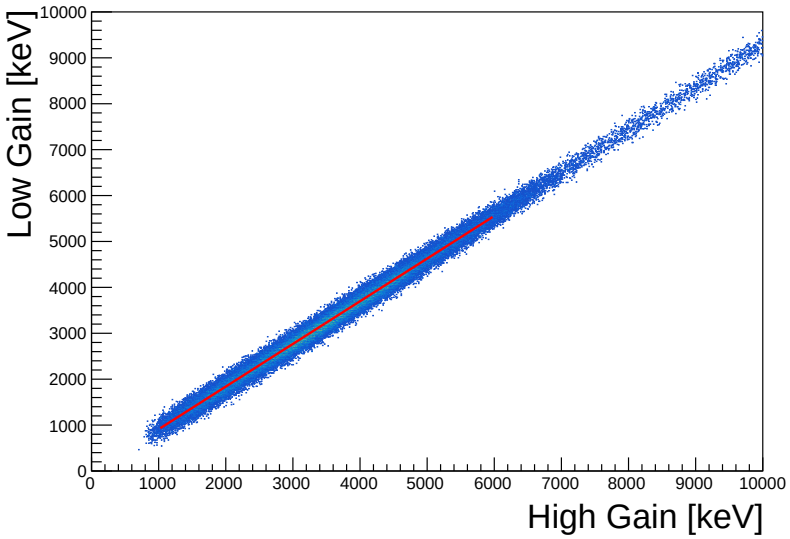


Figure 4.7: Correlation between calibrated high- and low-gain branches. The slope of the correlation after calibrating the low-gain branch with respect to the high-gain branch is equal to one.

4.2 VANDLE Experiment

4.2.1 Particle Identification

As described in the experiment section, particle identification is performed by the BigRIPS particle separator using the TOF-Bρ-ΔE method. The values of Z and A/Q are deduced using the measured values of TOF, Bρ, and ΔE together with the following equations:

The time of flight of a particle for a flight path L:

$$TOF = \frac{L}{\beta c}. \tag{4.18}$$

Equating Lorentz and centripetal forces experienced by a particle in magnetic field B:

$$\frac{A}{Q} = \frac{B\rho}{\beta\gamma}\frac{c}{m_u}. \tag{4.19}$$

The Bethe-Bloch formula describing energy-loss (ΔE) of a particle a material:

$$\frac{dE}{dx} = \frac{4\pi e^4 Z^2}{m_e \nu^2} N z \left[ln\frac{2m_e\nu^2}{I} - ln(1-\beta^2) - \beta^2 \right], \tag{4.20}$$

Here $\beta = \nu/c$, $\gamma = 1/\sqrt{1-\beta^2})$ is the velocity of the particle, $m_u = 931.4$ MeV is the atomic mass unit, m_e is the electron mass, and e is the electron charge. z, N, and I represent the atomic number, atomic density, and mean excitation of the material, respectively. Z, A, and Q denote the proton number, atomic mass, and charge states of a fragment, respectively.

The flight path (L) of ions from F3 to F7 is measured by thin plastic scintillators located at F3 and F7. The foci at F3 and F7 are fully achromatic, while the ones at F1 and F5 are momentum dispersive. ΔE is measured by using the multi-sampling ionization chamber (MUSIC) located at F7. The $B\rho$ measurement is done using the trajectory reconstruction from F3-F5 and from F5-F7. The trajectory of the particles is tracked with the help of a position-sensitive parallel plate avalanche counters (PPAC) located at F3, F5, and F7 [58].

The PPAC detectors and the energy degrader at F5 lead to energy loss. Hence, $B\rho$ measurements are done for the F3-F5 path and F5-F7 path. This leads to a change in Equations 4.18 and 4.19 as follows:

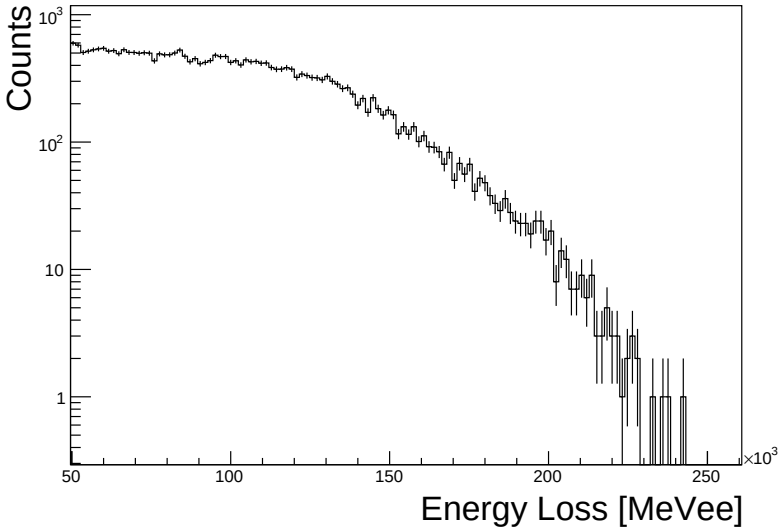


Figure 4.8: Energy-loss distribution of ^{82}Zn in the YSO with an estimated end-point energy of $\sim$ 240 MeVee.

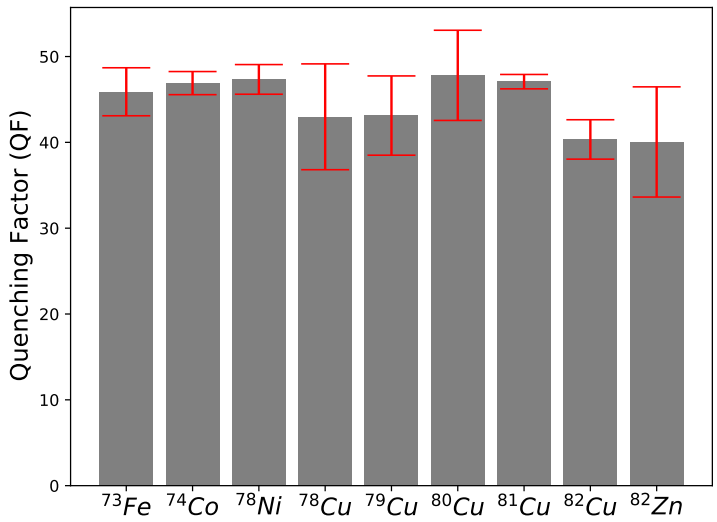


Figure 4.9: Light quenching factors obtained for various isotopes stopped in YSO.

$$TOF = \frac{L_{35}}{\beta_{35}c} + \frac{L_{57}}{\beta_{57}c}, \tag{4.21}$$

$$\left(\frac{A}{Q}\right)_{35} = \frac{B\rho_{35}}{\beta_{35}\gamma_{35}}\frac{c}{m_u}, \tag{4.22}$$

$$\left(\frac{A}{Q}\right)_{57} = \frac{B\rho_{57}}{\beta_{57}\gamma_{57}}\frac{c}{m_u}. \tag{4.23}$$

If the charge state of the ion does not change on its course from F3 to F7 at F5 then, we will have the following relation by equating 4.22 and 4.23:

$$\frac{B\rho_{35}}{B\rho_{57}} = \frac{\beta_{35}\gamma_{35}}{\beta_{57}\gamma_{57}}. \tag{4.24}$$

The velocities of the fragments before (β_{35}) and after (β_{57}) F5 can be deduced using equations 4.21 and 4.24 from the measured TOF and $B\rho_{35,57}$ values. The absolute value of Z can be deduced by modifying equation 4.20 as follows:

$$Z = a \times \beta_{57} \times \sqrt{\frac{\Delta E}{ln\left(\frac{2m_e c^2\beta^2}{I}\right) - ln(1-\beta_{57}^2) - \beta_{57}^2}} + b. \tag{4.25}$$

ΔE and β_{57} are the inputs to Equation 4.25, a and b are the parameters determined empirically during the experiment.

In the following sections, cuts and gates implemented in the data for building cleaner events tagged with calibrated Z and A/Q are shown.

F3 and F7

Plastic scintillator detectors located at F3 and F7 for measuring ToF are read out using the photomultiplier tubes (PMT), which are coupled to the left and right ends of the detector. The position of an incident particle can be found using the charge-integrated signals q_1 and q_2 from the left and right ends of the detector using the following expression:

$$x = -\frac{\lambda}{2} ln\left(\frac{q_1}{q_2}\right). \tag{4.26}$$

Here λ denotes the attenuation length of scintillation light in the detector. We can also get the position from the timing of the left and right PMT signals as

$$x = -\frac{V}{2}(t_2 - t_1). \tag{4.27}$$

By equating Eqs 4.26 and 4.27 we obtain the basis for rejecting signals in the data lying far off from the constraint defined by the following equation:

$$-\frac{\lambda}{2} ln\left(\frac{q_1}{q2}\right) = \frac{V}{2}(t_2 - t_1), \tag{4.28}$$

where V denotes the speed of propagation of light in the scintillation counter. Figure 4.10 shows the correlation derived from the time difference and the ratio of the left and right PMT signal amplitudes from the data for the F7 plastic scintillation detector.

PPAC

Position-sensitive Parallel Plate Avalance Counters (PPAC) are used for tracking the fragments in the beamline at RIBF [63]. The detectors consist of electrode films separated by 3-4 mm with four readouts ($T_{X_{(1,2)}}$ and $T_{Y_{(1,2)}}$) for each plate used for position tracking. The detectors adopt a delay-line readout method. The position of an incident particle is determined from the time difference between two timing signals T_1 and T_2 obtained from the ends of the delay line in the PPAC detector. The sum of the timing is defined as

$$T_{sum} = T_1 + T_2, \tag{4.29}$$

which remains constant independent of the position of the incident particle, and acts as an important tool to remove inconsistent events and effects of δ-rays from the data. As an example, Figure 4.11 shows the T_{sum} distribution for X position signals of one of the plates of PPAC located at F3. Similar cuts were used for all the PPAC detector plates in the BigRIPS separator.

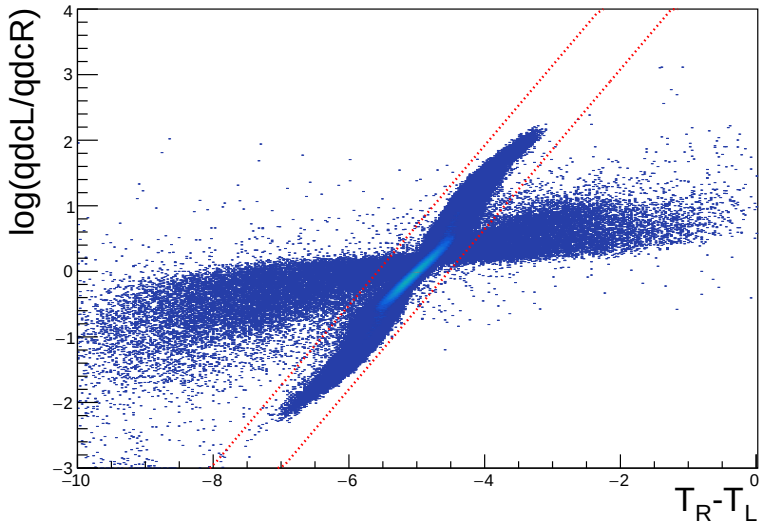


Figure 4.10: Implementation of a "cut" in the data from the F7 plastic to reject background events.

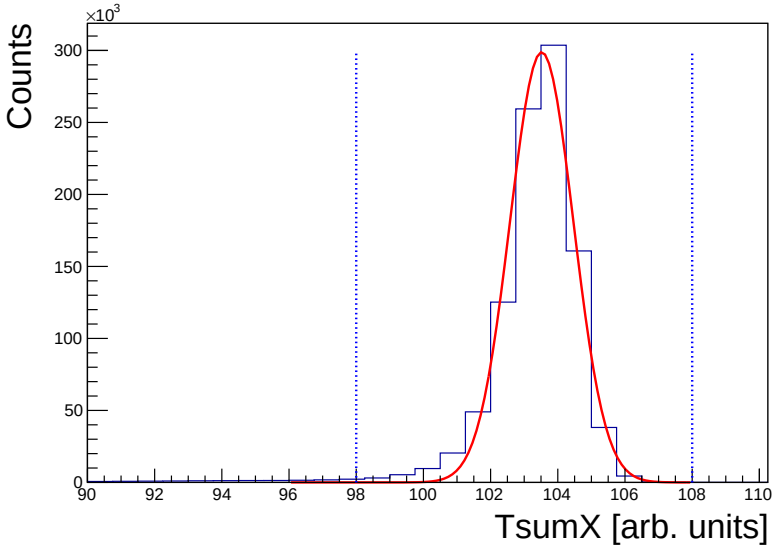


Figure 4.11: T_{sum} for the sum of one of the plates of PPAC at F3. Only events lying within the FWHM range of the main peak are accepted.

MUSIC (ΔE) Detector

The MUlti-Sampling Ionization Chamber (MUSIC) detector is used for the ΔE measurement in the BigRIPS separator and it consists of alternating twelve anodes and thirteen cathodes [64]. The neighboring anodes are electrically connected in pairs. The six anode signals are read independently and averaged for the ΔE measurement. The fragments on their way through the MUSIC detector can cause nuclear reactions with the electrodes and the counter gas leading to a change in their charge state. The correlation between alternative anodes helps to remove inconsistent events from the beam. As an example, Figure 4.12 shows the ratio of signals from two consecutive anodes. The signals were accepted within the FHWM of the peak of the distribution. Similar gates were implemented for all the consecutive anode signals. Further, fragments upon leaving the F7 plastic scintillator detector can experience a change in the charge state due to reactions in the F7 detector. These events were rejected using the correlation between the signal from the MUSIC detector and the signals from the left and right of the F7 detector as shown in Figure 4.13.

Upon the implementation of all the cuts, a linear function for calibration of Z was used, and Figure 4.14 shows the calibrated Particle Identification (PID) plot at the F7 focal plane, showing all the isotopes in the beam.

4.3 YSO

To obtain ion-beta correlation for the YSO detector, a similar approach developed for the YSO detector for the BRIKEN experiment was implemented. However, the images reconstructed from the data from the VANDLE experiment showed distortions due to the light guide and slight saturation in the signals. As a result of the distortions, there is a non-uniformity in pixel-to-pixel distance between the ion and the beta image. Figure 4.15 shows the position distribution of beta and ion images that were reconstructed using the anger logic. The images clearly show the distortions, the distortions are more severe in the ion position distribution. Figure 4.16 shows the distribution of the distance of pixels identified in the ion and beta images. The curve in the plot mimics the distortions in the images.

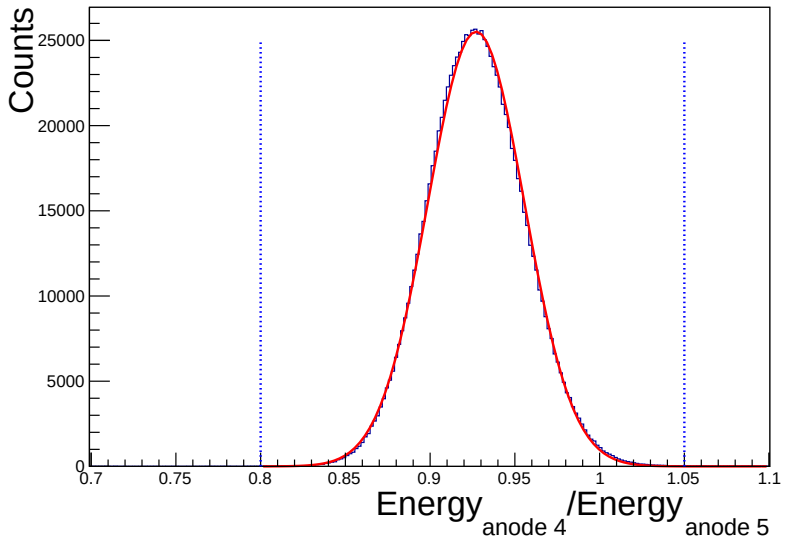


Figure 4.12: Ratio of 5th and 4th anode signal for the MUSIC detector.

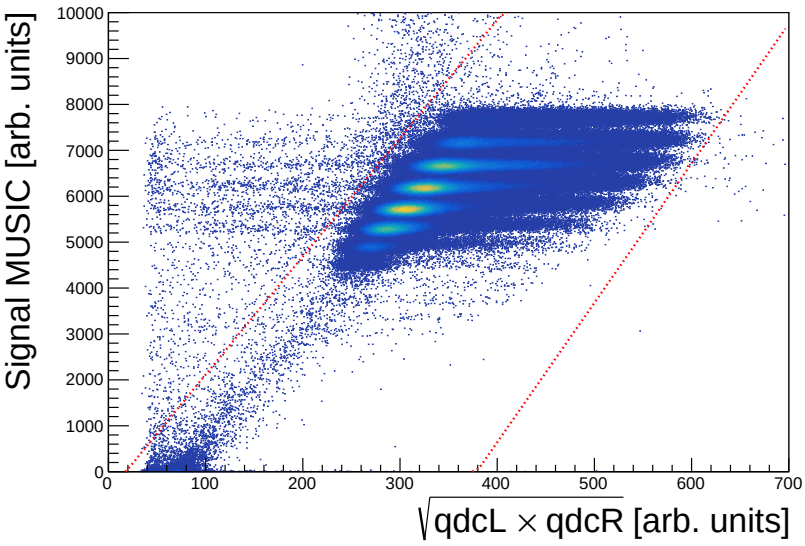


Figure 4.13: Cuts implemented on the data obtained from the MUSIC detector.

The irregularities in the pixel-to-pixel distance can lead to the accumulation of random background. The irregularities also can give misleading estimates of the beta efficiency with the change in correlation radius, as a given correlation radius will have fewer pixels in the center of the detector where pixel density is sparse compared to the corners where the pixel density is higher. To address these issues, images were transformed to a discrete space. This was achieved by using the nearest-neighbor pixel search approach. A template position map was created containing pixel ID (row, column) and position coordinates of the pixel in the beta and ion images. The algorithm looked for the nearest pixel ID from the map using the distance minimization approach or nearest neighbor approximation and assigned a pixel ID to each ion and beta event on an event-by-event basis. After the transformation, the position gates for correlation were set in terms of the pixel numbers.

The transformation from the position space to the pixel space can be written as follows:

$$(X_\beta, Y_\beta) \xrightarrow{NNA} (I_{\beta,i}, I_{\beta,j}) \tag{4.30}$$

and

$$(X_{ion}, Y_{ion}) \xrightarrow{NNA} (I_{ion,i}, I_{ion,j}). \tag{4.31}$$

Here, $I_{ion,\beta,i}, I_{ion,\beta,j}$ denote the indices of the pixel associated to a given position of an ion/beta event. The correlation criterion after the transformation changes from position space to pixel space as follows:

$$\sqrt{(I_{\beta,i} - I_{ion,k})^2 + (I_{\beta,j} - I_{ion,l})^2} < n. \tag{4.32}$$

Where n is the correlation radius in terms of number of the pixels around a beta or ion event. A schematic of the algorithm for the correlation in the pixel space is shown in Figure 4.18, and Figure 4.17 shows the transformed images gated on the activity of ^{74}Co. Figures 4.19 and 4.20 show the fitting of decay curves of ^{74}Co and ^{79}Cu, respectively, obtained using correlations in pixel space using the Bateman Equations.

Beta-detection Efficiency

The beta-detection efficiency of the detector is defined as:

$$E_\beta = \frac{N_{\beta,\text{parent}}}{N_{\text{imp}}}. \tag{4.33}$$

Here $N_{\beta,\text{parent}}$ is the number of β decays of the parent nucleus calculated within a certain time window ($\text{T} = T_\beta - T_{ion}$) and is defined as follows:

$$N_{\beta,\text{parent}} = \frac{A_0 \times \text{A}}{A_0 + A_1 P_{\beta 1} + (1 - P_{\beta 1}) A_2}, \tag{4.34}$$

where A_0 denotes the activity of the parent nucleus, A_1 is the activity of the daughter nucleus in the β-decay branch, A_2 denotes the activity of daughter nucleus in the βn channel, and A is the area under the decay curve, all calculated in time T.

N_{imp} is the number of implants or decays of the parent nucleus in YSO in time T. The portion of the activity of the parent nucleus in a certain time (T) is calculated using the activity of the parent nucleus as follows:

$$N_{\text{imp}} = N_o \times \frac{\int_0^T \exp(-\lambda t) dt}{\int_0^\infty \exp(-\lambda t) dt}, \tag{4.35}$$

Here N_o is the total number of implantations of the parent nucleus in the YSO detector. Beta-efficiency is calculated for ^{79}Cu implants by varying the correlation radius in terms of the number of pixels. Figure 4.21 shows the variation of the beta-detection efficiency of the YSO detector with changing correlation radius. A maximum of $\sim$ 80 % beta-detection efficiency is achieved with a 3-pixel correlation radius.

4.4 High-resolution Germanium Detectors

A clover detector contains 4 HPGe crystals sensitive to γ-rays. The main analysis for clover detectors consisted of calibration and efficiency calculations. The crystals of the detector need to be calibrated individually followed by proper gain-matching. For efficiency and calibration, data were collected using standard sources in the experiment configuration.

Standard sources, such as ^{133}Ba, ^{60}Co, ^{137}Cs, and ^{152}Eu were used for efficiency and calibration measurements. The analysis is performed in singles mode, where the spectrum from each crystal is analyzed independently. Some of the crystals of the clovers suffered from gain shift during the experiment. Thus, calibration parameters from the source run could not be implemented for the experiment runs. However, a number of known background lines were identified in the in-beam runs and they were used for calibration. The γ-ray lines identified in the background and used for the calibration and their sources are listed in Table 4.1.

A polynomial of the first order as shown in Equation 4.36 was used to calibrate the clover spectrum to keV.

$$E_\gamma = a \times E_{ch} + b \tag{4.36}$$

Here, a and b represent the calibration parameters. A calibrated spectrum gated on the decay of ^{84}Ga with annotated lines is shown in Figure 4.22.

The determination of the efficiency of the detector is rather complicated due to the presence of the YSO crystal. The YSO detector is sensitive to γ-rays and acts as a γ-ray absorbing material. The absorption can lead to a reduction in γ-ray efficiency of the Clovers for low-energy γ-rays. Another factor affecting the efficiency is the finite size of the YSO detector, which means that different γ-rays originating from different positions in the YSO will subtend different solid angles on clovers. To properly account for the absorption effects from the YSO and for the sake of accuracy, efficiency was measured by placing a standard source at different positions on the face of the YSO detector. Figure 4.23 shows the layout of the source holder. This source holder was affixed onto the face of the YSO detector to quantify the change in the efficiency with a change in the position of a gamma source around the implantation point.

From the efficiency measurements using the standard sources, it was determined that the data from ^{152}Eu was subjected to significant dead time due to high source activity. The dead time then leads to an underestimation of the efficiency. The dead time was calculated using the count rate for the 1435.7-keV line from ^{138}La, and $LaBr_3$ detectors are the source of the line. The ratio of the count rates from the background and the source data gives

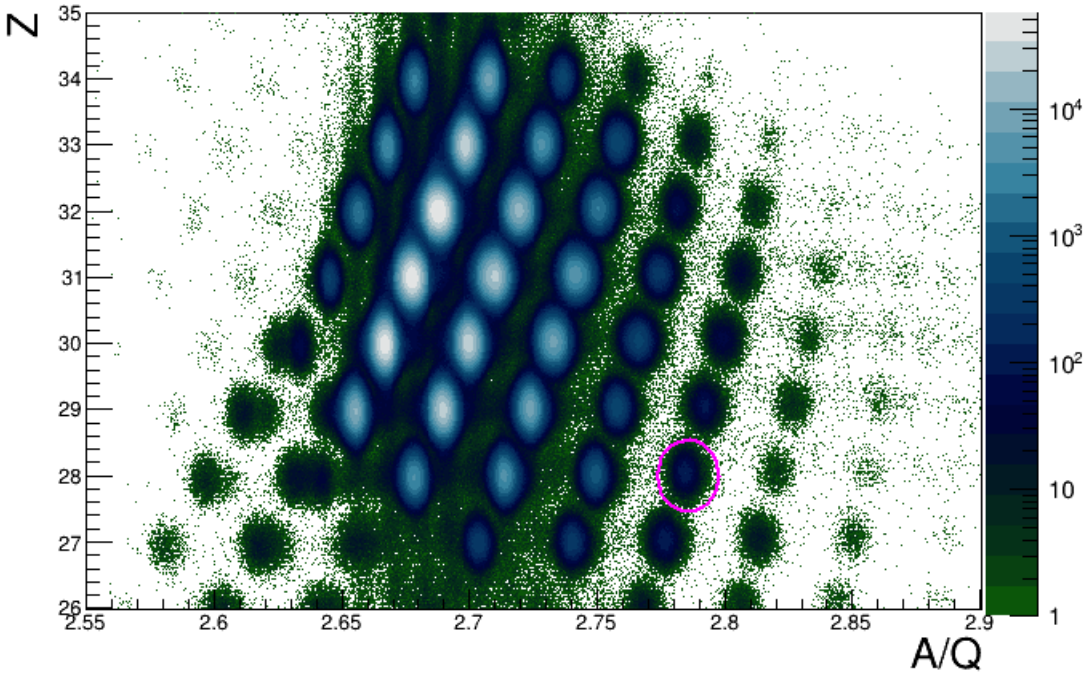


Figure 4.14: Calibrated and cleaned Particle Identification (PID) at the F7 focal plane showing ^{78}Ni in a pink ellipse.

Table 4.1: Sources used for calibrating HPGe detectors

γ-ray (keV)	Source
351.9	^{214}Pb(Ra)
511	Pair production
788.7	^{138}La
1435.7	^{138}La
1460.8	^{40}K
1764.5	^{214}Bi(Ra)
2614.7	^{208}Tl(Th)

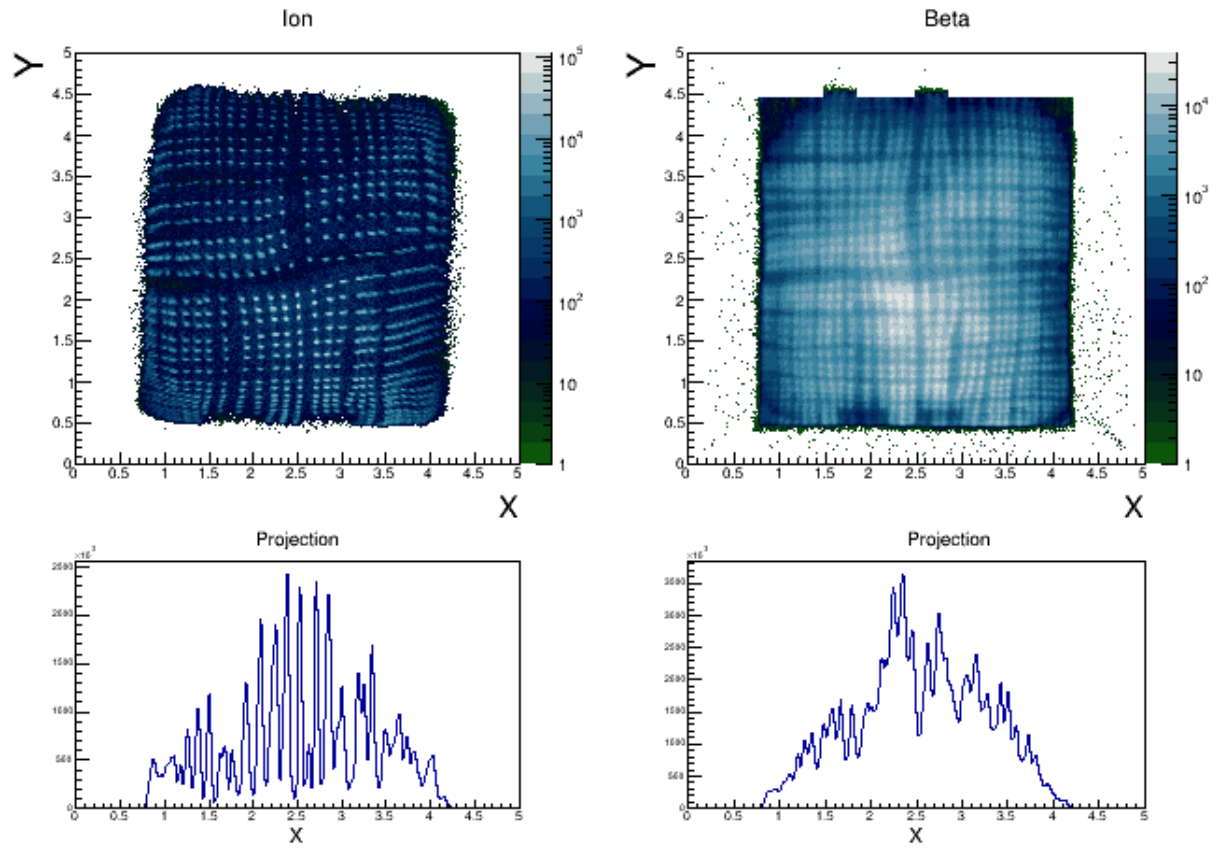


Figure 4.15: Images of ion and beta position distribution, gated on the activity of ^{84}Ga obtained using the anger logic.

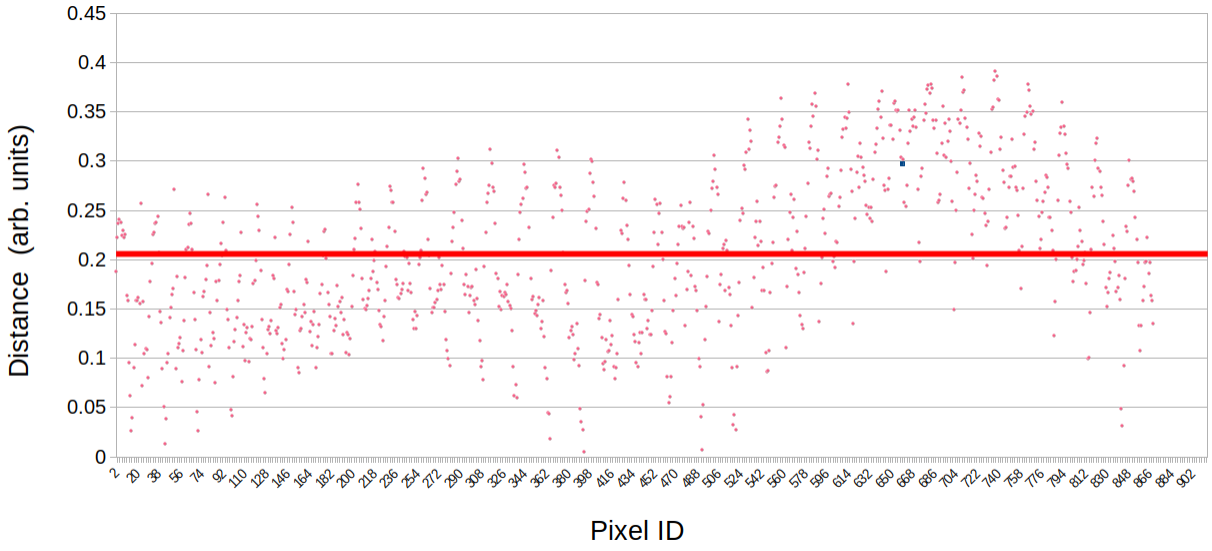


Figure 4.16: Distance between the pixels of ion and beta images. The irregularities in the distance are due to the distortions in the ion image. The solid pink line denotes the average distance of all the pixels.

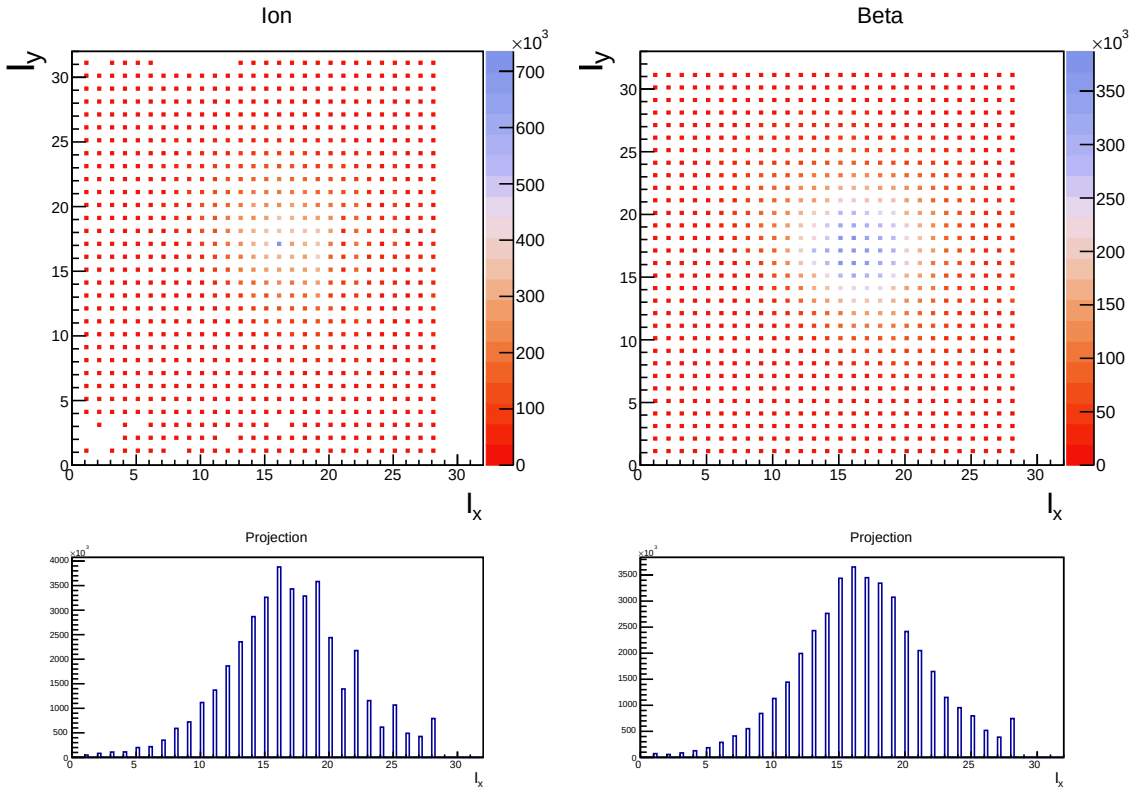


Figure 4.17: Transformed images to pixel space.

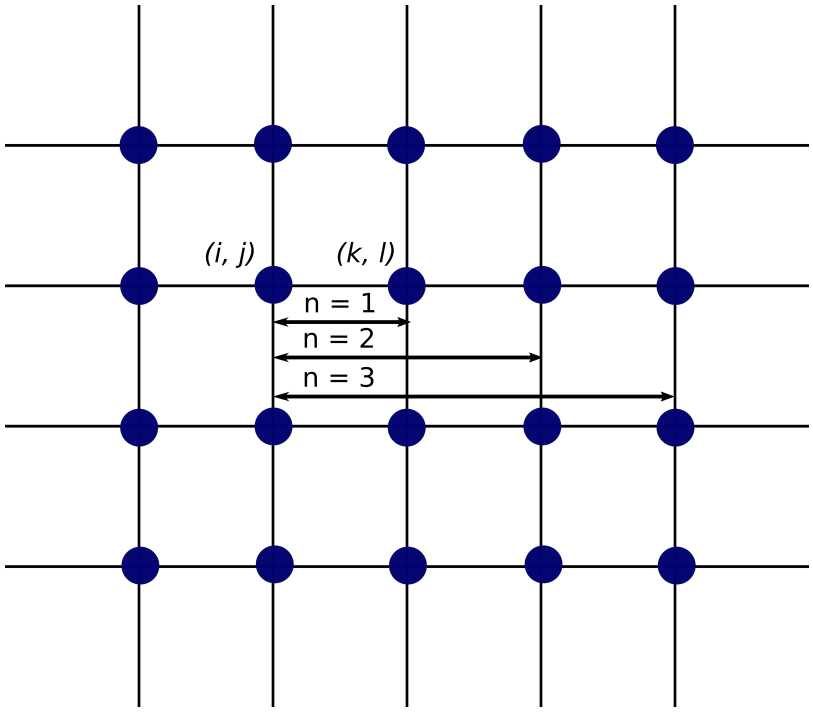


Figure 4.18: A schematic of the algorithm adopted to achieve ion-beta correlations using transformed images in pixel space.

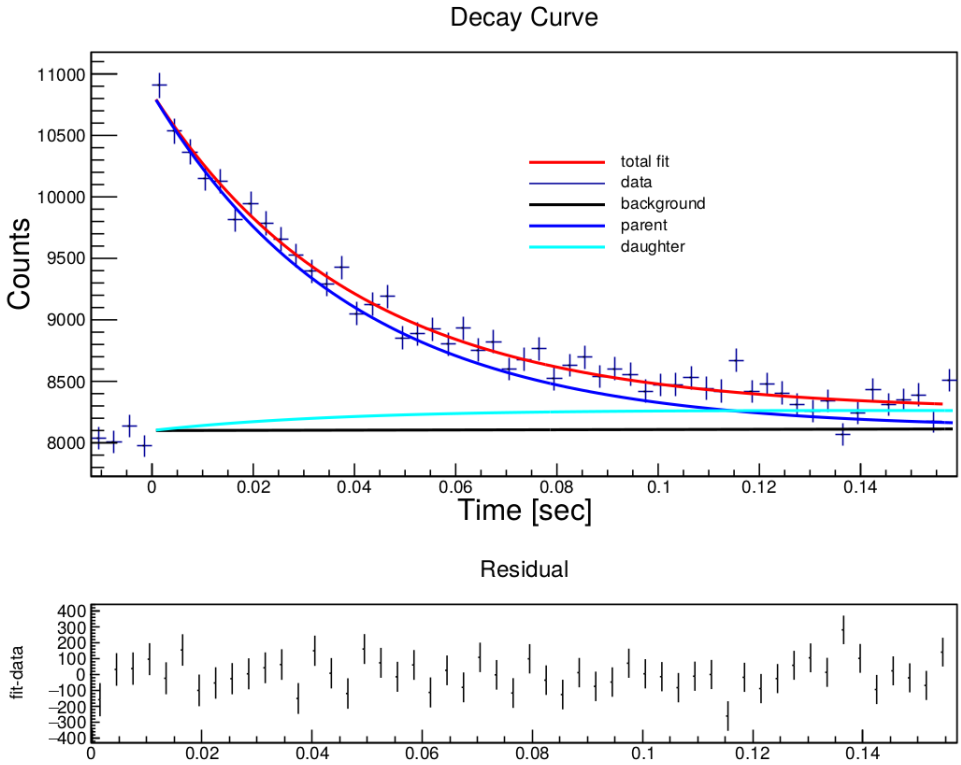


Figure 4.19: Decay curve of ^{74}Co obtained using the transformed images. The half-life of ^{74}Co was calculated to be 27.46 ± 2.30 ms. The top panel shows the fit of the decay curve using the Bateman Equations with various components and the bottom panel shows the residual between the data and fit.

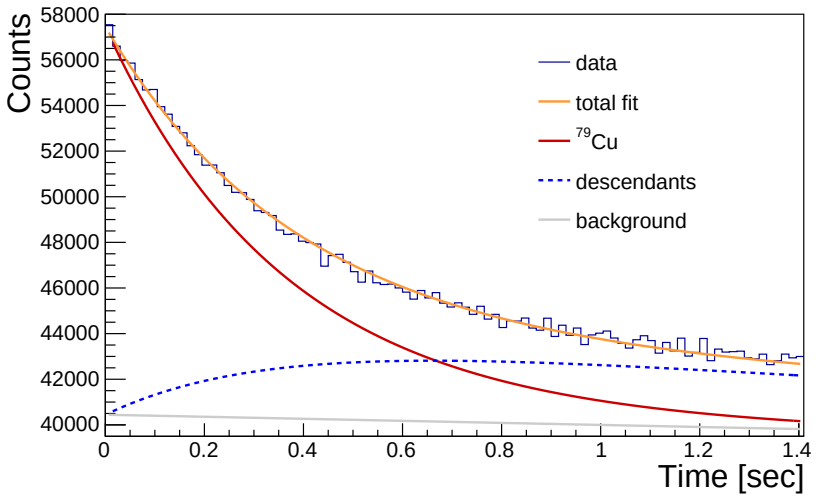


Figure 4.20: Decay curve of ^{79}Cu fitted using the Bateman Equations using the transformed images.

the correction factor needed for the efficiency calculated using the ^{152}Eu source. Figure 4.24 shows the dead time for all the source runs. Data from the ^{152}Eu experiences the largest dead time. The same count rate was calculated for the beam runs, and it showed no dead time.

The data collected for the efficiency measurements were later used to benchmark a GEANT4 simulation package. The benchmark here is to get reliable efficiency measurements from the GEANT4 simulations when a source is placed at any position on the face of the YSO detector. The criterion adopted for the benchmark was to have efficiency from the simulations within the error bars for measurements at each of the positions or there is a discrepancy of less than $\sim$ 5-8 % between the data and the simulations. The measurement of the efficiency with sources placed at different positions on the face of the YSO detector and the results from the simulations are shown in Figure 4.25.

After benchmarking the simulation using the data, a γ-ray source designed using the implantation profile was placed at the center of the YSO in the simulation. γ-rays were emitted randomly from the implant position. The validity of the method was verified by calculating the gamma intensity of lines from previous measurements. For example, 624.2 keV is known to be the strongest transition in the decay of ^{85}Ga with a measured intensity of 40(4)% [65]; comparatively, our measurements showed a value of 44.7(18)%. Using ^{84}Ga data from the experiment relative intensities of some of the intense lines in the decay of β-decay of ^{84}Ga to ^{84}Ge germanium were verified with the measurements reported by K. Kolos *et al.,* 2014 [66]. The measurements from our experiment have larger error bars due to higher uncertainty in the efficiency determination at low-energy γ-rays. The position of the source origin in the YSO detector coupled with absorption in the YSO leads to higher errors for the efficiency of low-energy γ-rays. A comparison of relative intensities of γ transitions in the decay of ^{84}Ga is listed in Table 4.2.

The values measured in this experiment are in consensus within the limits of error bars reported. The simulation was then extended to determine efficiency of the clovers in the add-back mode. In add-back mode, the energy deposited by a γ-ray on its track through the crystals of a clover is summed up and designated as a single event. This leads to an increase in efficiency for the high-energy γ-rays, which are more prone to scattering across

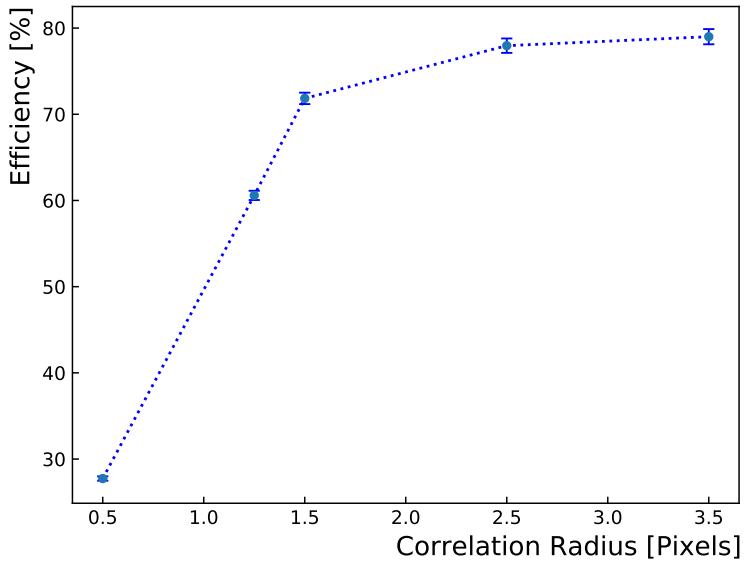


Figure 4.21: Beta-detection efficiency of the YSO detector for ^{79}Cu implants.

Table 4.2: Relative intensity of gamma lines in the decay of ^{84}Ga

Sr.No.	E_γ(keV)	Measured (%)	Reference Value (%)
1	247	100	100
2	624	67(16)	61(3)
3	1046	55(11)	55(3)
4	3502	36(7)	36(5)

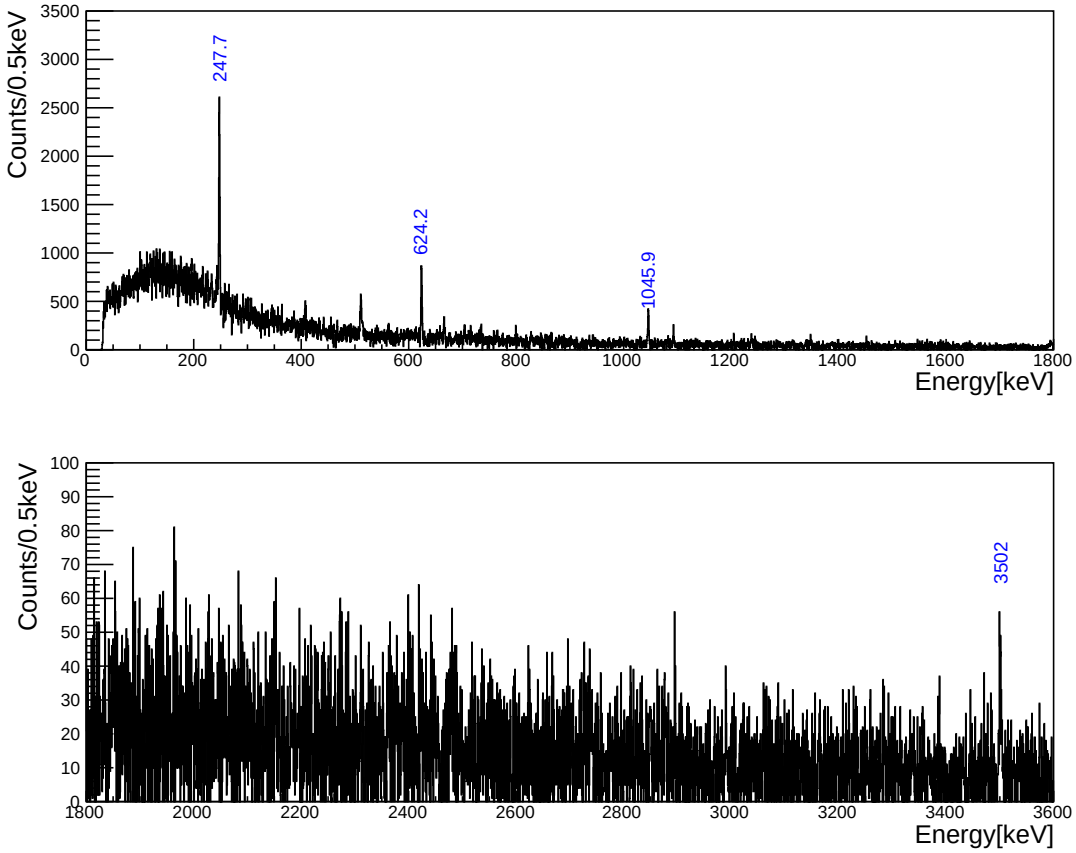


Figure 4.22: Calibrated HPGe spectrum in singles mode, gated on the decay of ^{84}Ga showing some of the intense γ lines.

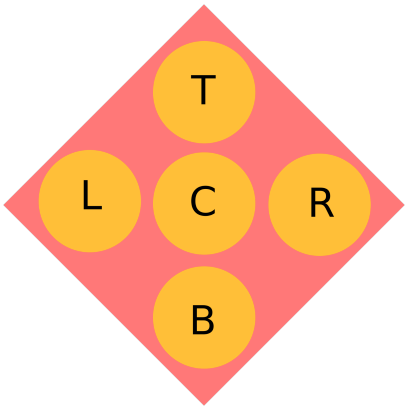


Figure 4.23: Design of a 3D-printed source holder matching the dimensions of the YSO. Yellow circles show cavities for placing a source. The source positions are labeled as the top (T), bottom (B), left (L), right(R), and center (C).

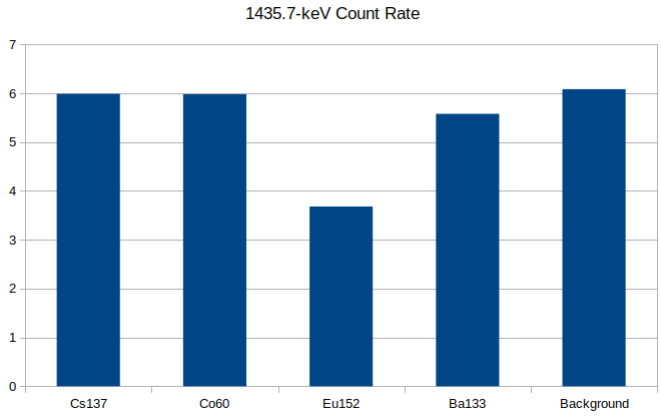


Figure 4.24: Count rate of the background peak during the source measurements.

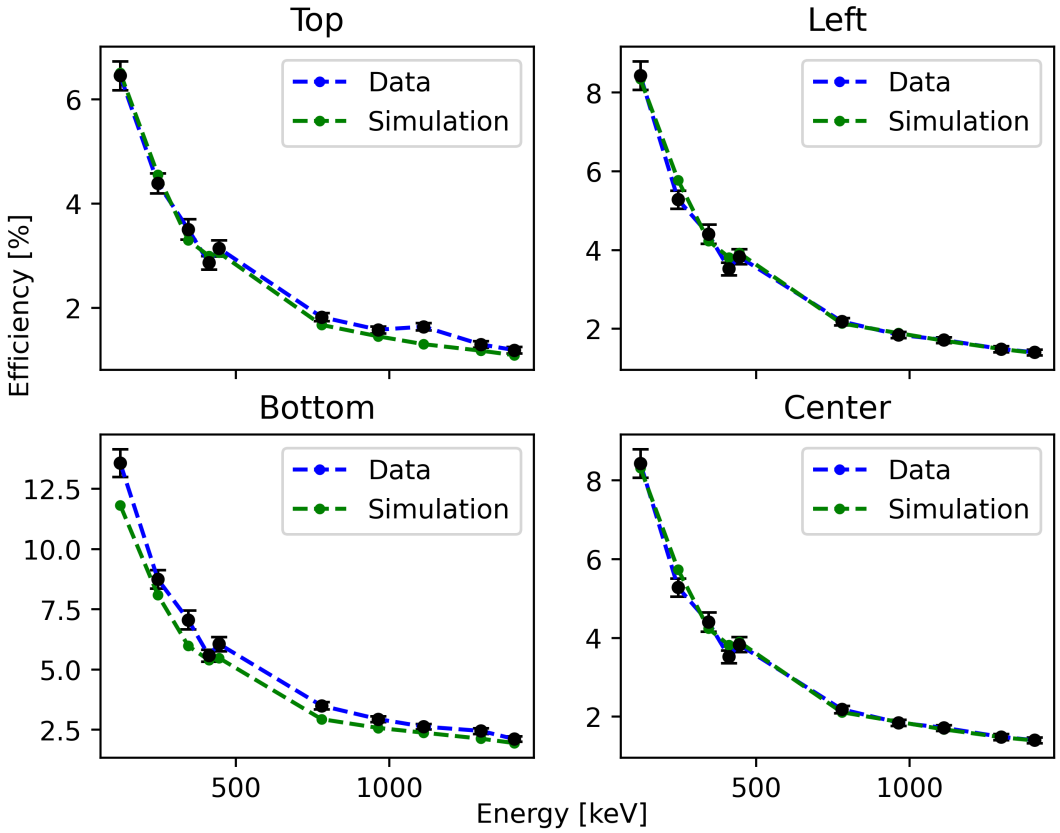


Figure 4.25: Measured and simulated efficiency for all source positions.

the crystals of a detector compared to low-energy γ-rays. Figure 4.26 shows the comparison of the efficiency of HPGe detectors in the singles and add-back mode.

4.5 Lanthanum Bromide ($LaBr_3$)

A procedure similar to the calibration of the HPGe detectors was used for calibrating $LaBr_3$ detectors, where standard sources such as ^{137}Cs and ^{60}Co were used. Figure 4.27 shows the calibrated spectrum from the $LaBr_3$ detectors gated on the decay of ^{83}Ga. The data from the $LaBr_3$ detectors have not been used in this dissertation.

4.6 VANDLE Analysis

This section contains the analysis of the VANDLE array.

4.6.1 Timing

For the Pixie-16 systems, the onboard digital filter, implemented in the FPGA latches and records the digitized waveforms (traces) once a valid trigger is detected. The validity of a trigger for the experiment is decided by a triple-coincidence criterion between the two signals of a VANDLE bar and the YSO. The total length of the trace, which includes the length and the pre-trigger length is set during the time of the experiment. The time of arrival of the trace is provided by a 48-bit timestamp when a valid trigger latches onto the FPGA. The timing obtained this way is limited by the sampling frequency of the onboard digitizer, *i.e.*, 2 ns. In order to determine a sub-nanosecond timing, a quantity called phase (ϕ) is calculated. The phase of a selected signal is given by the offset from the digitized latch time obtained from the FPGA. The final time of arrival of a signal is given by the summation of digitized time and calculated phase. The phase is derived from the trace, which is latched with respect to the FPGA time click. During the experiment, traces were saved for both left- and right-end PMT signals of each of the VANDLE bars. The time of a given event in the digitizer is provided by the summation of the filter clock from the FPGA and the phase,

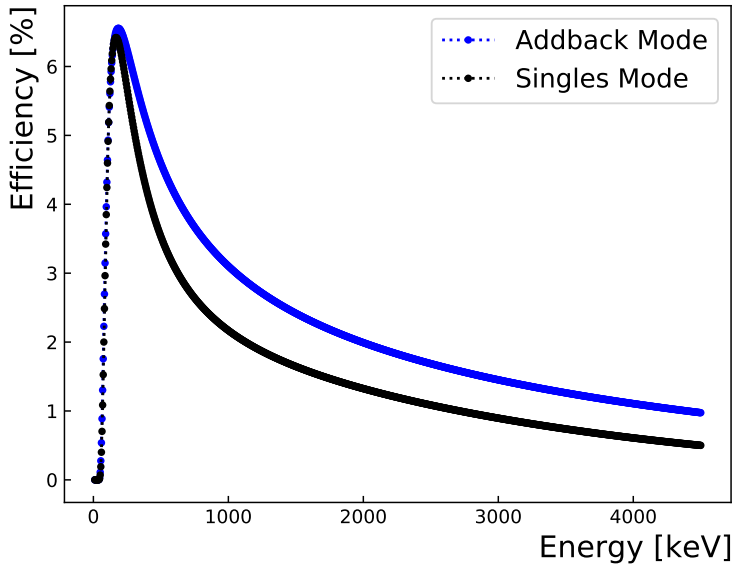


Figure 4.26: Comparison of the add-back and singles efficiency of HPGe detectors.

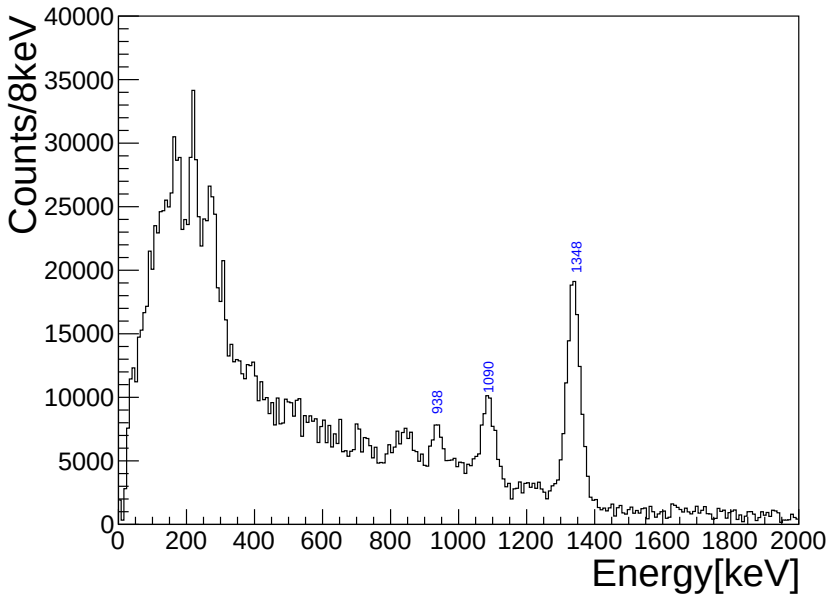


Figure 4.27: Calibrated $LaBr_3$ spectrum gated on ^{83}Ga. The most intense lines are identified and verified in the daughter nucleus ^{83}Ge and ^{82}Ga.

$$time[ns] = t_{FPGA} + \phi. \tag{4.37}$$

The digitized waveform can be approximated using an analytical function as follows:

$$f(t) = \alpha e^{\frac{-(t-\phi)}{\beta}}(1 - e^{\frac{-(t-\phi)^4}{\gamma}}) \tag{4.38}$$

Here, β denotes the exponential decay of the waveform. The leading edge of the wave function is approximated by an inverted-squared Gaussian having width γ, while α denotes the normalization of the function. All of these parameters are determined by fitting the digitized waveforms using the in-built GSL library in ROOT. For optimization, a sample of 16,000 waveforms was fitted with the waveform function as mentioned in S.V. Paulaskas *et al.*, 2015 [67]. All the parameters were set as free variables, giving a distribution of β and γ. Average values of β and γ were obtained which represent the shape of the response of waveforms generated by the PMTs of the VANDLE bars. These values (γ = 0.1734266 ns, β = 0.125515810 ns^4) are given as initial parameters at the time of fitting of the digitized waveform, and the phase (ϕ) obtained from the fit of each waveform is used for sub-nanosecond timing calculation.

4.6.2 Time Calibration

The arrangement of the bars around the YSO in a 105-cm radius is subject to minor fluctuations due to errors in measuring/placing the distance and mechanical handling of the frame. A small change in the distance of each bar is reflected in terms of the position of the gamma flash for each bar. The misalignment caused by the presence of z-offset for each bar affects the resolution of the neutron peaks and for severe misalignment, can also make the discrimination between two neighboring neutron peaks difficult. Therefore, it is important to align each bar in their time response for a similar measurement. The time difference (T_{diff}) between the left and the right signals of a VANDLE bar should have a Gaussian-like distribution centered at zero for a measurement with a source placed at the center of the bar, because of the left-right symmetry. To time-align the bars, measurements with a standard source placed at the center of each of the bars were taken. The T_{diff} distribution for each

distribution was fitted with a Gaussian function. The offset for each bar is measured and is applied to the data. Figure 4.28 shows the difference between left-right and their variation with bar number after adjusting the offset.

Time-Walk Correction

Time measurements in digital systems are subject to a dependence on the amplitude of the pulse. Different pulses with different amplitudes, even with the same trigger time, will register a different time in the software. This effect is shown in Figure 4.29 where three signals with the same start time (t_o) will have a different trigger time recorded in the software as per the threshold (V_T). This dependence of trigger time on the amplitude of the signal is referred to as Time-Walk. This effect is more severe for low-amplitude signals than high-amplitude signals. It is important to correct/compensate the trigger time of low-amplitude signals using a proper characterization for accurate measurements of ToF. Due to a constant speed of light we don't expect a time dependence in the ToF of gamma rays. However, the gamma flash in the ToF spectrum demonstrates the walk effect clearly. The gamma flash shape has a dependence on QDC (charge to digital conversion). Figure 4.30 demonstrates the presence of time walk leading to a curvature in the γ flash shape.

The signals from the PMTs of the VANDLE showed a walk as high as 1 ns over the entire QDC range of the signals. This can adversely affect the energy measurements of the neutrons. To properly characterize the walk behavior of VANDLE left and right PMTs, the timing of signals from the left and right PMTs are plotted with respect to YSO time, shown in Figure 4.31. The walk behavior is fitted with a second-order polynomial and the obtained function is used to correct the timing of signals.

The function obtained from the fit was used to correct walk in timing for all the bars.

$$f_{walk}(qdc) = \begin{cases} 6.79 \times 10^{-8} \times (qdc - 3700)^2, & \text{if } qdc < 3700. \\ 1.15696 \times 10^{-8} \times (qdc - 3700)^2, & \text{otherwise.} \end{cases} \tag{4.39}$$

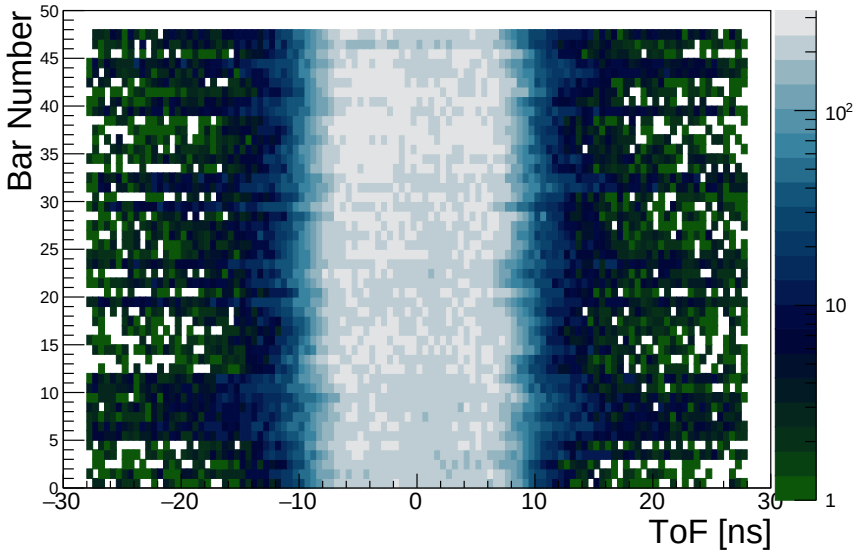


Figure 4.28: T_{diff} distribution for each VANDLE bar after time calibration.

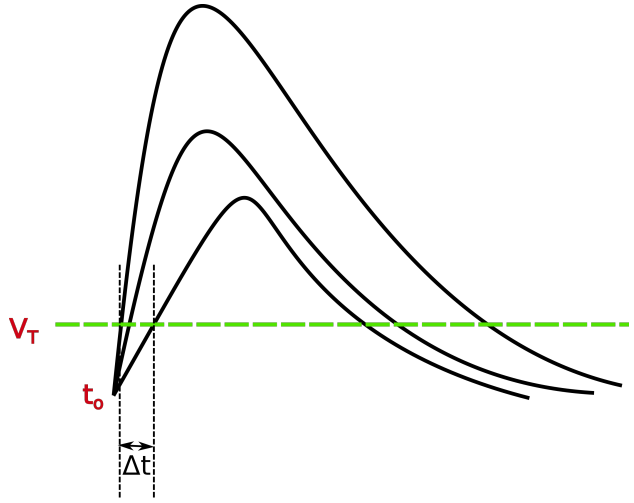


Figure 4.29: A diagram showing the cause of the walk in timing for signals with different amplitudes and dependence on threshold (V_T).

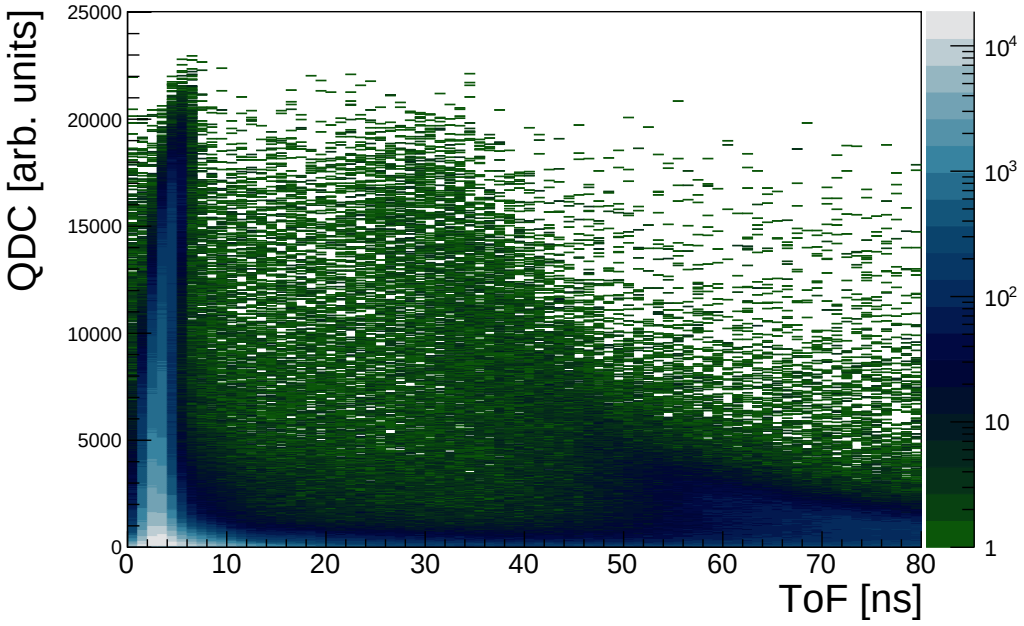


Figure 4.30: Gamma flash in ToF spectrum bent right due to time walk.

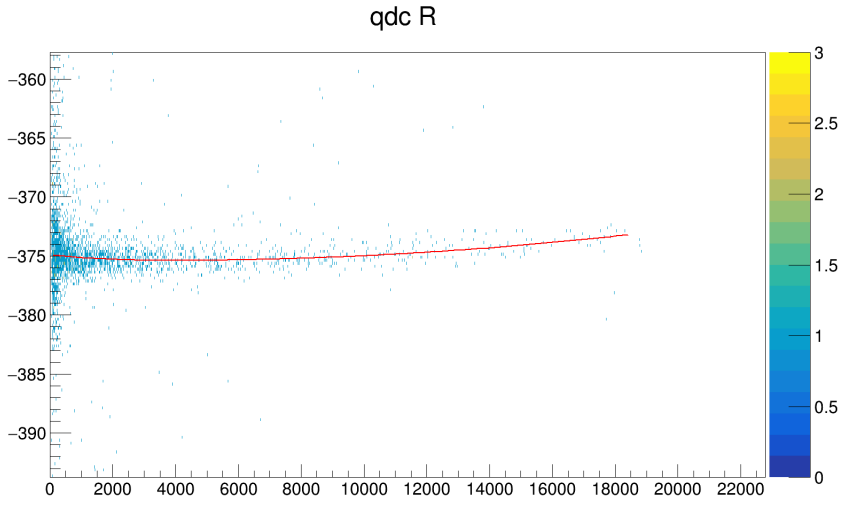


Figure 4.31: Walk characteristic of signals from right PMT of a VANDLE bar fitted with a second-order polynomial.

Correction using the function is applied on an event-by-event basis by the following equation:

$$t_{corrected} = t_{pixie} - f_{walk}(qdc). \tag{4.40}$$

Figure 4.32 shows the straightening of the γ flash after the walk correction is implemented to the timestamps from the VANDLE PMTs.

4.6.3 Flight-path Correction

The β-delayed neutrons are emitted by ions from various locations of implantation in the YSO detector. The YSO detector has a volume of $75 \times 75 \times 5\ mm^3$. Hence, the flight path of all the neutron events will not be the same as 105 cm. The flight path of neutron events will have a distribution ranging from 101.24 cm to 108.75 cm. This can affect the energy measurement of the neutrons, primarily for high-energy neutrons with greater sensitivity to the flight path. In other words, for a given ToF the difference in energy calculated using the two possible extremes of flight path length (101.24 cm and 108.75 cm) can be quite large. To minimize the error in energy measurement, it is imperative to calculate the flight path for each neutron event using the dimensions of the YSO and the geometry of the setup. The position (X_i, Y_i, Z_i) of neutron emission on the face of the YSO is derived from the position of the correlated beta event using anger logic. The position (X_f, Y_f, Z_f) of a neutron event in a VANDLE bar is calculated from the product of the speed of light in the bar and the time difference between the left and right PMT signal. The flight path of a neutron event is calculated using the position coordinates in the YSO detector and VANDLE bar, by using the distance formula for two points in a Cartesian coordinates system.

$$L^{'} = \sqrt{(X_i - X_f)^2 + (Y_i - Y_f)^2 + (Z_i - Z_f)^2} \tag{4.41}$$

A graphical description of the method to correct for the flight path of neutrons based on the YSO dimensions is shown in 4.33. The ToF ($ToF^{'}$) for each flight path ($L^{'}$) is then scaled to a ToF corresponding to a flight path of 105 cm as follows:

$$ToF = ToF^{'}\left(\frac{105}{L^{'}}\right). \tag{4.42}$$

Figure 4.34 shows a comparison between ToF distributions with and without the flight path correction, based on the YSO dimensions. The spectra overall look similar but upon close examination, we do see some difference for events, mainly in the ToF range of 30-60 ns.

4.6.4 VANDLE GEANT4 Simulations

The neutrons on their way from the YSO detector to VANDLE bars will also scatter from various components of the setup. A mono-energetic neutron beam when shot directly at a VANDLE bar will have a ToF distribution that peaks at the ToF corresponding to the energy of the neutrons with tail components, which are due to delay in reaching the bar or scattering within the bar itself. Now, when VANDLE is simultaneously showered with neutrons with a broad energy distribution, the ToF spectrum resembles that of a continuous distribution where some of the neutron energy peaks might be buried under the tails of response from higher neutron energy. To extract out the peaks corresponding to individual transitions, and count the neutrons present in those transitions, it is necessary to have a characterization of the response of VANDLE for various neutron energies expected in the experiment. GEANT4 offers numerous tools to extract such information using tracking and energy deposition of various particles in different (liquid, solid, or gas) volumes. The availability of various libraries for creating particle sources allows estimates that otherwise might be difficult to perform in the laboratory. For example, it is quite challenging to get a VANDLE response with neutrons of a wide energy range in a laboratory for every different setup of the experiment. For the VANDLE experiment, a GEANT4 simulation toolkit was developed at the University of Tennessee, Knoxville. VANDLE bars were constructed as active scintillator materials in the setup. The geometry of the components in the implantation box (YSO, Light Guide, front and back Veto, and PSPMT) was loaded into the simulation package using Geometry Description Markup Language (GDML) files from Computer-aided Designs (CAD) files. BRIKEN detector present at the F11 focal plane

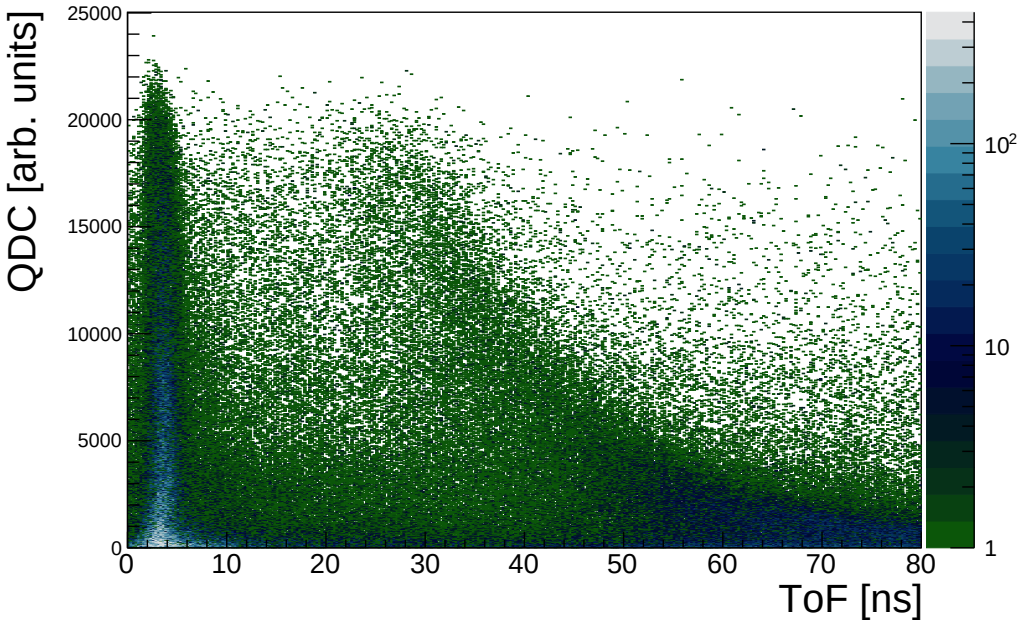


Figure 4.32: Gamma flash in ToF spectrum straightened after the walk-correction function is used to correct the time.

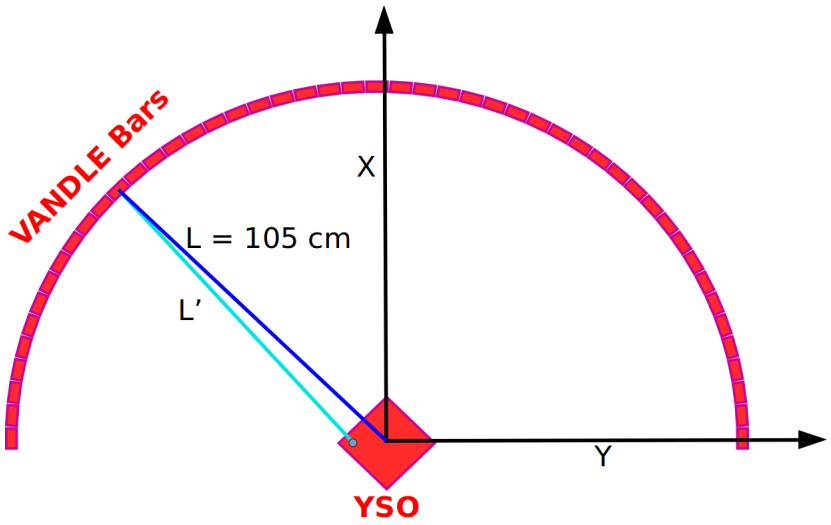


Figure 4.33: A graphical representation of the flight path possible due to the presence of YSO. The flight path ($L^{'}$) is the actual flight path of a neutron event.

was also imported as a polyethylene cube with a cavity. The aluminum frame was imported into the simulation as a Standard Tessellation Language (STL) object. HPGe detectors were loaded into the simulation as scattering materials using G4 volumes. To capture the possibility of the reflection of neutrons, a concrete floor was also added. Figure 4.35 shows a snapshot of the GEANT4 graphical user interface showing the geometry of all the components imported in the simulations. PMTs were implemented in the software to read signals from the VANDLE bars and trace analysis methods were also implemented to calculate the timing and QDC of signals induced by neutrons in the bars.

4.6.5 Response Function

The important information needed to de-convolve the neutron ToF spectrum, *i.e.*, extract peaks corresponding to transitions from the ToF spectrum is the response of the VANDLE to a broad range of neutron energy distributions. The response function of a VANDLE bar can be represented by a Gaussian peak with tails. The length of the tails and the onset of the tails on the Gaussian shoulder is decided by the scattering material encountered by the neutrons from YSO on their way to VANDLE. The scattered neutrons are the neutrons with the same energy as the neutrons in the main peak, but end up having a higher time of flight due to scattering with various materials in the setup. The amount of neutron scattering depends on the energy of the neutrons and the amount of scattering volume present. A number of simulations were performed for various neutron energies (0.03-7 MeV). To obtain the response, a neutron-point source producing a random distribution in space was placed at the center of the YSO detector. The response function was fitted with an asymmetric-Lorentzian function with three exponential-decay tail components. The mathematical description of the function is as follows:

$$\frac{1}{A}.f(t) = \begin{cases} \frac{1}{A_1}.\left[\frac{\sigma_0^2}{(t-t_o)^2+\sigma_0^2}(a_o+1) - a_o\right], & -\frac{1}{\sqrt{a_o}} \leq \frac{t-t_o}{\sigma_0} \leq 0 \\ \frac{1}{A_2}.\left[\frac{\sigma_1^2}{(t-t_o)^2+\sigma_1^2}\right], & 0 < \frac{t-t_o}{\sigma_1} \leq k_1+d_1 \\ \frac{1}{A_3}.b_1\exp(-k_1\frac{t-t_o}{\sigma_1}), & k_1+d_1 \leq \frac{t-t_o}{\sigma_1} \leq k_2+d_2 \\ \frac{1}{A_4}.b_2\exp(-k_2\frac{t-t_o}{\sigma_1}), & k_2+d_2 \leq \frac{t-t_o}{\sigma_1} \leq k_3+d_3 \\ \frac{1}{A_5}.b_3\exp(-k_3\frac{t-t_o}{\sigma_1}), & \frac{t-t_o}{\sigma_1} > k_3+d_3 \end{cases} \tag{4.43}$$

where,

$$b_1 = \frac{\exp(k_1(k_1+d_1))}{1+(k_1+d_1)^2}, \tag{4.44}$$

$$b_2 = \frac{\exp(k_1(k_1+d_1)-(k_1-k_2)(k_2+d_2))}{1+(k_1+d_1)^2}, \tag{4.45}$$

$$b_3 = \frac{\exp(k_1(k_1+d_1)-(k_1-k_2)(k_2+d_2)-(k_2-k_3)(k_3+d_3))}{1+(k_1+d_1)^2}. \tag{4.46}$$

Here, t_o denotes the peak position, a_o denotes the offset, k_1, k_2, and k_3 are the decay constants of the exponential tail components, d_1, d_2, and d_3 denote the onset of exponential tails after the peak. The normalization factor (A) can be written as the sum of the normalization of the function in various ranges as $\mathrm{A} = \sum_{i=1}^{5} A_i$.

Figure 4.36 shows the response function obtained from the simulations. The distribution has tail components after the peak and at the very long ToF values ($\sim$ 300 ns) there is a small bump in the distribution. The small bump is present for highly energetic ($>$ 1 MeV) neutrons. The bump is due to neutron reflections coming from the concrete floor. Overall, the effect of the concrete floor on the response function is small. The parameters ($a_o, \sigma_o, \sigma_1, k_1, k_2, k_3, d_1, d_2,$ and d_3) were obtained from the fit of the response function by using standard fitting libraries available in ROOT CERN package. The majority of the scattering in the setup is due to the components in the PSPMT box, which includes the YSO crystal, tapered light guide, and front plastic VETO detector. The response parameters were obtained by fitting the response of VANDLE to neutrons in the energy range of 0.03-4.0 MeV.

Figures 4.37 and 4.38 show the scattering of neutrons from the components in the immediate vicinity of the implantation. The majority of the scattering comes from the YSO crystal and the light guide as shown in the projections.

VANDLE Efficiency

The efficiency of the VANDLE array is needed for obtaining absolute β-decay feeding intensities to neutron-unbound energy levels in the daughter nucleus. Efficiency measurements for a medium VANDLE bar have been performed at Edwards Accelerator Laboratory at Ohio University [68]. Neutrons emitted in ^{27}Al(d, n)^{28}Si reaction with a broad (keV to MeV) energy distribution were impinged on a medium bar. The efficiency curve obtained by counting the number of neutrons at each energy is called the intrinsic efficiency curve, as it depends on the elemental composition of the bar, *i.e.*, scattering of neutrons with carbon and hydrogen present in EJ200 and propagation of scintillation light within the bar. The efficiency curve is sensitive to the QDC threshold applied in the Pixie-16 acquisition system. This sensitivity is more pronounced for low-energy neutrons which have low QDC and may end up in the vicinity of the threshold value. The efficiency curve sensitivity makes it essential to have an estimate of the thresholds to properly characterize efficiency for a given experimental setup. In total, neutron-detection efficiency of the VANDLE array depends on the geometry of arrangement of the bars, Pixie-16 threshold, and scattering experienced by mono-energetic neutrons. The simulation was tested for the setup of the intrinsic efficiency measurement at Edwards Accelerator Laboratory in terms of matching the results. A QDC calibration is required for the simulation and data to properly place a threshold. The QDC calibration for the simulation was achieved by adjusting the gain of the PMT in the simulation trace analysis routine. QDC spectra of a single bar using different γ-ray sources over a broad range of energy such as ^{241}Am, ^{137}Cs, and ^{60}Co were used to calibrate the VANDLE QDC spectrum. Standard sources were also placed in the simulation to obtain the gain-matched spectrum with the data. The calibration curve is plotted in Figure 4.39.

Simulations were performed with the adjusted gain for a single bar with a mono-energetic source placed at a distance of 105 cm from the bar. Figure 4.40 shows the efficiency of a

single bar for various QDC thresholds implemented in the simulation. A scaling factor of 0.85 was introduced to scale the efficiency curve from the simulation to achieve agreement with the measurement at Edwards Accelerator Laboratory.

The settings obtained for simulating a single bar such as QDC threshold, PMT gain, timing analysis, material definition, and scintillation properties of EJ200 are preserved for simulating the efficiency of the VANDLE array. For the simulation, a point and isotropic neutron source was placed at the center of the YSO crystal. Efficiency was calculated by counting the number of neutrons in the main peak and the tail of the ToF spectrum of each neutron energy. Figure 4.41 shows the efficiency of the VANDLE array obtained from the simulation.The error bars are assigned to the data points based on the uncertainty in the threshold value determination. The error bars are higher for low-energy neutrons due to sensitivity to the threshold value and are lower for high-energy neutrons. The mathematical expression for calculating error is written in Equation 4.47.

$$\delta_{Eff}(E_i) = |Eff(T, E_i) - Eff(T + \Delta, E_i)| \tag{4.47}$$

Here, $\delta_{Eff}(E_i)$ denotes the error in efficiency for a specific neutron energy E_i. $Eff(T, E_i)$ denotes the efficiency calculated with a threshold T, and $Eff(T + \Delta, E_i)$ denotes the efficiency calculated with threshold $T + \Delta$ with Δ denoting uncertainty in the threshold.

4.6.6 Designing Neutron Gate

The relationship between the QDC maximum for given neutron energy and the corresponding time of flight can be used to set a decision boundary for permissible neutron events and noise/spurious events incurred in the spectrum. The relationship can be derived from a graph of the simulated-gain-matched QDC vs ToF spectrum for different nuclear energy. The neutron events lying below the curve (upper boundary) are deemed as signals whereas the ones lying outside are deemed as noise. For the lower boundary, neutron events bearing ToF above the $Q_\beta - S_n$ value were accepted. The lower boundary is specific to the nucleus chosen for the analysis.

4.6.7 Background Subtraction

The neutron ToF spectrum for a particular isotope after gating with the ion-beta correlation time window includes actual correlated neutron events and the mis-correlated neutron events due to the background incurred in establishing ion-beta correlations. The events in the background are due to the ions with high neutron-emission branching ratios that pollute the ToF spectrum of other ions. The knowledge of the relative timing information of ion-beta events can be used to account for the background in the spectrum. Neutrons correlated in a positive ion-beta time window (T) include the Signal (S) and the Background (B). The background is determined by obtaining a neutron ToF spectrum by gating on a negative time window (-T). This spectrum contains only the background. The signal (actual correlated neutrons) is obtained by subtracting the two spectra on a bin-by-bin basis. A similar approach is adopted by obtaining gamma-ray spectra from $LaBr_3$ and HPGe detectors for analyzing γ-transitions for any given isotope. Figure 4.43 shows the methodology adopted to sample the signal (S) and background (B) using the decay curve.

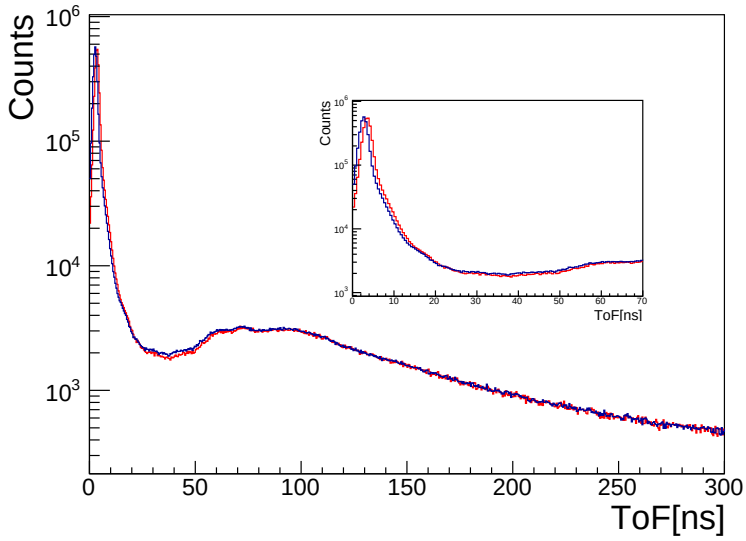


Figure 4.34: ToF spectrum of neutron events before (blue) and after(red) correcting for the flight path using YSO dimensions.

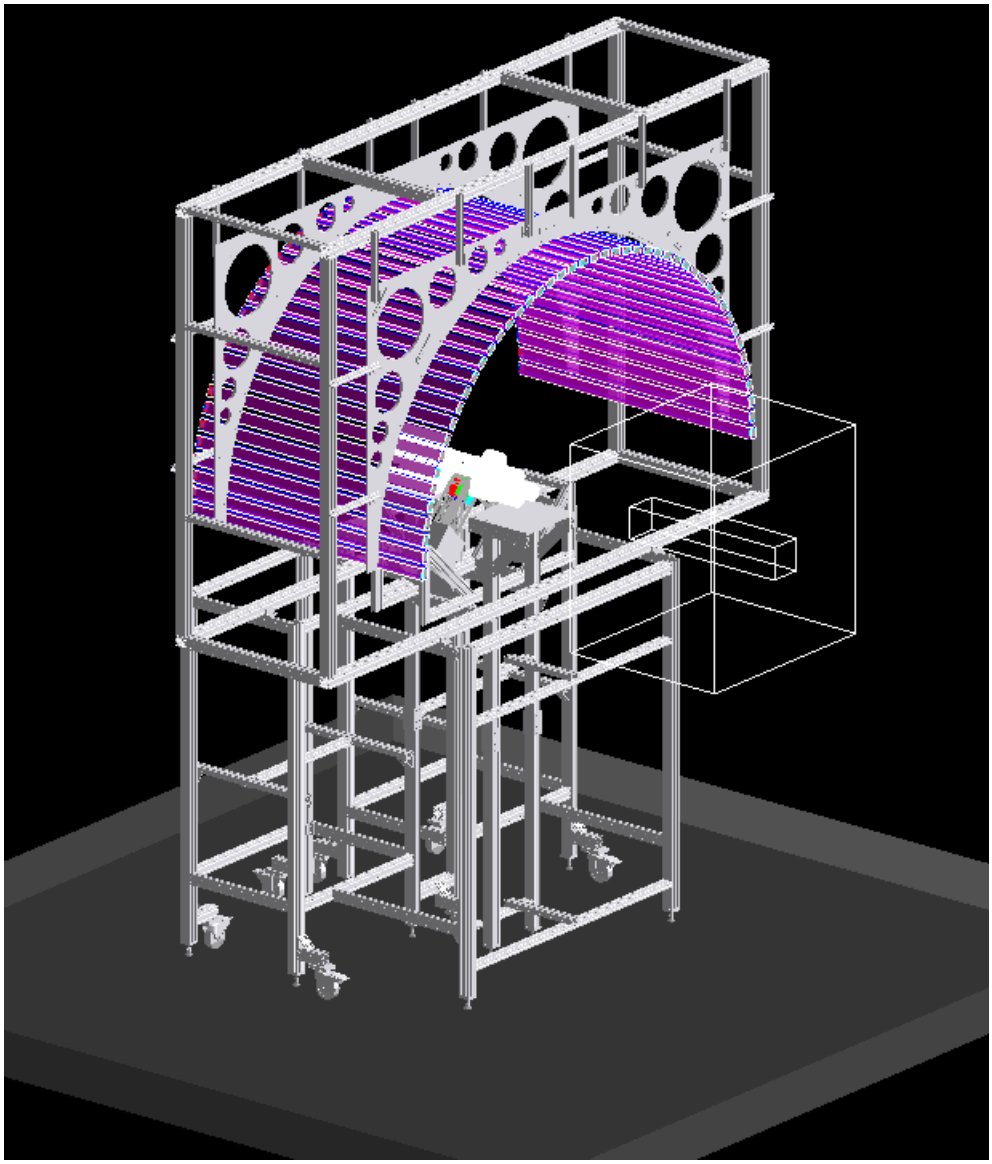


Figure 4.35: Geometry of the complete experiment imported into the GEANT4 simulation package.

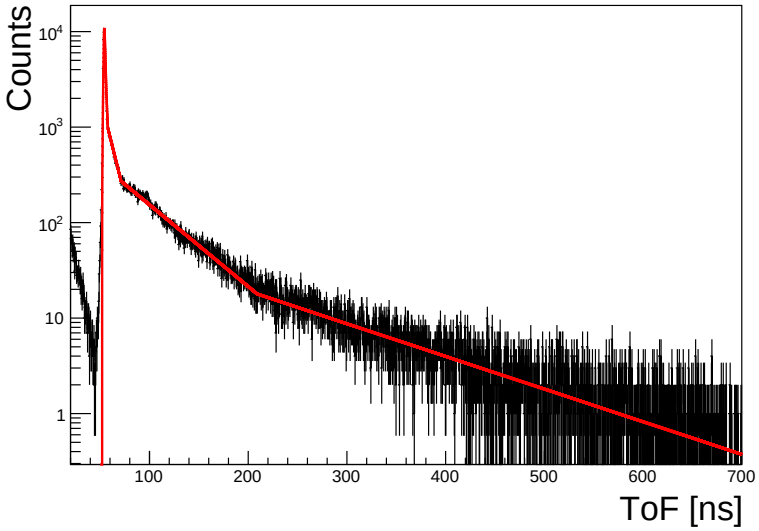


Figure 4.36: VANDLE response to 2-MeV neutrons for the experiment setup. The response function is fitted with an asymmetric Lorentzian function with exponential tails.

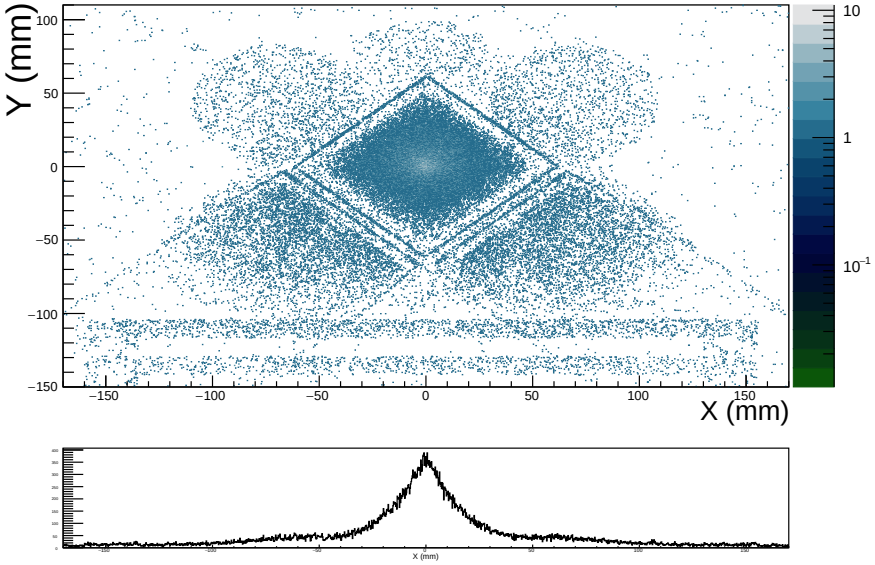


Figure 4.37: Scattering of neutrons as seen from the frame of reference of the beam. The main source of scattering is the PSPMT box as seen in the projections of the scattering points along x-axis.

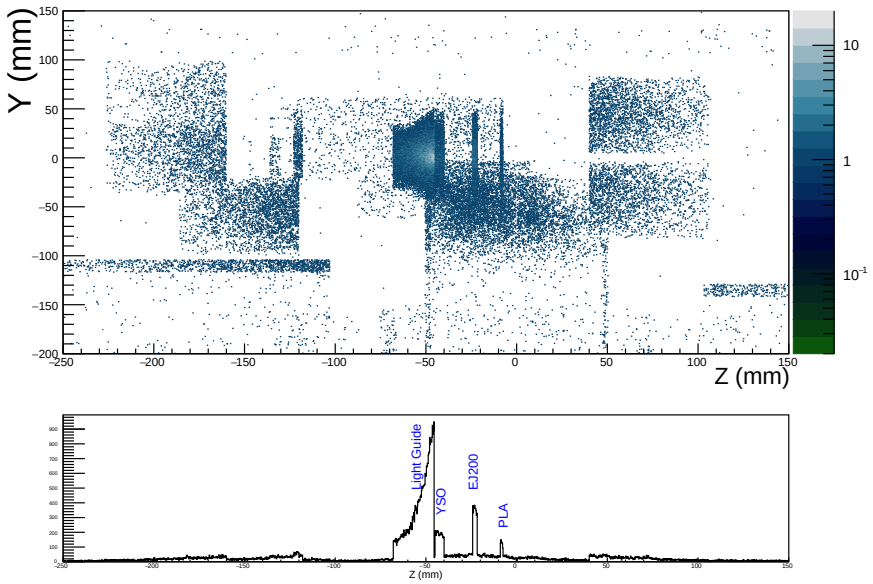


Figure 4.38: Scattering of neutrons as seen along the z-axis. The projection of the scattering points shows the scattering of neutrons around the implantation point.

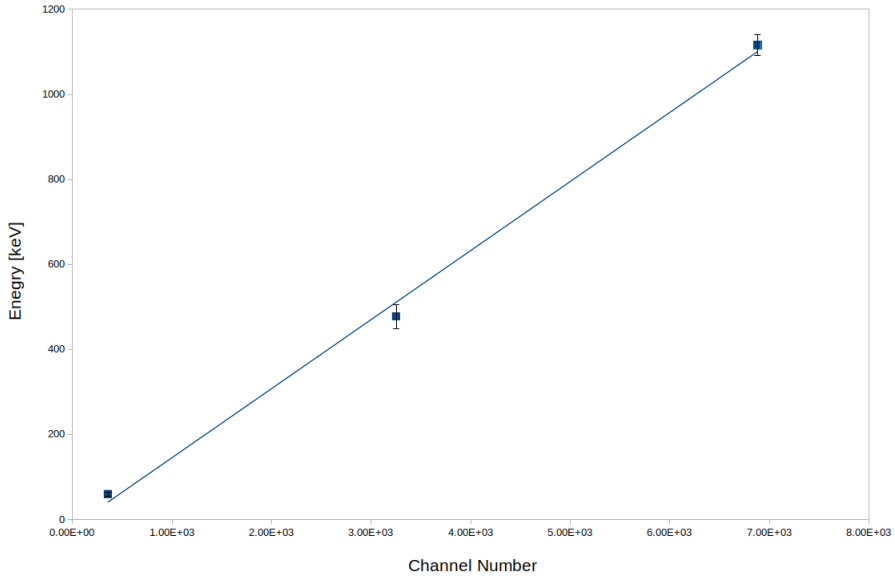


Figure 4.39: Calibration of VANDLE QDC using ^{241}Am Photopeak and Compton edge of ^{137}Cs and ^{60}Co.

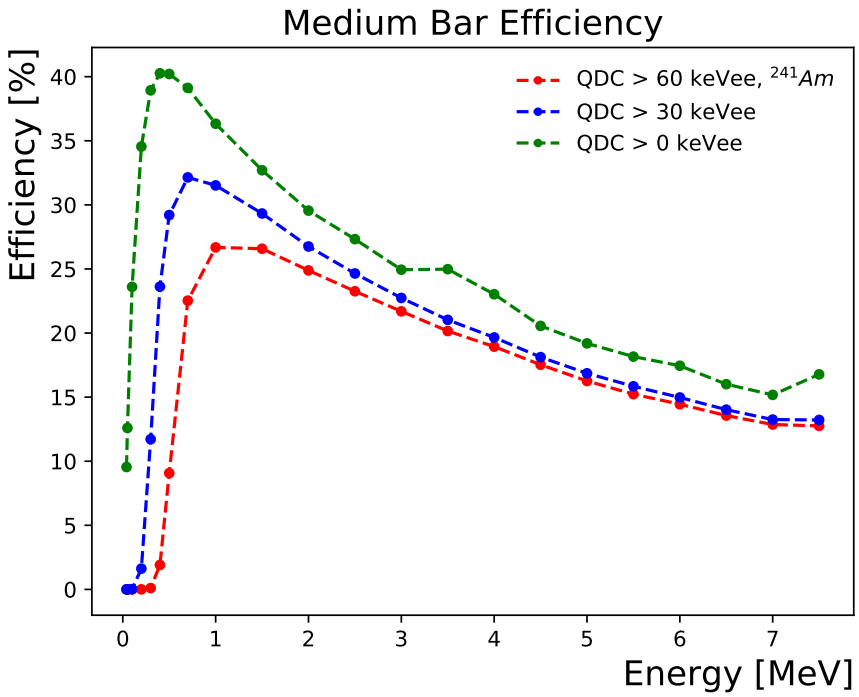


Figure 4.40: Neutron-detection efficiency of a single medium VANDLE bar calculated using GEANT4.

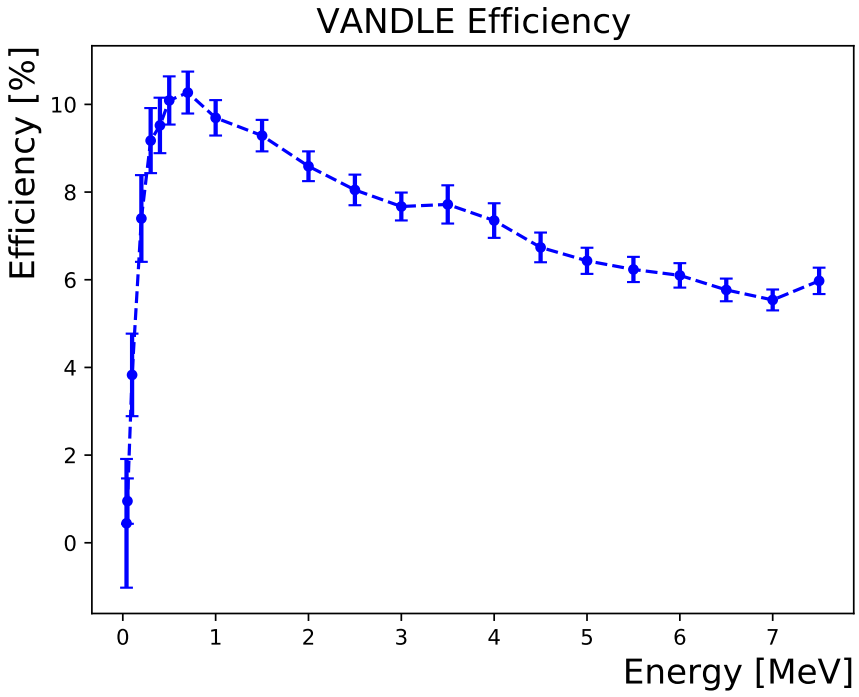


Figure 4.41: Neutron-detection efficiency of the VANDLE array setup in the experiment, calculated using GEANT4.

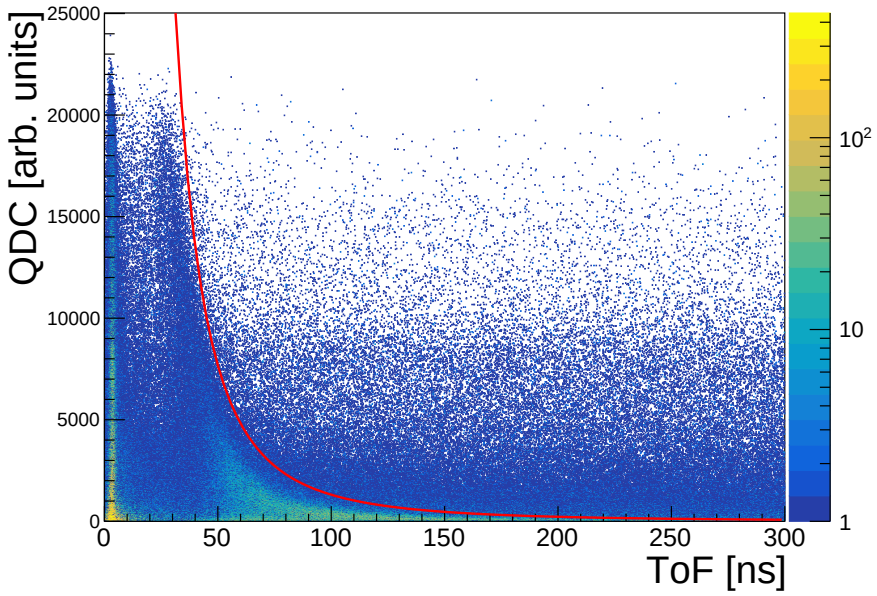


Figure 4.42: QDC versus ToF parameterization obtained from simulation and overlaid onto the data. The neutron events below the curve are deemed permissible for the analysis.

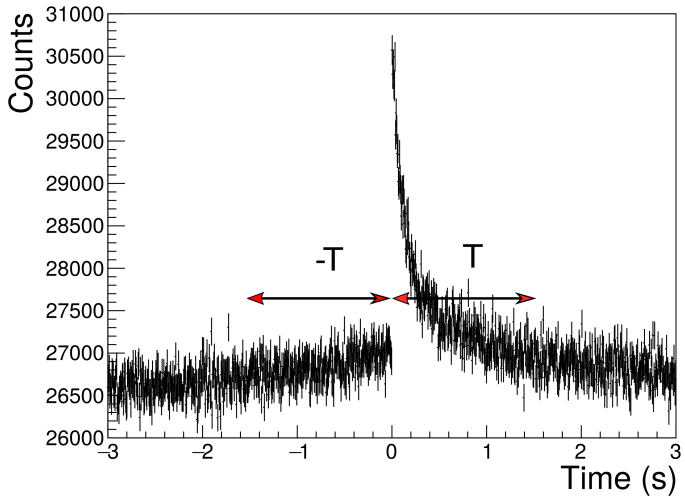


Figure 4.43: Decay curve of ^{80}Cu with timing windows for sampling signal plus background (S+B) in time (T) and the background (B) in time (-T).

Chapter 5

Results

5.1 Beta decay of ^{79,80,81}Cu

Cu isotopes with N$\geq$ 50 were implanted into the YSO detector over a period of 5 days. The number of $^{79,\ 80,\ 81}$Cu ions implanted into the YSO are 1.5 $\times$ 10^6, 1.1 $\times$ 10^6, and 1.9 $\times$ 10^3, respectively.

5.1.1 ^{79}Cu Analysis

^{79}Cu decays to ^{79}Zn with a half-life of 241.0 $\pm$ 2.1 *ms* [69]. The delayed-neutron emission probability is measured to be 72 $\pm$ 12 % by P. Hosmer, *et al.*, 2010 [70]. To obtain the neutron singles spectrum an ion-beta gate of 600 *ms* is chosen to collected 82 % of ^{79}Cu decays during $\sim$ 2.5 half-lives. Figure 5.1 shows the expected decay scheme of the isotope to ^{79}Zn and the decay of ^{79}Zn into ^{78}Zn via neutron emission. Figure 5.2 shows the neutron spectrum as gated on the beta events in the decay of ^{79}Cu and the spectrum is deconvoluted using the evaluated response function. The identified neutron-emitting states and the corresponding branching ratios and *log(ft)* values are listed in table 5.1.

Coincidences between neutrons emitted from excited states in ^{79}Zn and $2^+ \rightarrow 0^+$ transition of 730 keV in ^{78}Zn are identified. Figure 5.3 shows the ToF spectrum of neutron events in coincidence. The neutrons states identified in this spectrum are a subset of the

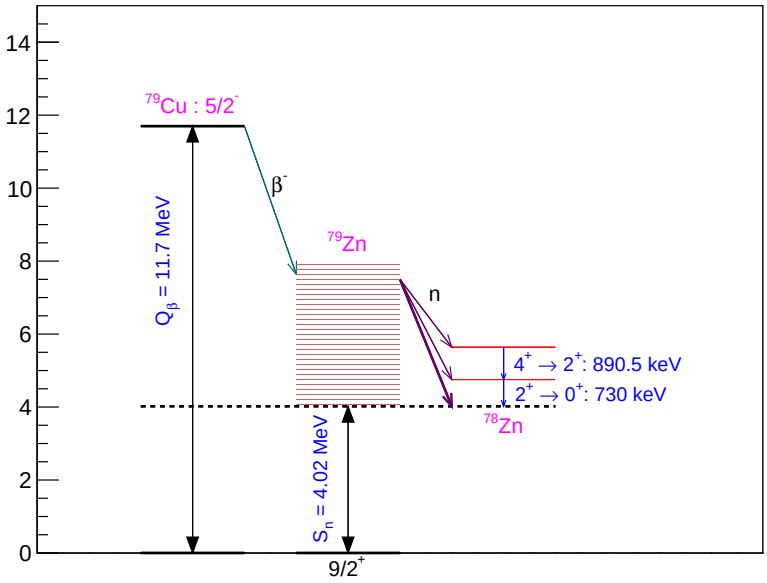


Figure 5.1: Expected decay path of ^{79}Cu and the schematic of neutron emission from neutron unbound states in ^{79}Zn. The neutron emission can lead to a direct population of the 0^+ ground state or 2^+ excited state in ^{78}Zn.

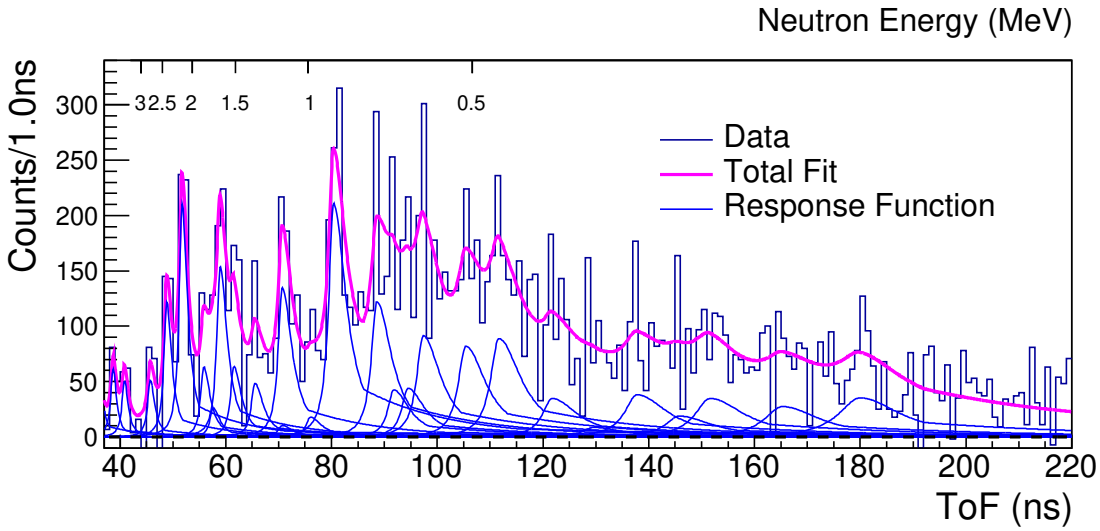


Figure 5.2: ToF neutron spectrum of ^{79}Cu obtained from VANDLE with an ion-beta correlation gate of 600 *ms*.

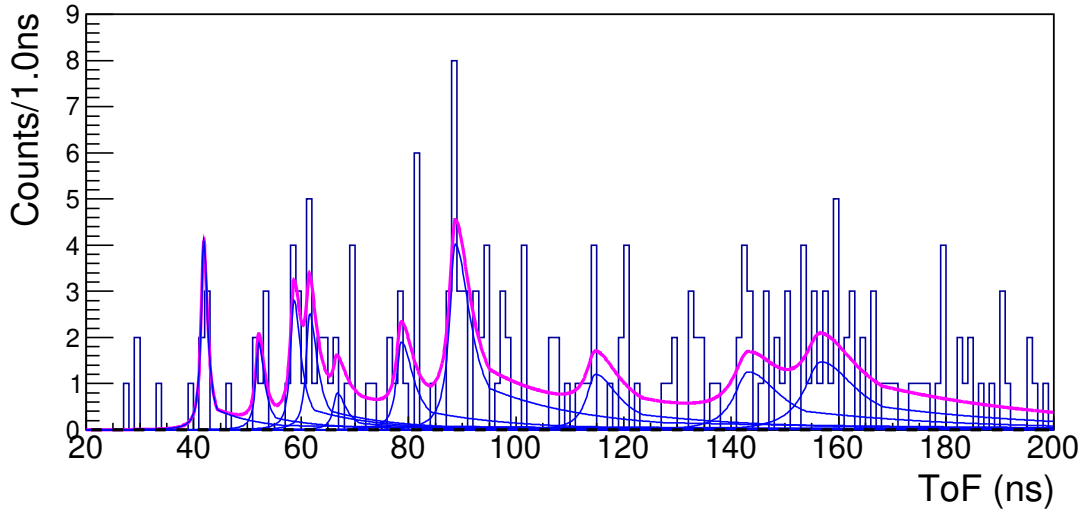


Figure 5.3: ToF spectrum of neutrons in coincidence with the 730-keV transition in ^{78}Zn.

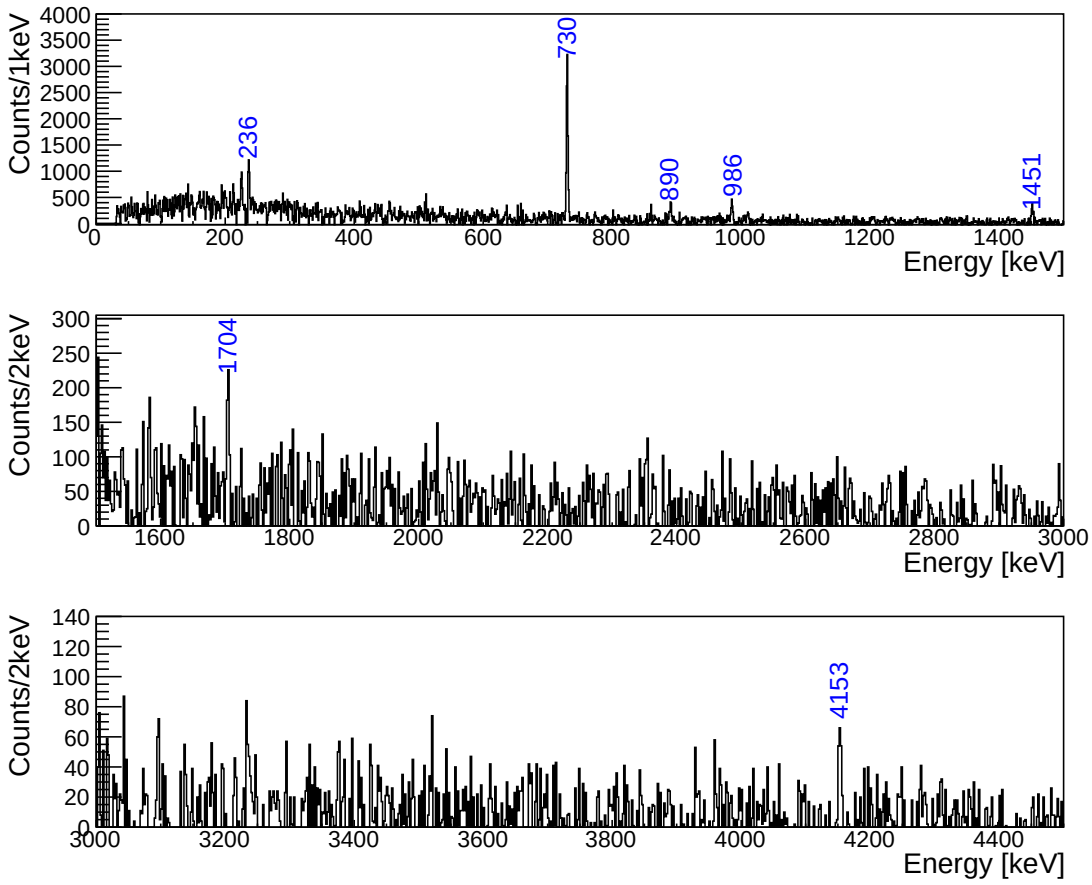


Figure 5.4: Beta-gated γ-ray spectrum of ^{79}Cu obtained from Clovers with an ion-beta gate of 600 *ms*.

neutron states identified from the "singles" spectrum. These identified states are shifted in energy by 730 keV for their placement in the beta-strength distribution.

The γ-lines identified in the decay are also shown in Figure 5.4. The *log(ft)* values of these transitions are calculated using the established decay scheme and are plotted in Figure 5.5. A newly identified γ-ray transition of 4153-keV is also identified in this experiment. The half-life of the line is also measured as shown in Figure 5.6. The placement of the line in the decay scheme is still ambiguous because of the absence of any gamma-gamma coincidences. However, various scenarios of placement of the line within the decay scheme using angular momentum selection rules are shown in Figure 5.7.

As each individual neutron transition corresponds a number of transitions condensed in a single peak, given the limited resolution of the VANDLE array for high neutron energies, error bars for the calculated neutron energy using the FWHM of the response function corresponding to the transition in ToF space. The FWHM in ToF space is translated to the energy space using the path length of 105 cm.

The strength distribution (S_β) is calculated for each identified neutron energy peak. Now, the strength associated with a single energy peak may be a contribution from closely separated neutron transitions which are not resolved due to the resolution of the detector. To show the contribution from the unresolved peaks the strength from each individual peak is spread over energy using a Gaussian profile with FWHM calculated from the data. The Gaussian-broadened beta-strength distribution is plotted in Figure 5.8.

5.1.2 ^{80}Cu

β-decay half-life of ^{80}Cu was measured to be 170^{+110}_{-50} *ms* by P. Hosmer, *et al.,* 2010 at NSCL [70]. There is no P_n value measurement reported so far, but a value of 60 $\pm$ 20 % is provided by Xu *et al.*, 2014 [69]. The nucleus has $Q_\beta - S_n = 9.2 \pm 0.9$ MeV [71]. A decay scheme of the nucleus is shown in Figure 5.9. An analysis technique similar to that for ^{79}Cu is performed, where neutron events are selected with respect to beta for a timing gate of 300 *ms*. Figure 5.10 shows the neutron ToF spectrum of β-delayed neutrons emitted from excited states in ^{80}Zn. The spectrum is fitted with the VANDLE response function for the experiment. For the decay of ^{80}Cu no coincidences were identified between the neutrons emitted from

Table 5.1: Neutron-emitting states and the corresponding neutron transitions identified in ^{79}Zn

Sr.No.	ToF (ns)	Energy (keV)	Exc. Energy (keV)	Branching Ratio (%)	*log(ft)*
1	41.15	3483(242)	8278(244)	0.58(0.07)	4.88(0.18)
2	46.05	2759(197)	6815(199)	0.61(0.09)	5.55(0.15)
3	49.18	2406(176)	6457(178)	1.50(0.18)	5.29(0.13)
4	52.1	2135(161)	6912(162)	2.69(0.29)	4.85(0.13)
5	56.23	1825(143)	5868(144)	0.87(0.14)	5.74(0.13)
6	58.03	1711(139)	5753(140)	0.37(0.23)	6.15(0.22)
7	59.36	1634(133)	6405(134)	2.22(0.32)	5.14(0.12)
8	61.96	1498(125)	6267(126)	0.96(0.17)	5.55(0.12)
9	65.97	1320(115)	6087(116)	0.79(0.14)	5.7(0.12)
10	71.17	1133(104)	5168(105)	2.41(0.28)	5.53(0.11)
11	76.54	979(95)	5012(95)	0.35(0.14)	6.41(0.16)
12	80.95	875(88)	5636(88)	4.51(0.48)	5.1(0.1)
13	89.19	721(78)	5480(78)	3.03(0.37)	5.32(0.17)
14	92.4	671(75)	4700(75)	1.11(0.35)	6.00(0.14)
15	95.11	634(73)	4662(73)	1.21(0.45)	5.98(0.16)
16	98.01	597(70)	4624(70)	2.65(0.40)	5.65(0.10)
17	106.11	509(63)	4536(63)	2.72(0.33)	5.66(0.1)
18	112.41	453(58)	5209(58)	3.28(0.37)	5.38(0.1)
19	122.58	381(52)	4406(52)	1.51(0.21)	5.96(0.1)
20	130.47	337(48)	4361(48)	0.42(0.14)	6.52(0.15)
21	138.75	298(44)	4321(44)	2.12(0.29)	5.83(0.10)
22	146.77	266(40)	5019(40)	1.18(0.48)	5.88(0.2)
23	152.64	246(38)	4269(38)	2.36(0.44)	5.80(0.11)
24	166.41	207(33)	4959(33)	2.26(0.36)	5.61(0.16)
25	181.2	174(28)	4197(28)	3.56(0.43)	5.64(0.09)
				47.4(8.6)	

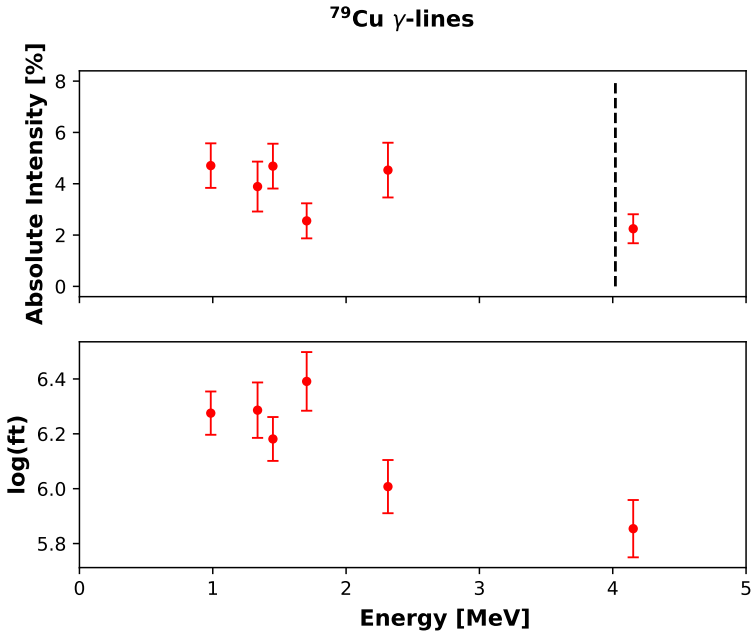


Figure 5.5: Absolute intensity (top) and calculated *log(ft)* (bottom) of all the γ lines identified in the decay of ^{79}Cu.

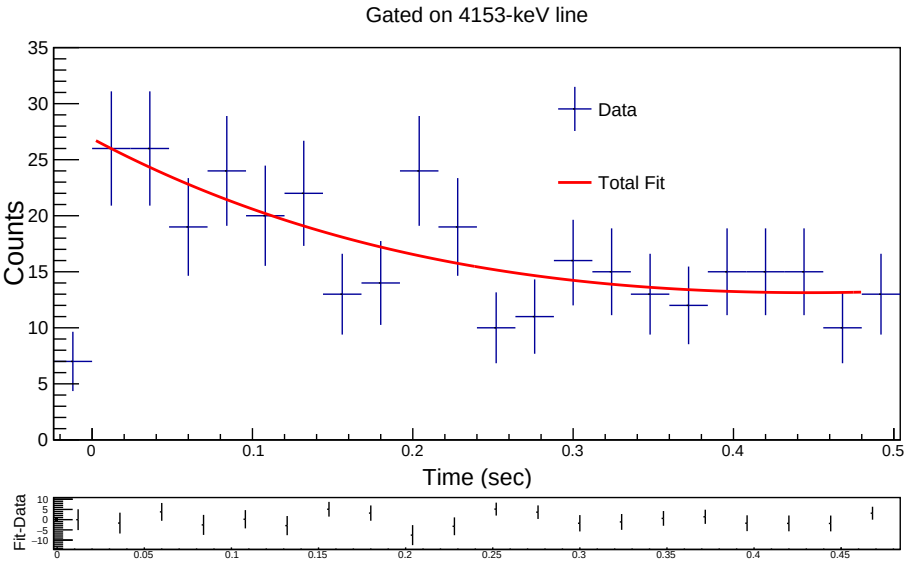


Figure 5.6: Decay curve gated on the 4153-keV line in the β-decay of ^{79}Cu gives a half-life of 268.1 $\pm$ 45.6 *ms*. The upper panel shows the fit of the decay curve using Bateman Equation, and the lower panel shows the difference between the fitted curve and data.

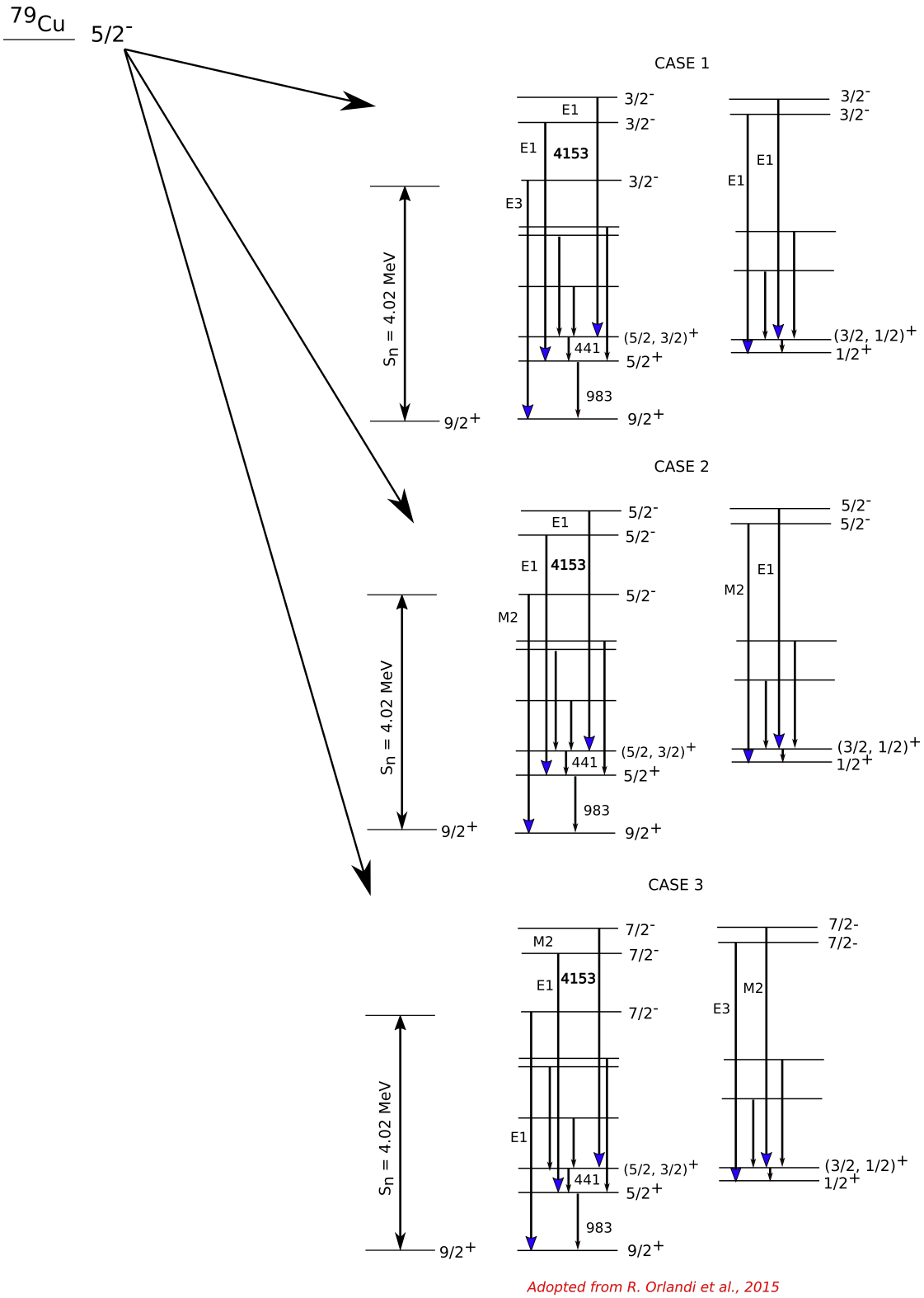


Figure 5.7: Various scenarios for the placement of the 4153-keV line in the decay scheme of ^{79}Cu based on the selection rules of total angular momentum with initial states being $3/2^-, 5/2^-$, or $7/2^-$. The arrows with blue head denote the 4153-keV transition.

excited states in ^{80}Zn and electromagnetic transitions in ^{79}Zn, due to limited statistics and low neutron- and γ-detection efficiencies. However, the β-gated HPGe spectrum shows the presence of the $5/2^- \rightarrow 9/2^+$ transition at 986 keV in ^{79}Zn. The identified neutron-emitting states and the corresponding branching ratios and *log(ft)* values are listed in Table 5.2. The challenge to construct beta-strength function in the decay of ^{80}Cu is posed by the presence of an isomeric state in ^{79}Zn. It is imperative to obtain information on feeding of neutrons to $5/2^-$ and isomeric state in ^{79}Zn to accurately deduce beta-decay strength distribution. But a tentative Gaussian-broadened beta-strength function is calculated, as shown in Figure 5.12.

The β-decay feeding intensities via 986-keV and 1492-keV are estimated to be 5.1(1.8) % and 8.3(2.1) %, respectively.

5.1.3 ^{81}Cu

^{81}Cu β decays to ^{81}Zn with a measured half-life of 68.5 $\pm$6.8 ms, provided by Xu *et al.*, 2014 [69] using beta-decay experiments. A $Q_\beta - S_n$ value of 12.2 MeV is reported by Wang *et al.*, 2012 [71]. A P_n value of 65 $\pm$ 20 % is reported by Xu *et al.*, 2014 [69]. For analyzing β-delayed neutrons, an ion-beta gate of 180 ms is chosen. The neutron ToF spectrum is deconvoluted using the response function obtained from the simulations. Figure 5.14 shows ToF spectrum of neutrons, emitted in the energy range $\sim$ 6.0-0.3 MeV from excited states in ^{81}Zn. The identified neutron-emitting states and the corresponding branching ratios and *log(ft)* values are listed in Table 5.3. Due to the limited number of implants of ^{81}Cu in YSO, and given the efficiency of gamma detectors in the setup, neutron-gamma coincidences between delayed neutrons and γ-ray transitions in ^{80}Zn remain unidentified. However, the $2^+ \rightarrow 0^+$ transition of 1492-keV and $4^+ \rightarrow 2^+$ transition of 482-keV were identified in the β-gated clover spectrum, giving evidence for possible coincidences. Figure 5.15 shows the lines clearly identified in the β-gated clover spectrum. The β-decay feeding via the 482-keV and 1492-keV lines in the decay are estimated to be 9.4(3.8) % and 26.7(4.8) %, respectively. Given the strong presence of the 1492-keV line in the spectrum, it is expected that most of the neutrons emitted from ^{81}Zn will populate 2^+ excited state in ^{80}Zn. Therefore, the

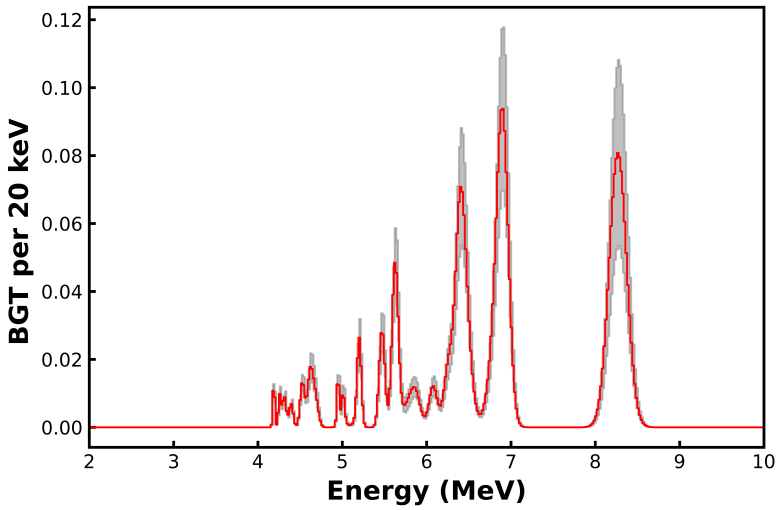


Figure 5.8: Reduced transition probability B(GT) to neutron-unbound states in the decay of ^{79}Cu. The red curve shows the probability distribution and the shaded-gray area is the error in the measurement.

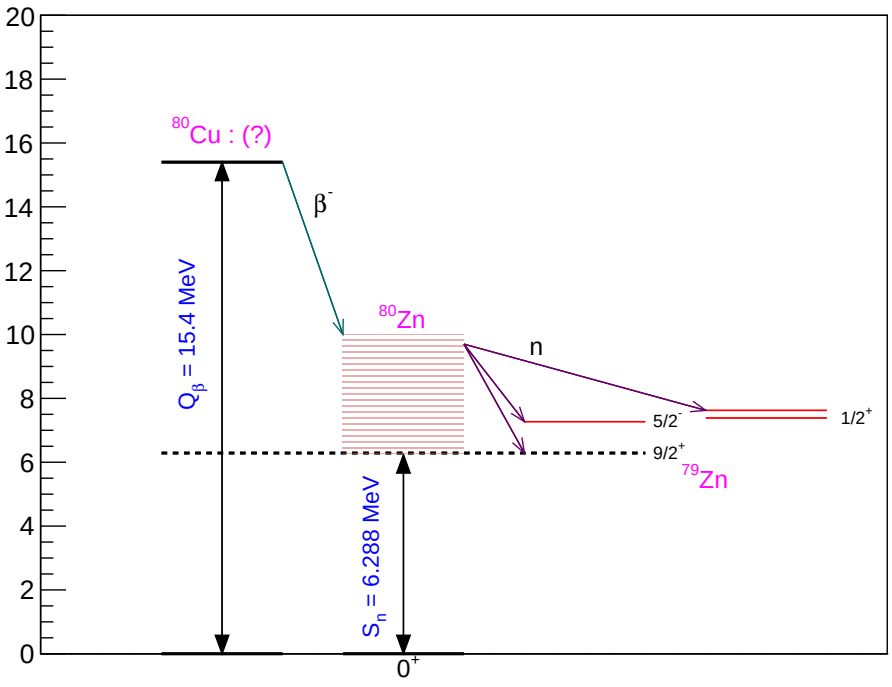


Figure 5.9: Expected decay path of ^{80}Cu and a schematic of neutron emission from neutron-unbound states in ^{80}Zn.

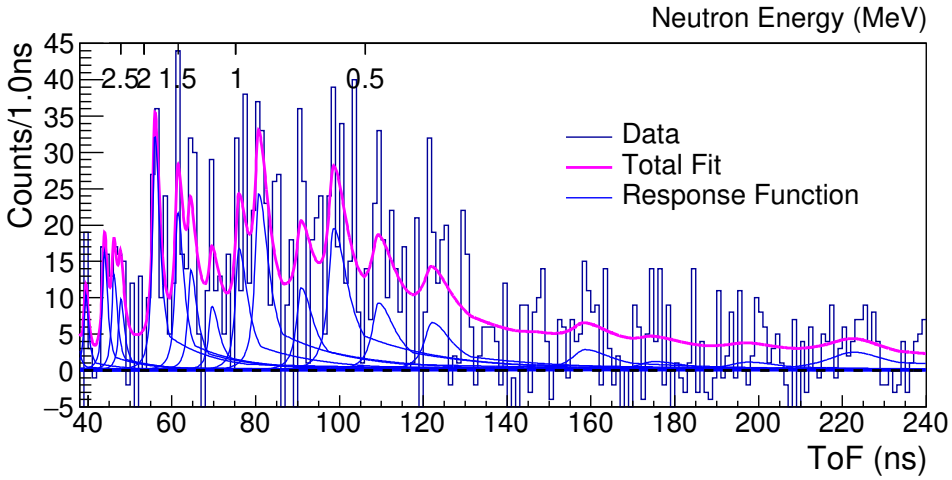


Figure 5.10: β-gated neutron spectrum of ^{80}Cu fitted using χ^2 minimization.

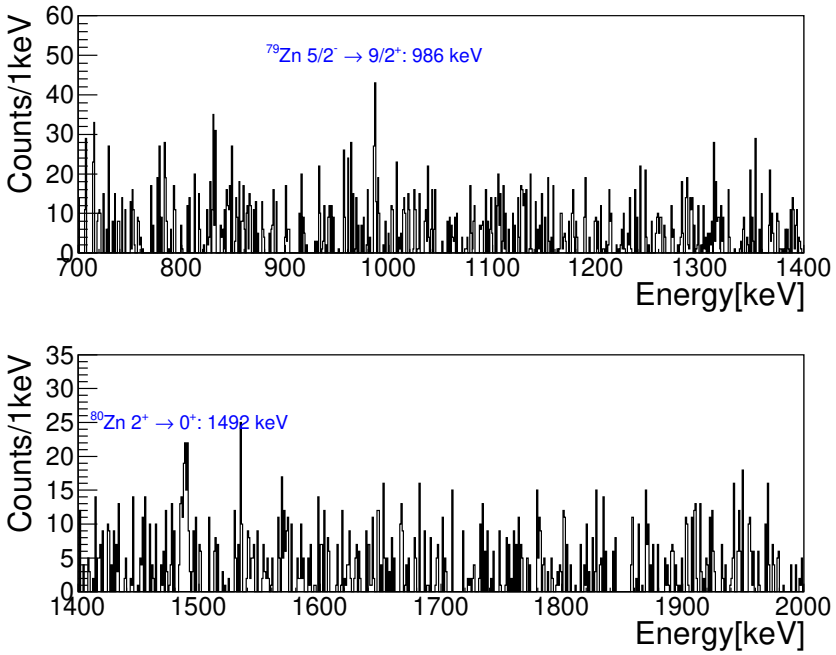


Figure 5.11: Beta-gated γ-ray spectrum of ^{80}Cu obtained using Clovers with an ion-beta gate of 300 *ms*.

Table 5.2: Neutron-emitting states identified in ^{80}Zn

Sr.No.	ToF (ns)	Energy (keV)	Exc. Energy (keV)	Branching Ratio (%)	*log(ft)*
1	39.77	3697(257)	10032(260)	1.59(0.45)	4.98(0.14)
2	44.12	2986(218)	9312(220)	2.02(1.82)	5.13(0.28)
3	47.26	2588(188)	8909(190)	2.88(0.74)	5.11(0.11)
4	45.26	2833(238)	9156(240)	1.02(1.57)	5.48(0.41)
5	50.86	2222(168)	8538(169)	0.42(0.36)	6.05(0.27)
6	56.33	1800(142)	8111(143)	5.90(0.98)	5.03(0.08)
7	61.85	1488(125)	7795(126)	4.41(0.89)	5.25(0.09)
8	64.95	1349(116)	7654(117)	2.97(0.77)	5.46(0.11)
9	70.01	1160(106)	7462(107)	2.08(0.64)	5.66(0.12)
10	76.5	971(94)	7271(94)	4.42(0.97)	5.39(0.09)
11	81.2	861(87)	7160(87)	6.75(1.29)	5.23(0.08)
12	85.21	782(83)	7080(83)	0.63(0.85)	6.28(0.37)
13	91.47	679(75)	6975(75)	3.94(0.95)	5.51(0.10)
14	99.26	576(68)	6871(68)	8.05(1.35)	5.23(0.07)
15	110.03	469(60)	6763(60)	4.75(1.06)	5.48(0.09)
16	122.9	376(51)	6668(51)	4.44(0.99)	5.53(0.09)
17	160.27	221(35)	6512(35)	6.17(1.13)	5.43(0.08)
				62.43(12.0)	

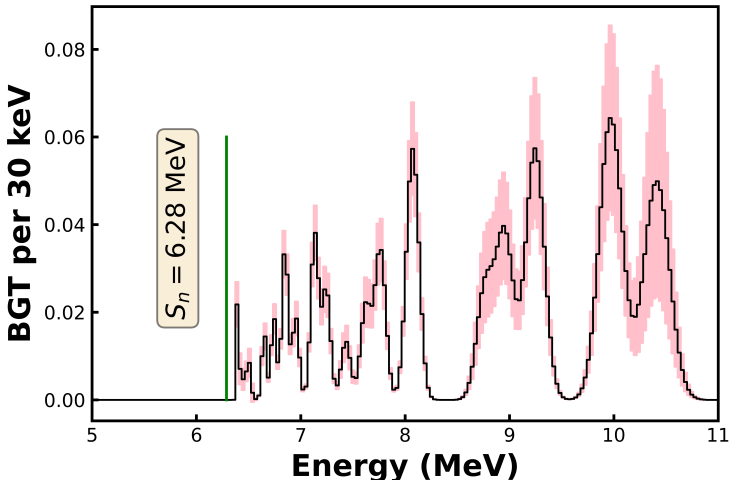


Figure 5.12: Reduced transition probability B(GT) to neutron-unbound states in the decay of ^{80}Cu. The black curve shows the probability distribution and the shaded-pink area is the error in the measurement.

beta-strength distribution obtained from neutron transitions from this data set is shifted in excitation energy by 1492 keV. The beta-strength distribution is plotted in Figure 5.16.

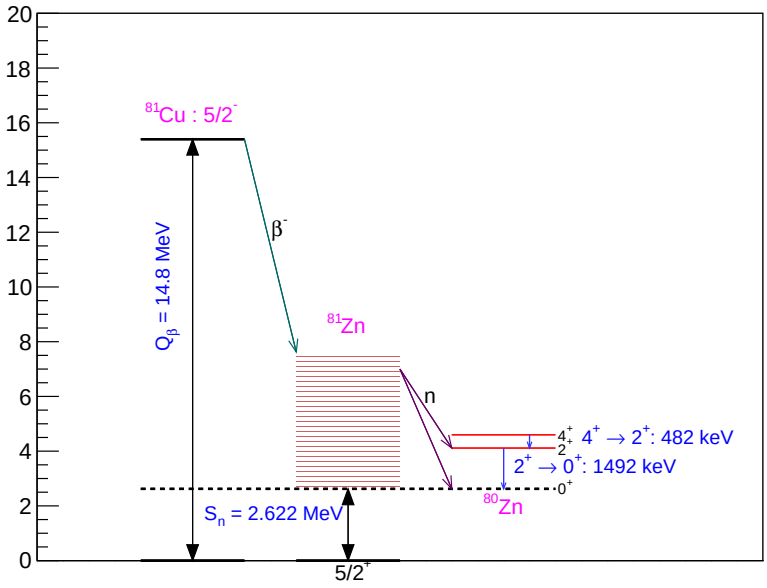


Figure 5.13: Expected decay path of ^{81}Cu and a schematic of neutron emission from neutron unbound states in ^{81}Zn.

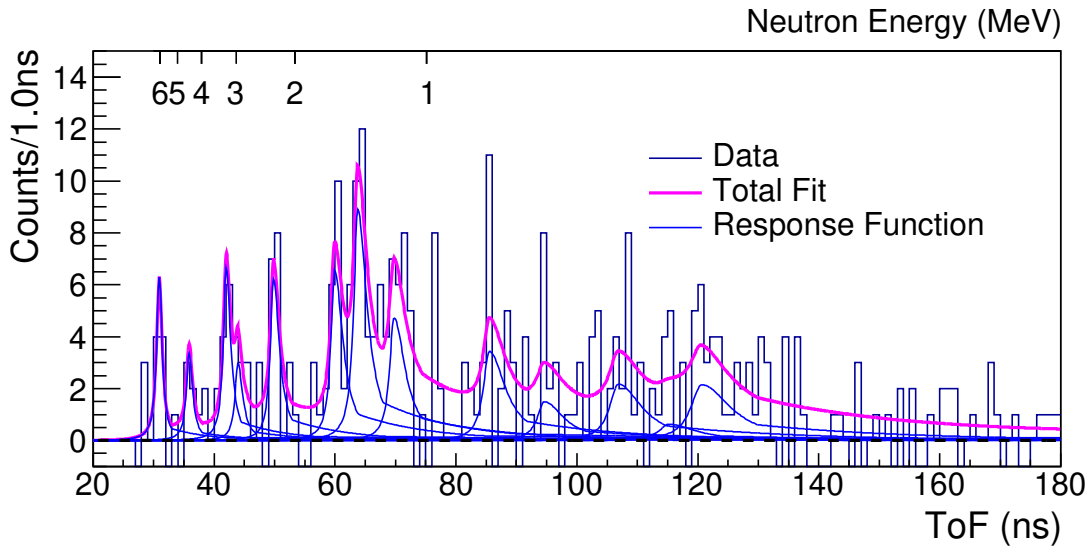


Figure 5.14: Beta-gated neutron ToF spectrum of ^{81}Cu deconvoluted using χ^2 minimization.

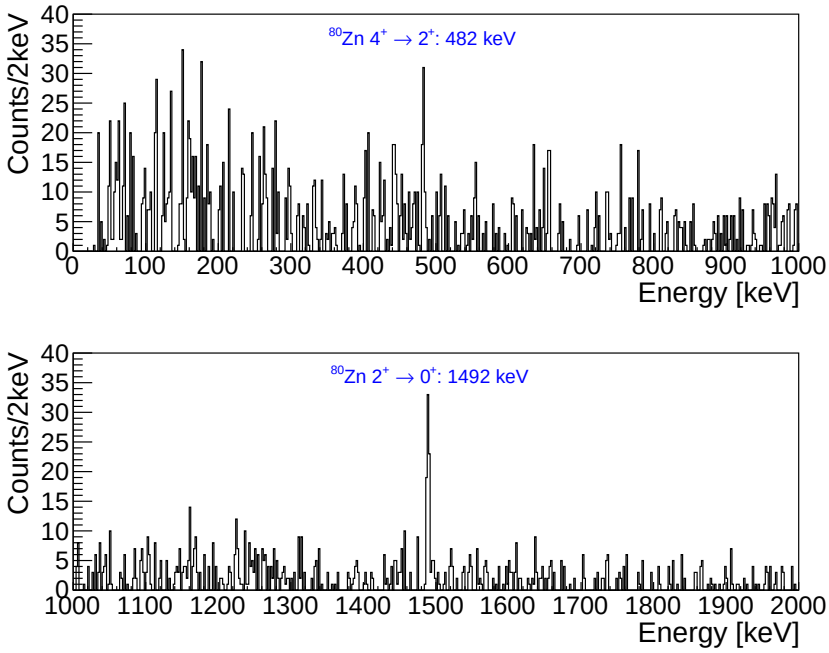


Figure 5.15: Beta-gated γ-ray spectrum of ^{81}Cu obtained from Clovers with an ion-beta gate of 180 *ms*.

Table 5.3: Neutron-emitting states identified in ^{81}Zn

Sr.No.	ToF (ns)	Energy (keV)	Exc. Energy (keV)	Branching Ratio (%)	*log(ft)*
1	31.18	6058(442)	8755(446)	6.48(2.14)	4.42(0.24)
2	36.13	4494(323)	7172(326)	2.91(1.48)	5.25(0.22)
3	42.31	3256(231)	5919(233)	5.65(2.45)	5.28(0.19)
4	44.25	2967(221)	5626(223)	2.55(1.57)	5.69(0.23)
5	50.16	2286(171)	4936(172)	5.71(1.93)	5.49(0.16)
6	60.33	1565(130)	4207(131)	7.10(2.08)	5.55(0.15)
7	64.18	1381(120)	4021(121)	10.32(3.02)	5.43(0.15)
8	70.22	1152(105)	3789(106)	6.12(1.88)	5.70(0.15)
9	86.08	766(82)	3398(82)	5.96(1.94)	5.79(0.15)
10	95.24	626(72)	3255(72)	3.05(1.54)	6.11(0.20)
11	107.53	491(62)	3119(62)	5.48(1.87)	5.88(0.15)
12	115.98	422(57)	3049(57)	1.81(2.76)	6.37(0.41)
13	121.44	385(53)	3011(53)	6.80(3.17)	5.80(0.18)
				69.91(21.40)	

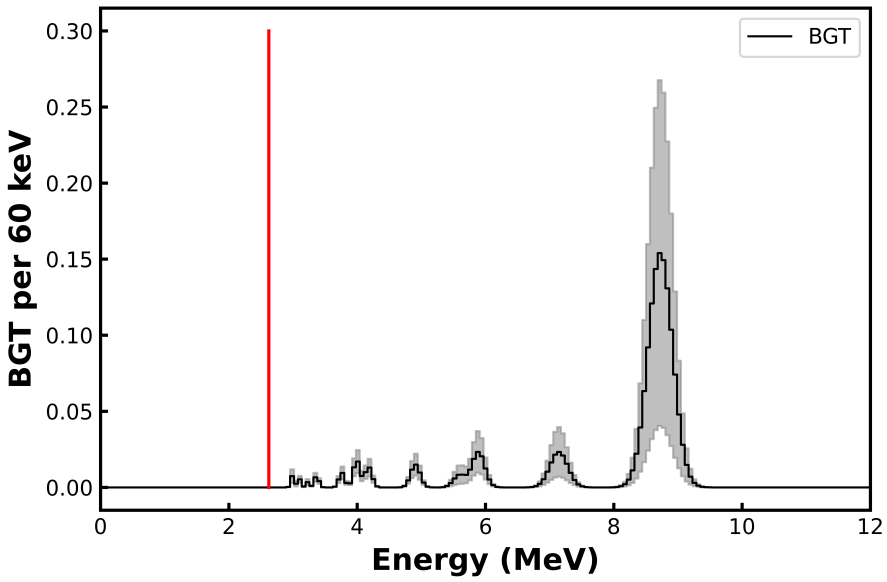


Figure 5.16: Reduced transition probability B(GT) to neutron-unbound states in the decay of ^{81}Cu. The black curve shows the probability distribution and the shaded-gray area is the error in the measurement. The vertical red line denotes the neutron separation energy of ^{81}Zn.

Chapter 6

Discussion

^{78}Ni is a doubly magic nucleus with 50 neutrons and 28 protons. A recent experiment at RIKEN Nishina Center, Japan has proved its magicity by measuring the excitation energy of the first excited state at 2.6 MeV, which is known to be high for doubly magic nuclei. The experiments also established the spins and parities of the excited states in ^{78}Ni nucleus using a two-proton knockout from ^{80}Zn [38]. Given the doubly-magic nature of the mother nucleus, its decay should be simple and can be used to benchmark shell-model calculations. There are only a few radioactive doubly-magic nuclei, such as ^{48}Ni (Z=28; N=20), ^{56}Ni (Z=28; N=28), ^{100}Sn (Z=50; N=50), and ^{132}Sn (Z=50; N=82). The decay properties vary among different isotopes of Ni. ^{48}Ni exhibits two-proton radioactivity and little is known about its β decay [72]. ^{56}Ni on the other hand is a long-lived isotope with a half-life of 6 days. The beta decay of ^{56}Ni populates only a single 1^+ state with a small *logft* value indicative of Gamow-Teller (GT) decay. ^{78}Ni bears a relatively large Q_β value of 10 MeV [73] and multiple 1^+ states can be populated. Because of the large Q_β value, ^{78}Ni is a unique neutron-rich doubly magic nucleus to probe the fundamentals of the beta decay. The doubly magic nature of ^{100}Sn makes it the best candidate for large-scale calculations to quantify the Gamow-Teller quenching problem [74]. In the decay of neutron-rich ^{132}Sn with $Q_\beta = 3$ MeV [75] only two 1^+ states are known to be populated in GT decay.

In ^{78}Ni (N=50), the Fermi Level neutron fills in the $1g_{g/2}$ orbital. The proton Fermi Level, on the other hand, is filled in the $1f_{7/2}$ orbital. The large asymmetry in the neutron-to-proton ratio will strongly affect decay properties for very neutron-rich nuclei. The general

form of beta-decay transitions as explained in the introduction section are of Gamow-Teller ($\Delta l = 0$) or First Forbidden ($\Delta l = 1$) transitions. The unoccupied states in the proton valence space above the Z=28 closure are $2p_{3/2}$, $1f_{7/2}$, $2p_{1/2}$, $1g_{9/2}$, and $1g_{7/2}$. It is therefore possible to convert neutrons to protons occupying just mentioned proton levels above Z=28 level. The resulting excited states will have high excitation energy and their population will be suppressed in the final β-decay intensity due to decreasing phase-space (see Figure 1.2 and Equation 1.15). The major contributors to the β-decay strength along with their type are listed in Table 6.1.

The goal of the experimental studies of ^{78}Ni is to provide the data which can be compared with nuclear model predictions. Within the shell model framework, the decay properties are sensitive to the single-particle energies and residual interactions. A reliable theoretical framework is essential to constrain energies of single-particle states contributing to the decay. For studying the decay of ^{78}Ni, a simplified approach was used by considering a hamiltonian in the absence of any residual interactions. This enables to illustrate schematically the dominant transitions using predictions for pure single-particle matrix elements. The formula for pure GT transition probability is given by Equation 6.1.

$$|M_{im}|^2 = |M^{i\rightarrow m}{}_{GT}|^2 = N_\nu \left[1 - \frac{N_\pi}{2j_\pi + 1}\right] . |M^0{}_{GT}|^2 \tag{6.1}$$

Here, N_ν and N_π denote neutron and proton occupancy, respectively. For a given orbital angular momentum l of a given state in the parent and the daughter nucleus, the matrix elements given in Equation 6.1 can be simplified as given in Table 6.2. In the table, $J_{i,f}$ are the total angular momentum states of the parent and the daughter nuclei and are related to the orbital angular momentum of the states as $J_{i,f} = l \pm 1/2$.

Figure 6.2 shows reduced transition probability calculated for the expected β-decay transitions. The calculations predict GT transitions leading to neutron-bound states in ^{78}Ni with the highest probability calculated for the $\nu 1f_{7/2} \longrightarrow \pi 1f_{5/2}$ transition. The transition originating from the N=50 shell belongs to the $\nu 1g_{9/2} \longrightarrow \pi 1g_{9/2}$, and is predicted at lower excitation energy compared to the one originating from the N=28 shell. The calculations are simplified and are not expected to capture the exact decay properties of the nucleus, but give

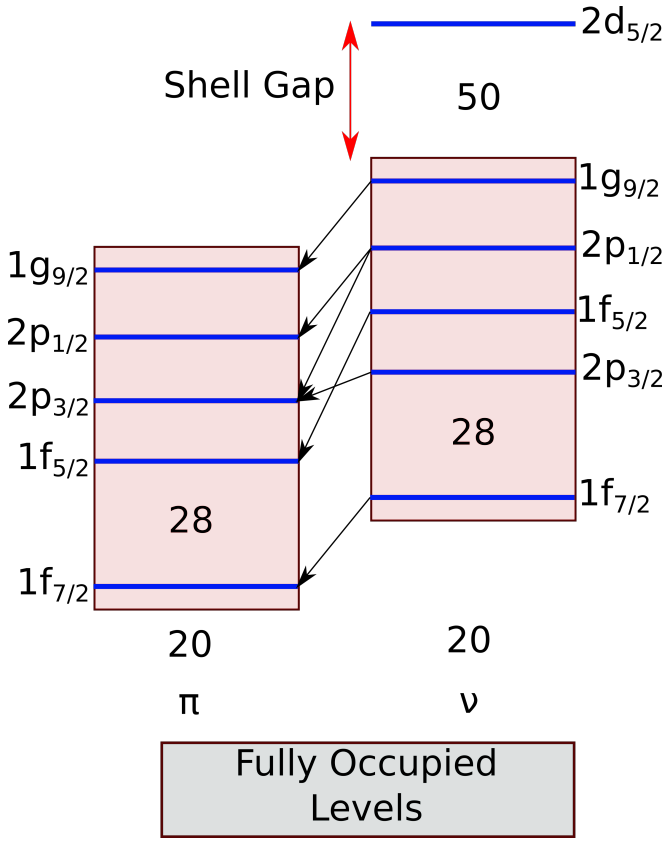


Figure 6.1: Model of beta decay of Cu isotopes in the shell-mdoel framework for N>50.

Table 6.1: β-decay neutron and proton spin-orbit partners in the decay of ^{78}Ni.

Sr.No.	β-decay Transition
1	$\nu 1p_{1/2} \longrightarrow \pi 1p_{1/2}$, $\nu 1p_{1/2} \longrightarrow \pi 1p_{3/2}$
2	$\nu 1f_{5/2} \longrightarrow \pi 1f_{5/2}$, $\nu 1f_{7/2} \longrightarrow \pi 1f_{5/2}$
3	$\nu 2p_{1/2} \longrightarrow \pi 2p_{1/2}$, $\nu 2p_{1/2} \longrightarrow \pi 2p_{3/2}$
4	$\nu 1g_{9/2} \longrightarrow \pi 1g_{9/2}$, $\nu 1g_{9/2} \longrightarrow \pi 1g_{7/2}$

Table 6.2: GT probability ($|M^0_{GT}|^2$) using single particle states.

	$l+\frac{1}{2}$	$l-\frac{1}{2}$
$l+\frac{1}{2}$	$\frac{2l+3}{2l+1}$	$\frac{4(l+1)}{2l+1}$
$l-\frac{1}{2}$	$\frac{4l}{2l+1}$	$\frac{2l-1}{2l+1}$

a starting point to see what states contribute to the beta-strength. To get a more precise look into the decay, it is imperative to include the residual interactions and configuration mixing into the model.

A shell model code called NuShellX code was used to perform the calculations [45] which take into account configuration mixing effects, which are due to effective residual interactions. The obtained beta-strength function for the decay is compared to shell-model calculations using various choices of interactions. The NuShellX code first predicts the states in the mother and the daughter nucleus. The GT transition matrix elements are calculated between the parent ground state and daughter excited states, which fulfill GT selection rules. To assess the decay of ^{78}Ni, shell-model calculations are performed using $f_{7/2}pg_{9/2}$ model space with ^{40}Ca core using *fpgpn* interactions. The calculated single-particle energies of the neutron and proton states are listed in Table 6.3.

The neutron-proton spin-orbit partners contributing to the beta decay of ^{78}Ni are shown in Table 6.5. The configurations represent a neutron-hole state coupled to a proton single-particle state in ^{78}Cu. Out of all the combinations $\nu {p_{3/2}}^{-1} \otimes \pi {p_{3/2}}^{+1}$, $\nu {p_{1/2}}^{-1} \otimes \pi {p_{3/2}}^{+1}$, $\nu {f_{5/2}}^{-1} \otimes \pi {f_{5/2}}^{+1}$, $\nu {f_{7/2}}^{-1} \otimes \pi {f_{5/2}}^{+1}$, and $\nu {g_{9/2}}^{-1} \otimes \pi {g_{9/2}}^{+1}$ represent the dominant configuration of 1^+ states populated in Gamow-Teller transitions. Figure 6.3 shows the shell-model calculations using *fpgpn* interactions for the decay of ^{78}Ni decay. The contributions from the neutron-proton configuration mixing in ^{78}Cu to the β-decay strength are labeled in the middle section of the Figure 6.3. As per the predictions, $\nu {p_{3/2}}^{-1} \otimes \pi {f_{f/2}}^{+1}$, $\nu {p_{1/2}}^{-1} \otimes \pi {p_{3/2}}^{+1}$, and $\nu {p_{1/2}}^{-1} \otimes \pi {p_{1/2}}^{+1}$ which represent transitions from $29 \leq N \leq 40$ lead to beta-strength to states which are bound with respect to neutron emission. The rest of the transitions lead to states above the neutron-separation energy.

The decay of N=50 nucleus, ^{79}Cu is expected to bear resemblance to ^{78}Ni. The shell model calculations are able to capture the effect of the proton outside of the Z=28 closed shell. For the case of ^{79}Cu, the calculations were performed using an $f_{7/2}pg_{9/2}$ model space with a ^{40}Ca core using the *fpgpn* [76] interactions. The calculations use single-particle state energy distribution in both the proton and the neutron space. Figure 6.5 shows the outcome of the calculation for the decay of ^{79}Cu using these *fpgpn* interactions. Because the ground state of ^{79}Cu has spin and parity $J_\pi = 5/2^-$, the states that can be populated in the daughter

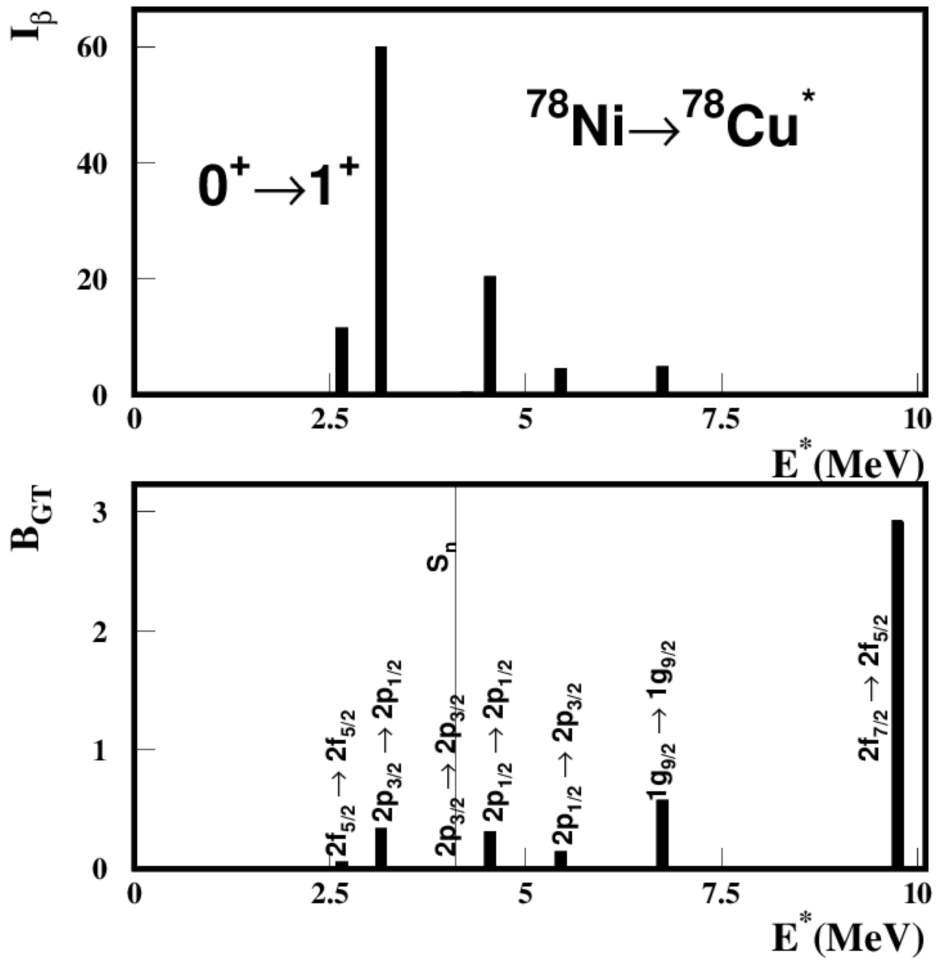


Figure 6.2: Shell-model calculations for the decay of ^{78}Ni in the absence of any residual interaction component to the nuclear potential. The top panel shows the beta-decay feeding intensities for the predicted transitions and and the lower panel shows the reduced transition probability amplitude for those transitions.

Table 6.3: Neutron and proton single-particle energy states used in calculations with *fpgpn* interaction for ^{78}Ni

Sr.No.	Proton(π)	Energy (MeV)	Neutron(ν)	Energy (MeV)
1	$0f_{7/2}$	-8.955	$0f_{7/2}$	-4.624
2	$1p_{3/2}$	-6.044	$1p_{3/2}$	-2.679
3	$0f_{5/2}$	-1.683	$0f_{5/2}$	2.617
4	$1p_{1/2}$	-5.544	$1p_{1/2}$	-1.137
5	$0g_{9/2}$	0	$0g_{9/2}$	2.4
6	$0g_{7/2}$	6	$0g_{7/2}$	8.9

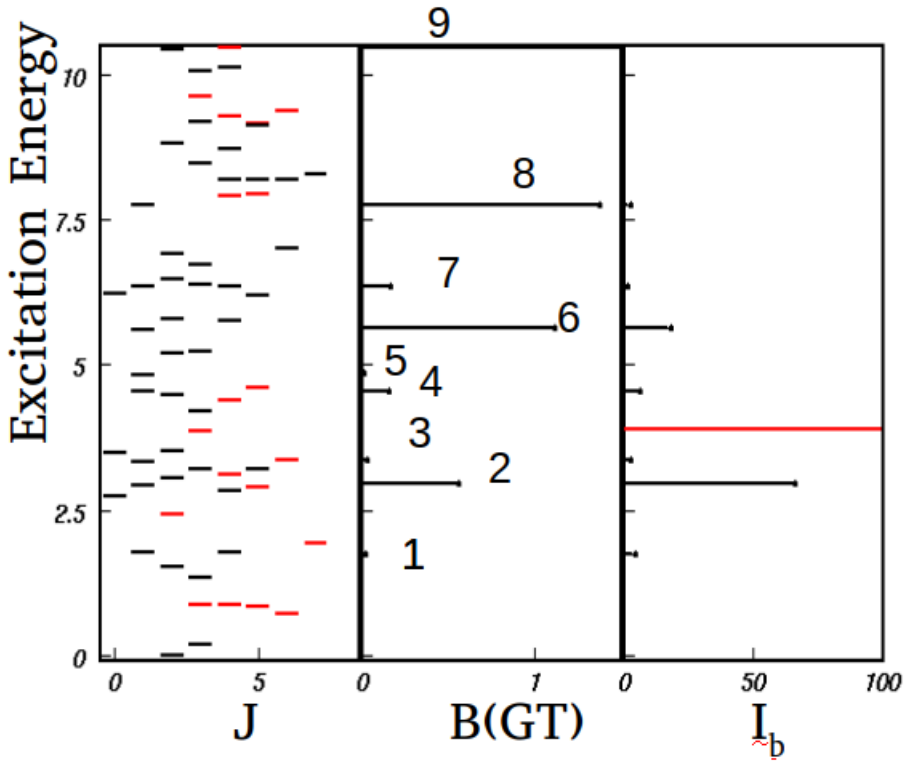


Figure 6.3: Shell-model calculations for the decay of ^{78}Ni using the *fpgpn* interactions.

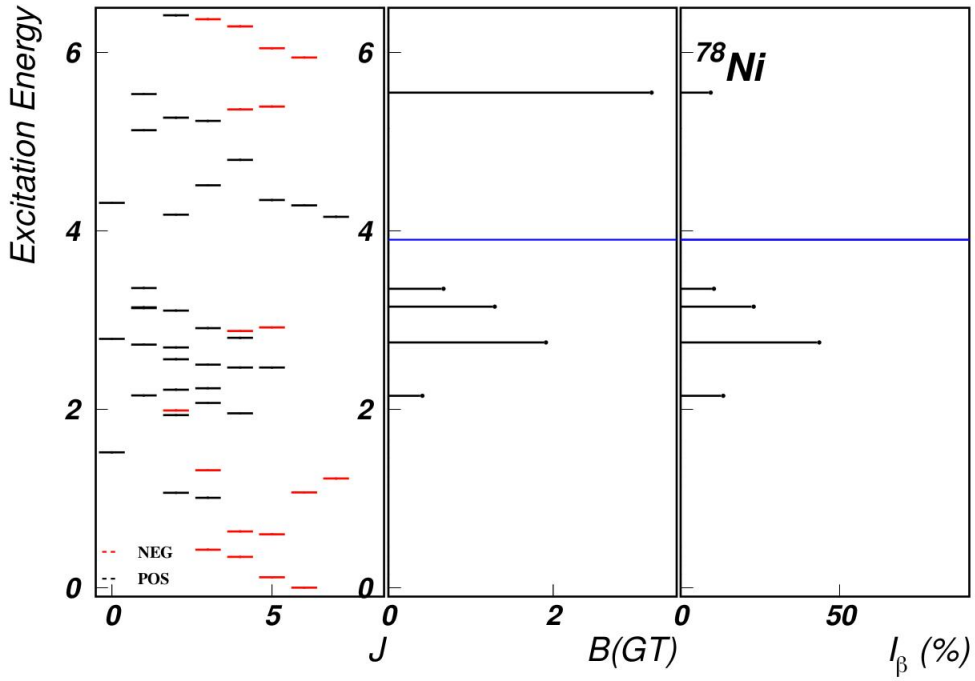


Figure 6.4: Shell-model calculations for the decay of ^{78}Ni using the *jj44bpn* interactions.

nucleus ^{79}Zn are $(3/2)^-$, $(5/2)^-$, and $(7/2)^-$ to satisfy GT selection rules. Reduced beta-decay probability is also calculated as shown in Figure 6.5. Shell-model calculations were also performed using *jj44bpn* [76] interactions with $f_{5/2}pg_{9/2}$ model space with ^{56}Ni core. The results from the calculations are shown in Figure 6.6. The predictions of the two interactions show different strength distribution. The *fpgpn* predicts a sparse amount of strength below the neutron-separation energy (S_n) of ^{79}Zn with some accumulation of strength around 8 MeV and 6 MeV excitation energy. The strength close to S_n leads to intense β-decay feeding. On the other hand, the calculations with the *jj44bpn* interactions predict a larger fraction of the total strength below S_n. Above S_n, the strength is more fragmented with a peak-like structure around 7 and 10 MeV.

Figure 6.7 shows the comparison of the calculations and the results from the experiment. The experimental data are better matched to the shell-model calculations performed using the *fpgpn* interactions. The predictions overestimate the strength in the region of excitation energy from S_n to around 5.5 MeV. Figure 6.8 shows the cumulative B(GT) obtained in the decay of ^{78}Ni and ^{79}Cu. The major contributors in the decay of both the nuclei appear to be similar as seen through the jumps in the strength at various excitation energy levels.

Moving to the decay of Cu isotopes with neutrons above the N=50 shell gap. Figure 6.1 shows possible neutron and proton spin partners active in GT decays with the presence of the extra neutrons in the $d_{5/2}$ shell. The figure shows schematically the role of dominant GT transitions. The transitions involving neutrons in the $d_{5/2}$ to proton states above the Z=28 shell closure represent FF decays, which have much smaller amplitude compared to GT decays. This plot illustrates how the decays of N>50 nuclei are affected by the presence of the N=50 shell gap. Their strength distribution is expected to be shifted to higher excitation energy compared to ^{79}Cu by about the size of the N=50 shell gap.

For analyzing the decay of ^{81,80}Cu it is necessary to expand the shell-model space to include the occupation of the extra neutrons above the N=50 occupancy in the $d_{5/2}$ shell. The outcome of shell-model calculations for the decay of ^{81}Cu is shown in Figure 6.9. The shell model predicts a population of the daughter nucleus ^{81}Zn with angular momentum $(3/2)^-$, $(5/2)^-$, and $(7/2)^-$. The beta-strength is predicted to be above S_n of ^{81}Zn. The shift in the strength to higher excitation energy is attributed to the N=50 shell gap. The

Table 6.4: Neutron and proton single-particle energy states using Shell model used in calculations with *jj44bpn* interaction.

Sr.No.	Proton(π)	Energy (MeV)	Neutron(ν)	Energy (MeV)
1	$0f_{5/2}$	-9.286	$0f_{5/2}$	-9.286
2	$1p_{3/2}$	-9.657	$1p_{3/2}$	-9.657
3	$1p_{1/2}$	-8.269	$1p_{1/2}$	-8.269
4	$0g_{9/2}$	-5.894	$0g_{9/2}$	-5.894

Table 6.5: The configurations in the daughter nucleus after the beta-decay of ^{78}Ni to ^{78}Cu.

Sr. No.	Configuration
1	$\nu {p_{3/2}}^{-1} \otimes \pi {f_{5/2}}^{+1}$
2	$\nu {p_{1/2}}^{-1} \otimes \pi {p_{3/2}}^{+1}$
3	$\nu {p_{1/2}}^{-1} \otimes \pi {p_{1/2}}^{+1}$
4	$\nu {f_{5/2}}^{-1} \otimes \pi {p_{5/2}}^{+1}$
5	$\nu {p_{3/2}}^{-1} \otimes \pi {p_{3/2}}^{+1}$
6	$\nu {p_{3/2}}^{-1} \otimes \pi {p_{1/2}}^{+1}$
7	$\nu {f_{5/2}}^{-1} \otimes \pi {p_{3/2}}^{+1}$
8	$\nu {f_{7/2}}^{-1} \otimes \pi {f_{5/2}}^{+1}$
9	$\nu {g_{9/2}}^{-1} \otimes \pi {g_{9/2}}^{+1}$

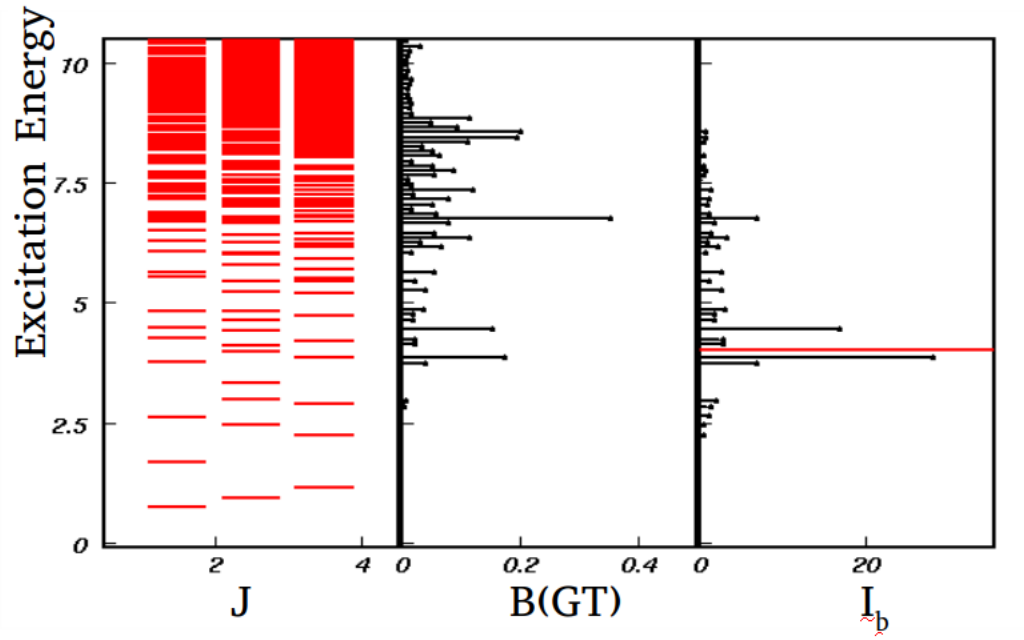


Figure 6.5: Shell-model calculations performed for the decay of ^{79}Cu using *fpgpn* interactions.

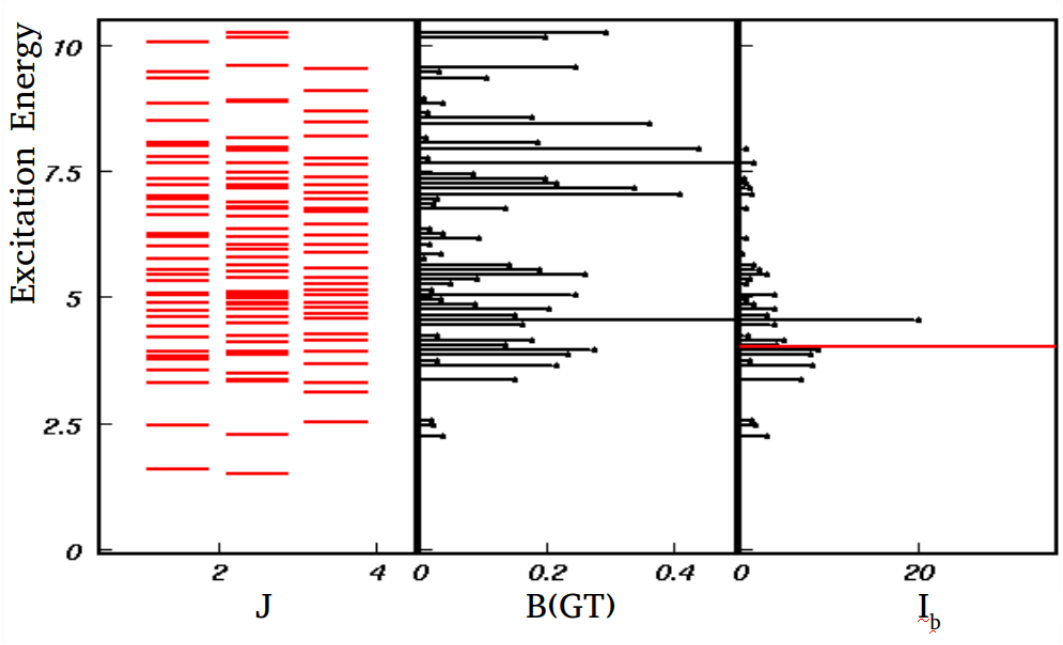


Figure 6.6: Shell-model calculations performed for the decay of ^{79}Cu using *jj44bpn* interactions.

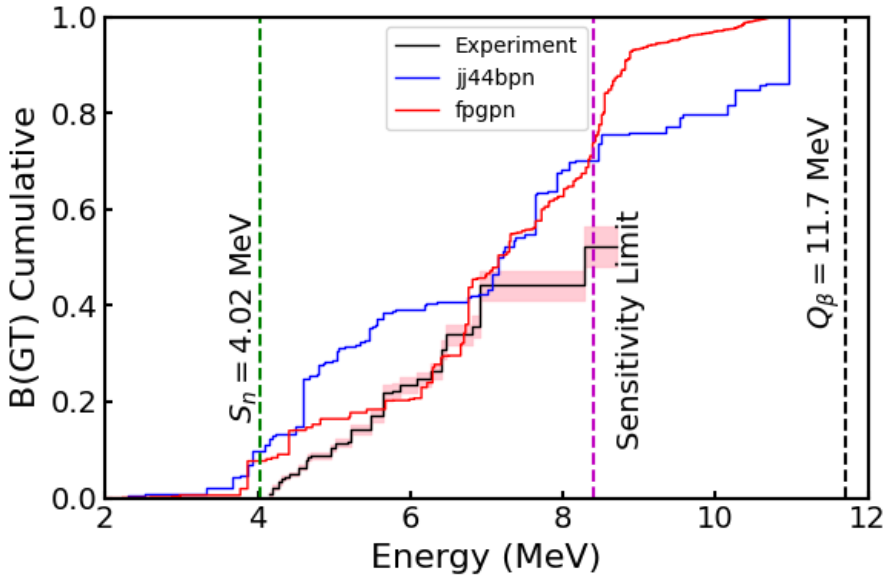


Figure 6.7: Comparison of cumulative BGT from the experiment and the ones obtained from the shell-model calculations using *fpgpn* and *jj44bpn* interactions.

decay of the nucleus is similar to the decay of ^{79}Cu, but with more configurations due to the presence of two extra neutrons in the $d_{5/2}$ shell, and strength at higher excitation energy which is also seen from the results calculated from the experiment.

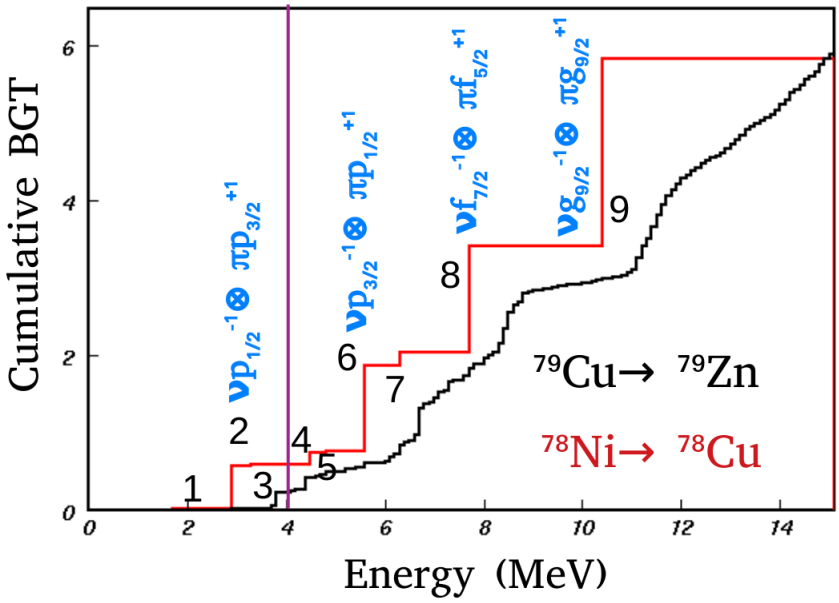


Figure 6.8: Comparison of cumulative strength distribution of ^{78}Ni and ^{79}Cu using *fpgpn* interactions. The major contributors are shown.

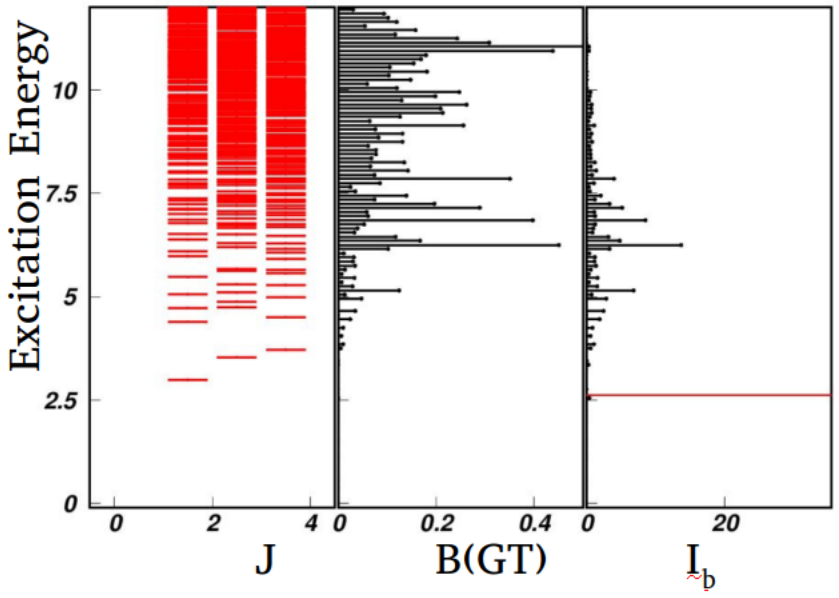


Figure 6.9: Shell-model calculations for the decay of ^{81}Cu.

Chapter 7

Conclusion

The study presented in the dissertation aims to provide a detailed account of the decay of neutron-rich isotopes in the ^{78}Ni region ($26 \leq Z \leq 34$). Many isotopes in this region have a large $Q_\beta - S_n$ window leading to large β-delayed neutron-emission probabilities. To establish beta-strength for the decay of these nuclei the energy distribution of the delayed neutrons and subsequent gamma-rays has to be measured. For neutron detection VANDLE array provides capability for the measurements using the time-of-flight technique. To study the decay of these nuclei, experiments were performed at the RIBF facility at RIKEN Nishina Center, Japan. The facility provides a multi-species neutron-rich beam with the best rates in the world, presently.

To exploit the neutron-detection properties of the VANDLE array, it is important to pair it with a fast trigger detector that can provide a start of the neutron time-of-flight measurement. A YSO-based segmented implant detector was developed at the University of Tennessee, Knoxville for such measurements. The detector provides a sub-nanosecond timing resolution with the capability of pixelization in the images of the implanted ions and the corresponding beta-decay, crucial for ion-beta correlations. The commissioning experiment for the detector was performed at RIBF alongside BRIKEN neutron counter. The detector yielded a very high β-detection efficiency of ~ 80 %. A variant of the detector was used in coordination with the VANDLE array for spectroscopy of the β-delayed neutrons emitted from the radioactive nuclei in the ^{78}Ni region. Estimates of the quenching to the light produced by ions in the ^{78}Ni region are also extracted in this work. The quenching factor is

an important piece of information that is needed for the planning of experiments with this detector in various regions of the chart of nuclei.

In this dissertation, the first-ever measurement of the beta-strength function of N$\geq$ 50 Cu isotopes is reported. The decay strength distribution of ^{79}Cu with N=50 and just one proton above the Z=28 resembles that of the decay of ^{78}Ni. The beta-strength distribution obtained from the experiment for ^{79}Cu was compared to shell-model calculations using various interactions. The data matches better with shell model calculations performed with *fpgpn* interactions which predicts a larger energy spread of the ^{78}Ni beta-strength. And a large portion of beta-decay feeding in ^{78}Ni decay is to high-density states, requiring Modular Total Absorption Spectroscopy (MTAS) [77] to measure γ-ray excitation from these levels.

This work also contains the first measurement of beta-strength to neutron-unbound states for ^{80,81}Cu with N>50. The obtained beta-strength of these nuclei is at much higher excitation energy compared to ^{79}Cu. The strength distribution extracted from the data is still ambiguous due to the absence of coincidences between β-delayed neutrons and the gamma-ray emissions in ^{79,80}Zn. However, in the case of ^{81}Cu a strong population seen in data of $2^+ \rightarrow 0^+$ and $4^+ \rightarrow 2^+$ transitions in ^{80}Zn was observed, which is indicative that neutron emission proceeds through the excited states in ^{80}Zn. This is also supported by calculations using a statistical model of neutron emission [78]. The situation is more complex in the case of ^{80}Cu due to the presence of an isomeric state in ^{79}Zn. The decay of these nuclei is determined by the GT decays of the ^{78}Ni core. A similar scenario is demonstrated by Madurga *et al.*, [8] where the decay of ^{83,84}Ga (Z=31) is discussed. However, in the case of $^{79-81}$Cu (Z=29) fewer protons result in simpler configurations, enabling a closer comparison to ^{78}Ni decay itself. The shift in the strength distribution of ^{80,81}Cu is attributed to the presence of the N=50 shell gap between the $g_{9/2}$ and $d_{5/2}$ shells.

The results presented in the dissertation provide information on the decay properties of nuclei taking part in the r-process, especially for Cu isotopes with N$\geq$50. The data about the decay properties of these nuclei is challenging to obtain due to the limitations of the beamline facilities to achieve high rates of these exotic isotopes. In order to measure the strength distribution with better energy resolution, it is important to implement neutron detectors with better energy resolution. The development of detectors arrays such as NEXT [79, 80]

will aid such measurements. The implantation detector technology will be implemented at FRIB for decay experiments.

Bibliography

[1] R. B. Roberts, L. R. Hafstad, R. C. Meyer, and P. Wang. The delayed neutron emission which accompanies fission of uranium and thorium. *Phys. Rev.*, 55:664–664, Apr 1939. 1

[2] Paraskevi Dimitriou Iris Dillman and Balraj Singh. Summary report of 1st research coordination meeting on development of reference database for beta-delayed neutron emission. *IAEA Report INDC(NDS)*, 2014. 2

[3] P. Mller, M.R. Mumpower, T. Kawano, and W.D. Myers. Nuclear properties for astrophysical and radioactive-ion-beam applications (ii). *Atomic Data and Nuclear Data Tables*, 125:1 – 192, 2019. 2

[4] R. Yokoyama, R. Grzywacz, B. C. Rasco, N. Brewer, K. P. Rykaczewski, I. Dillmann, J. L. Tain, S. Nishimura, D. S. Ahn, A. Algora, J. M. Allmond, J. Agramunt, H. Baba, S. Bae, C. G. Bruno, R. Caballero-Folch, F. Calvino, P. J. Coleman-Smith, G. Cortes, T. Davinson, C. Domingo-Pardo, A. Estrade, N. Fukuda, S. Go, C. J. Griffin, J. Ha, O. Hall, L. J. Harkness-Brennan, J. Heideman, T. Isobe, D. Kahl, M. Karny, T. Kawano, L. H. Khiem, T. T. King, G. G. Kiss, A. Korgul, S. Kubono, M. Labiche, I. Lazarus, J. Liang, J. Liu, G. Lorusso, M. Madurga, K. Matsui, K. Miernik, F. Montes, A. I. Morales, P. Morrall, N. Nepal, R. D. Page, V. H. Phong, M. Piersa, M. Prydderch, V. F. E. Pucknell, M. M. Rajabali, B. Rubio, Y. Saito, H. Sakurai, Y. Shimizu, J. Simpson, M. Singh, D. W. Stracener, T. Sumikama, R. Surman, H. Suzuki, H. Takeda, A. Tarifeño Saldivia, S. L. Thomas, A. Tolosa-Delgado, M. Woli ńska Cichocka, P. J. Woods, and X. X. Xu. Strong one-neutron emission from two-neutron unbound states in β decays of the r-process nuclei ^{86,87}Ga. *Phys. Rev. C*, 100:031302, Sep 2019. 2, 4

[5] K. Miernik, K. P. Rykaczewski, C. J. Gross, R. Grzywacz, M. Madurga, D. Miller, J. C. Batchelder, I. N. Borzov, N. T. Brewer, C. Jost, A. Korgul, C. Mazzocchi, A. J. Mendez, Y. Liu, S. V. Paulauskas, D. W. Stracener, J. A. Winger, M. Woli ńska Cichocka, and E. F. Zganjar. Large β-delayed one and two neutron emission rates in the decay of ^{86}Ga. *Phys. Rev. Lett.*, 111:132502, Sep 2013. 2

[6] R. Caballero-Folch, I. Dillmann, J. Agramunt, J. L. Taín, A. Algora, J. Äystö, F. Calviño, L. Canete, G. Cortès, C. Domingo-Pardo, T. Eronen, E. Ganioglu, W. Gelletly, D. Gorelov, V. Guadilla, J. Hakala, A. Jokinen, A. Kankainen, V. Kolhinen, J. Koponen, M. Marta, E. Mendoza, A. Montaner-Pizá, I. Moore, C. R. Nobs, S. E. A. Orrigo, H. Penttilä, I. Pohjalainen, J. Reinikainen, A. Riego, S. Rinta-Antila, B. Rubio, P. Salvador-Castiñeira, V. Simutkin, A. Tarifeño Saldivia, A. Tolosa-Delgado, and A. Voss. First determination of β-delayed multiple neutron emission beyond $a = 100$ through direct neutron measurement: The P_{2n} value of ^{136}Sb. *Phys. Rev. C*, 98:034310, Sep 2018. 2

[7] M. Piersa-Siłkowska, A. Korgul, J. Benito, L. M. Fraile, E. Adamska, A. N. Andreyev, R. Álvarez-Rodríguez, A. E. Barzakh, G. Benzoni, T. Berry, M. J. G. Borge, M. Carmona, K. Chrysalidis, J. G. Correia, C. Costache, J. G. Cubiss, T. Day Goodacre, H. De Witte, D. V. Fedorov, V. N. Fedosseev, G. Fernández-Martínez, A. Fijałkowska, H. Fynbo, D. Galaviz, P. Galve, M. García-Díez, P. T. Greenlees, R. Grzywacz, L. J. Harkness-Brennan, C. Henrich, M. Huyse, P. Ibáñez, A. Illana, Z. Janas, K. Johnston, J. Jolie, D. S. Judson, V. Karanyonchev, M. Kici ńska Habior, J. Konki, Ł. Koszuk, J. Kurcewicz, I. Lazarus, R. Lică, A. López-Montes, H. Mach, M. Madurga, I. Marroquín, B. Marsh, M. C. Martínez, C. Mazzocchi, K. Miernik, C. Mihai, N. Mărginean, R. Mărginean, A. Negret, E. Nácher, J. Ojala, B. Olaizola, R. D. Page, J. Pakarinen, S. Pascu, S. V. Paulauskas, A. Perea, V. Pucknell, P. Rahkila, C. Raison, E. Rapisarda, K. Rezynkina, F. Rotaru, S. Rothe, K. P. Rykaczewski, J.-M. Régis, K. Schomacker, M. Siłkowski, G. Simpson, C. Sotty, L. Stan, M. Stănoiu, M. Stryjczyk, D. Sánchez-Parcerisa, V. Sánchez-Tembleque, O. Tengblad, A. Turturică, J. M. Udías, P. Van Duppen, V. Vedia, A. Villa, S. Viñals, R. Wadsworth, W. B. Walters, N. Warr, and S. G. Wilkins. First β-decay spectroscopy of ^{135}In and new β-decay branches of ^{134}In. *Phys. Rev. C*, 104:044328, Oct 2021. 2

[8] M. Madurga, S. V. Paulauskas, R. Grzywacz, D. Miller, D. W. Bardayan, J. C. Batchelder, N. T. Brewer, J. A. Cizewski, A. Fijałkowska, C. J. Gross, M. E. Howard, S. V. Ilyushkin, B. Manning, M. Matoš, A. J. Mendez, K. Miernik, S. W. Padgett,

W. A. Peters, B. C. Rasco, A. Ratkiewicz, K. P. Rykaczewski, D. W. Stracener, E. H. Wang, M. Woli ńska Cichocka, and E. F. Zganjar. Evidence for gamow-teller decay of ^{78}Ni core from beta-delayed neutron emission studies. *Phys. Rev. Lett.*, 117:092502, Aug 2016. 4, 24, 138

[9] W.A. Peters, S. Ilyushkin, M. Madurga, C. Matei, S.V. Paulauskas, R.K. Grzywacz, D.W. Bardayan, C.R. Brune, J. Allen, J.M. Allen, Z. Bergstrom, J. Blackmon, N.T. Brewer, J.A. Cizewski, P. Copp, M.E. Howard, R. Ikeyama, R.L. Kozub, B. Manning, T.N. Massey, M. Matos, E. Merino, P.D. O'Malley, F. Raiola, C.S. Reingold, F. Sarazin, I. Spassova, S. Taylor, and D. Walter. Performance of the versatile array of neutron detectors at low energy (vandle). *Nuclear Instruments and Methods in Physics Research Section A: Accelerators, Spectrometers, Detectors and Associated Equipment*, 836:122 – 133, 2016. 4, 36, 37, 55, 57

[10] E. Margaret Burbidge, G. R. Burbidge, William A. Fowler, and F. Hoyle. Synthesis of the elements in stars. *Rev. Mod. Phys.*, 29:547–650, Oct 1957. 4

[11] E. Margaret Burbidge, G. R. Burbidge, William A. Fowler, and F. Hoyle. Synthesis of the elements in stars. *Rev. Mod. Phys.*, 29:547–650, Oct 1957. 5, 12

[12] Ian U. Roederer, George W. Preston, Ian B. Thompson, Stephen A. Shectman, Christopher Sneden, Gregory S. Burley, and Daniel D. Kelson. A SEARCH FOR STARS OF VERY LOW METAL ABUNDANCE. VI. DETAILED ABUNDANCES OF 313 METAL-POOR STARS. *The Astronomical Journal*, 147(6):136, may 2014. 5

[13] Chen Ning Yang. Fermi's β-decay theory. *Asia Pacific Physics Newsletter*, 01(01):27–30, 2012. 6, 7

[14] C. L. Cowan, F. Reines, F. B. Harrison, H. W. Kruse, and A. D. McGuire. Detection of the free neutrino: a confirmation. *Science*, 124(3212):103–104, 1956. 6

[15] Bernd Pfeiffer, Karl-Ludwig Kratz, and Peter Mller. Status of delayed-neutron precursor data: half-lives and neutron emission probabilities. *Progress in Nuclear Energy*, 41(1):39 – 69, 2002. 11

[16] Martínez-Pinedo, G., Langanke, and K. Shell-model half-lives for $N = 82$ nuclei and their implications for the r process. *Phys. Rev. Lett.*, 83:4502–4505, Nov 1999. 11

[17] Peter Möller, Bernd Pfeiffer, and Karl-Ludwig Kratz. New calculations of gross β-decay properties for astrophysical applications: Speeding-up the classical r process. *Phys. Rev. C*, 67:055802, May 2003. 11

[18] Eugene Feenberg and George Trigg. The interpretation of comparative half-lives in the fermi theory of beta-decay. *Rev. Mod. Phys.*, 22:399–406, Oct 1950. 11

[19] M. R. Mumpower, T. Kawano, and P. Möller. Neutron-γ competition for β-delayed neutron emission. *Phys. Rev. C*, 94:064317, Dec 2016. 12, 13

[20] Reiner Krcken. Introduction to shell structure in exotic nuclei. *Contemporary Physics*, 52(2):101–120, 2011. 14

[21] B. P. Abbott et al. Gw170817: Observation of gravitational waves from a binary neutron star inspiral. *Phys. Rev. Lett.*, 119:161101, Oct 2017. 15

[22] H. A. Bethe and R. F. Bacher. Nuclear physics a. stationary states of nuclei. *Rev. Mod. Phys.*, 8:82–229, Apr 1936. 15, 19

[23] Fermi gas model, 2017. 16

[24] V. Zelevinsky and A. Volya. *Physics of Atomic Nuclei*. Wiley, 2017. 16

[25] Maria G. Mayer. On closed shells in nuclei. *Phys. Rev.*, 74:235–239, Aug 1948. 16

[26] Otto Haxel, J. Hans D. Jensen, and Hans E. Suess. On the "magic numbers" in nuclear structure. *Phys. Rev.*, 75:1766–1766, Jun 1949. 16

[27] Roger D. Woods and David S. Saxon. Diffuse surface optical model for nucleon-nuclei scattering. *Phys. Rev.*, 95:577–578, Jul 1954. 17

[28] N. Michel and M. Płoszajczak. *Gamow Shell Model: The Unified Theory of Nuclear Structure and Reactions*. Lecture Notes in Physics. Springer International Publishing, 2021. 18

[29] B. Pritychenko, M. Birch, B. Singh, and M. Horoi. Tables of e2 transition probabilities from the first 2+ states in eveneven nuclei. *Atomic Data and Nuclear Data Tables*, 107:1–139, 2016. 21

[30] T. Otsuka. Exotic nuclei and nuclear forces. *Physica Scripta*, 2013:014007, 2013. 20

[31] I. Stefanescu, G. Georgiev, D. L. Balabanski, N. Blasi, A. Blazhev, N. Bree, J. Cederkäll, T. E. Cocolios, T. Davinson, J. Diriken, J. Eberth, A. Ekström, D. Fedorov, V. N. Fedosseev, L. M. Fraile, S. Franchoo, K. Gladnishki, M. Huyse, O. Ivanov, V. Ivanov, J. Iwanicki, J. Jolie, T. Konstantinopoulos, Th. Kröll, R. Krücken, U. Köster, A. Lagoyannis, G. Lo Bianco, P. Maierbeck, B. A. Marsh, P. Napiorkowski, N. Patronis, D. Pauwels, G. Rainovski, P. Reiter, K. Riisager, M. Seliverstov, G. Sletten, J. Van de Walle, P. Van Duppen, D. Voulot, N. Warr, F. Wenander, and K. Wrzosek. Interplay between single-particle and collective effects in the odd-a cu isotopes beyond $n = 40$. *Phys. Rev. Lett.*, 100:112502, Mar 2008. 22

[32] J. M. Daugas, T. Faul, H. Grawe, M. Pfützner, R. Grzywacz, M. Lewitowicz, N. L. Achouri, J. C. Angélique, D. Baiborodin, R. Bentida, R. Béraud, C. Borcea, C. R. Bingham, W. N. Catford, A. Emsallem, G. de France, K. L. Grzywacz, R. C. Lemmon, M. J. Lopez Jimenez, F. de Oliveira Santos, P. H. Regan, K. Rykaczewski, J. E. Sauvestre, M. Sawicka, M. Stanoiu, K. Sieja, and F. Nowacki. Low-lying isomeric levels in ^{75}Cu. *Phys. Rev. C*, 81:034304, Mar 2010. 22

[33] K. T. Flanagan, P. Vingerhoets, M. Avgoulea, J. Billowes, M. L. Bissell, K. Blaum, B. Cheal, M. De Rydt, V. N. Fedosseev, D. H. Forest, Ch. Geppert, U. Köster, M. Kowalska, J. Krämer, K. L. Kratz, A. Krieger, E. Mané, B. A. Marsh, T. Materna, L. Mathieu, P. L. Molkanov, R. Neugart, G. Neyens, W. Nörtershäuser, M. D. Seliverstov, O. Serot, M. Schug, M. A. Sjoedin, J. R. Stone, N. J. Stone, H. H. Stroke, G. Tungate, D. T. Yordanov, and Yu. M. Volkov. Nuclear spins and magnetic moments of ^{71,73,75}Cu: Inversion of $\pi 2p_{3/2}$ and $\pi 1f_{5/2}$ levels in ^{75}Cu. *Phys. Rev. Lett.*, 103:142501, Oct 2009. 22

[34] S. Franchoo, M. Huyse, K. Kruglov, Y. Kudryavtsev, W. F. Mueller, R. Raabe, I. Reusen, P. Van Duppen, J. Van Roosbroeck, L. Vermeeren, A. Wöhr, K.-L. Kratz, B. Pfeiffer, and W. B. Walters. Beta decay of $^{68--74}$Ni and level structure of neutron-rich cu isotopes. *Phys. Rev. Lett.*, 81:3100–3103, Oct 1998. 22

[35] C. Santamaria, C. Louchart, A. Obertelli, V. Werner, P. Doornenbal, F. Nowacki, G. Authelet, H. Baba, D. Calvet, F. Château, A. Corsi, A. Delbart, J.-M. Gheller, A. Gillibert, T. Isobe, V. Lapoux, M. Matsushita, S. Momiyama, T. Motobayashi, M. Niikura, H. Otsu, C. Péron, A. Peyaud, E. C. Pollacco, J.-Y. Roussé, H. Sakurai, M. Sasano, Y. Shiga, S. Takeuchi, R. Taniuchi, T. Uesaka, H. Wang, K. Yoneda, F. Browne, L. X. Chung, Zs. Dombradi, S. Franchoo, F. Giacoppo, A. Gottardo, K. Hadynska-Klek, Z. Korkulu, S. Koyama, Y. Kubota, J. Lee, M. Lettmann, R. Lozeva, K. Matsui, T. Miyazaki, S. Nishimura, L. Olivier, S. Ota, Z. Patel, N. Pietralla, E. Sahin, C. Shand, P.-A. Söderström, I. Stefan, D. Steppenbeck, T. Sumikama, D. Suzuki, Zs. Vajta, J. Wu, and Z. Xu. Extension of the $n = 40$ island of inversion towards $n = 50$: Spectroscopy of ^{66}Cr, ^{70,72}Fe. *Phys. Rev. Lett.*, 115:192501, Nov 2015. 22

[36] F. Nowacki, A. Poves, E. Caurier, and B. Bounthong. Shape coexistence in ^{78}Ni as the portal to the fifth island of inversion. *Phys. Rev. Lett.*, 117:272501, Dec 2016. 22

[37] L. Olivier, S. Franchoo, M. Niikura, Z. Vajta, D. Sohler, and Doornenbal. Persistence of the $z = 28$ shell gap around ^{78}Ni: First spectroscopy of ^{79}Cu. *Phys. Rev. Lett.*, 119:192501, Nov 2017. 22

[38] R. Taniuchi, C. Santamaria, P. Doornenbal, A. Obertelli, K. Yoneda, G. Authelet, H. Baba, D. Calvet, F. Château, A. Corsi, A. Delbart, J. Gheller, A. Gillibert, J. Holt, T. Isobe, V. Lapoux, M. Matsushita, J. Menendez, S. Momiyama, T. Motobayashi, M. Niikura, F. Nowacki, K. Ogata, H. Otsu, T. Otsuka, C. Péron, S. Péru, A. Peyaud, E. Pollacco, A. Poves, J. Roussé, H. Sakurai, A. Schwenk, Y. Shiga, J. Simonis, Steven Ragnar Stroberg, S. Takeuchi, Y. Tsunoda, T. Uesaka, H. Wang, F. Browne, L. X. Chung, Z. Dombrádi, S. Franchoo, F. Giacoppo, A. Gottardo, K. Hadyska-Klk, Z. Korkulu, S. Koyama, Y. Kubota, J. Lee, M. Lettmann, C. Louchart, R. Lozeva,

K. Matsui, T. Miyazaki, S. Nishimura, L. Olivier, S. Ota, Z. Patel, E. ahin, C. Shand, P. Söderström, I. Stefan, D. Steppenbeck, T. Sumikama, D. Suzuki, Z. Vajta, V. Werner, J. Wu, and Z. Xu. 78ni revealed as a doubly magic stronghold against nuclear deformation. *Nature*, 569:53–58, 2019. 22, 126

[39] S. Franchoo, M. Huyse, K. Kruglov, Y. Kudryavtsev, W. F. Mueller, R. Raabe, I. Reusen, P. Van Duppen, J. Van Roosbroeck, L. Vermeeren, A. Wöhr, K.-L. Kratz, B. Pfeiffer, and W. B. Walters. Beta decay of $^{68--74}$Ni and level structure of neutron-rich cu isotopes. *Phys. Rev. Lett.*, 81:3100–3103, Oct 1998. 23

[40] K. T. Flanagan, P. Vingerhoets, M. Avgoulea, J. Billowes, M. L. Bissell, K. Blaum, B. Cheal, M. De Rydt, V. N. Fedosseev, D. H. Forest, Ch. Geppert, U. Köster, M. Kowalska, J. Krämer, K. L. Kratz, A. Krieger, E. Mané, B. A. Marsh, T. Materna, L. Mathieu, P. L. Molkanov, R. Neugart, G. Neyens, W. Nörtershäuser, M. D. Seliverstov, O. Serot, M. Schug, M. A. Sjoedin, J. R. Stone, N. J. Stone, H. H. Stroke, G. Tungate, D. T. Yordanov, and Yu. M. Volkov. Nuclear spins and magnetic moments of ^{71,73,75}Cu: Inversion of $\pi 2p_{3/2}$ and $\pi 1f_{5/2}$ levels in ^{75}Cu. *Phys. Rev. Lett.*, 103:142501, Oct 2009. 23

[41] B. Zeidman and J. A. Nolen. Mass and low-lying energy levels of ^{69}Cu. *Phys. Rev. C*, 18:2122–2126, Nov 1978. 23

[42] E. Sahin, F. L. Bello Garrote, Y. Tsunoda, T. Otsuka, G. de Angelis, A. Görgen, M. Niikura, S. Nishimura, Z. Y. Xu, H. Baba, F. Browne, M.-C. Delattre, P. Doornenbal, S. Franchoo, G. Gey, K. Hadyńska-Klęk, T. Isobe, P. R. John, H. S. Jung, I. Kojouharov, T. Kubo, N. Kurz, Z. Li, G. Lorusso, I. Matea, K. Matsui, D. Mengoni, P. Morfouace, D. R. Napoli, F. Naqvi, H. Nishibata, A. Odahara, H. Sakurai, H. Schaffner, P.-A. Söderström, D. Sohler, I. G. Stefan, T. Sumikama, D. Suzuki, R. Taniuchi, J. Taprogge, Z. Vajta, H. Watanabe, V. Werner, J. Wu, A. Yagi, M. Yalcinkaya, and K. Yoshinaga. Shell evolution towards ^{78}Ni: Low-lying states in ^{77}Cu. *Phys. Rev. Lett.*, 118:242502, Jun 2017. 23

[43] U. Köster, N. J. Stone, K. T. Flanagan, J. Rikovska Stone, V. N. Fedosseev, K. L. Kratz, B. A. Marsh, T. Materna, L. Mathieu, P. L. Molkanov, M. D. Seliverstov, O. Serot, A. M. Sjödin, and Yu. M. Volkov. In-source laser spectroscopy of ^{75,77,78}cu: Direct evidence for a change in the quasiparticle energy sequence in ^{75,77}cu and an absence of longer-lived isomers in ^{78}cu. *Phys. Rev. C*, 84:034320, Sep 2011. 23

[44] C. Petrone, J. M. Daugas, G. S. Simpson, M. Stanoiu, C. Plaisir, T. Faul, C. Borcea, R. Borcea, L. Cáceres, S. Calinescu, R. Chevrier, L. Gaudefroy, G. Georgiev, G. Gey, O. Kamalou, F. Negoita, F. Rotaru, O. Sorlin, and J. C. Thomas. Nearly degenerate isomeric states of ^{75}Cu. *Phys. Rev. C*, 94:024319, Aug 2016. 23

[45] B.A. Brown and W.D.M. Rae. The shell-model code nushellx@msu. *Nuclear Data Sheets*, 120:115–118, 2014. 24, 27, 129

[46] M Leone, N Robotti, and G Verna. rutherfords experiment on alpha particles scattering: the experiment that never was. *Physics Education*, 53(3):035003, 2018. 28

[47] William R Leo. *Techniques for Nuclear and Particle Physics Experiments : A How-to Approach*. Second revised edition.. edition, 1994. 29

[48] J.B. Birks, D.W. Fry, L. Costrell, and K. Kandiah. *The Theory and Practice of Scintillation Counting: International Series of Monographs in Electronics and Instrumentation*. International series of monographs on electronics and instrumentation. Elsevier Science, 2013. 31

[49] AIDA Collaboration. *Technical Report For the Design, Construction and Commissioning of the Advanced Implantation Detector Array (AIDA)*, 2018 (accessed December 4, 2018). http://www2.ph.ed.ac.uk/~td/AIDA/Design/tdr_aida.pdf. 32

[50] S. Nishimura, G. Lorusso, Z. Xu, J. Wu, R. Gernh, H. S. Jung, Y. K. Kwon, Z. Li, K. Steiger, and H. Sakurai. *RIKEN Accelerator Progress Report*, 2013. 32

[51] X-Z lab. *YSO Scintillation Crystal*, 2018 (accessed November 8, 2018). https://www.x-zlab.com/product/yso-scintillation-crystal/. 33, 34

[52] A. Tarifeo-Saldivia, J.L. Tain, C. Domingo-Pardo, F. Calvio, G. Corts, V.H. Phong, A. Riego, J. Agramunt, A. Algora, N. Brewer, R. Caballero-Folch, P.J. Coleman-Smith, T. Davinson, I. Dillmann, A. Estrad, C.J. Griffin, R. Grzywacz, L.J. Harkness-Brennan, G.G. Kiss, M. Kogimtzis, M. Labiche, I.H. Lazarus, G. Lorusso, K. Matsui, K. Miernik, F. Montes, A.I. Morales, S. Nishimura, R.D. Page, Z.S. Podolyk, V.F.E. Pucknell, B.C. Rasco, P. Regan, B. Rubio, K.P. Rykaczewski, Y. Saito, H. Sakurai, J. Simpson, E. Sokol, R. Surman, A. Svirkhin, S.L. Thomas, A. Tolosa, and P. Woods. Conceptual design of a hybrid neutron-gamma detector for study of β-delayed neutrons at the rib facility of riken. *Journal of Instrumentation*, 12(04):P04006, 2017. 33, 51

[53] Agile. *Agile Technologies Inc.*, 2022 (accessed April 20, 2022). https://http://www.agiletechnologies.net/. 39

[54] Joel S. Karp, Suleman Surti, Margaret E. Daube-Witherspoon, Richard Freifelder, Christopher A. Cardi, L Adam, Kilian Bilger, and Gerd Muehllehner. Performance of a brain pet camera based on anger-logic gadolinium oxyorthosilicate detectors. *Journal of nuclear medicine : official publication, Society of Nuclear Medicine*, 44 8:1340–9, 2003. 33

[55] Michigan State University. *LISE++: Exotic Beam Production*, 2018 (accessed December 4, 2018). http://lise.nscl.msu.edu/lise.html. 35

[56] National Institute of Standards and Technology. *ESTAR: stopping-power and range tables for electrons*, 2018 (accessed December 4, 2018). https://physics.nist.gov/PhysRefData/Star/Text/ESTAR.html. 36

[57] Osamu Kamigaito. *Accelerator-Overview*, 2018 (accessed November 8, 2018). http://www.nishina.riken.jp/RIBF/accelerator/overview.html. 50

[58] N. Fukuda, T. Kubo, T. Ohnishi, N. Inabe, H. Takeda, D. Kameda, and H. Suzuki. Identification and separation of radioactive isotope beams by the bigrips separator at the riken ri beam factory. *Nuclear Instruments and Methods in Physics Research Section B: Beam Interactions with Materials and Atoms*, 317:323 – 332, 2013. 52, 55, 73

[59] XIA. *Pixie-16*, 2018 (accessed December 4, 2018). https://www.xia.com/DGF_Pixie-16.html. 55

[60] R. Yokoyama, M. Singh, R. Grzywacz, A. Keeler, T.T. King, J. Agramunt, N.T. Brewer, S. Go, J. Heideman, J. Liu, S. Nishimura, P. Parkhurst, V.H. Phong, M.M. Rajabali, B.C. Rasco, K.P. Rykaczewski, D.W. Stracener, J.L. Tain, A. Tolosa-Delgado, K. Vaigneur, and M. Woliska-Cichocka. Segmented yso scintillation detectors as a new -implant detection tool for decay spectroscopy in fragmentation facilities. *Nuclear Instruments and Methods in Physics Research Section A: Accelerators, Spectrometers, Detectors and Associated Equipment*, 937:93–97, 2019. 65, 70

[61] J.E. Martin. *Physics for Radiation Protection: A Handbook*. Wiley, 2006. 64

[62] M. Balcerzyk, M. Moszynski, M. Kapusta, D. Wolski, J. Pawelke, and C.L. Melcher. Yso, lso, gso and lgso. a study of energy resolution and nonproportionality. *IEEE Transactions on Nuclear Science*, 47(4):1319–1323, 2000. 69

[63] Hiyori Kumagai, Takeo Ohnishi, Naoki Fukuda, H. Takeda, D. Kameda, N. Inabe, K. Yoshida, and Tomoha Kubo. Development of parallel plate avalanche counter ppac for bigrips fragment separator. *Nuclear Instruments and Methods in Physics Research B*, 317, 11 2013. 76

[64] K. Kimura, T. Izumikawa, R. Koyama, T. Ohnishi, T. Ohtsubo, A. Ozawa, W. Shinozaki, T. Suzuki, M. Takahashi, I. Tanihata, T. Yamaguchi, and Y. Yamaguchi. High-rate particle identification of high-energy heavy ions using a tilted electrode gas ionization chamber. *Nuclear Instruments and Methods in Physics Research Section A: Accelerators, Spectrometers, Detectors and Associated Equipment*, 538(1):608–614, 2005. 78

[65] K. Miernik, K. P. Rykaczewski, R. Grzywacz, C. J. Gross, M. Madurga, D. Miller, D. W. Stracener, J. C. Batchelder, N. T. Brewer, A. Korgul, C. Mazzocchi, A. J. Mendez, Y. Liu, S. V. Paulauskas, J. A. Winger, M. Woli ńska Cichocka, and E. F. Zganjar. β-delayed neutron emission from ^{85}Ga. *Phys. Rev. C*, 97:054317, May 2018. 87

[66] K. Kolos, D. Verney, F. Ibrahim, F. Le Blanc, S. Franchoo, K. Sieja, F. Nowacki, C. Bonnin, M. Cheikh Mhamed, P. V. Cuong, F. Didierjean, G. Duchêne, S. Essabaa, G. Germogli, L. H. Khiem, C. Lau, I. Matea, M. Niikura, B. Roussière, I. Stefan, D. Testov, and J.-C. Thomas. Probing nuclear structures in the vicinity of ^{78}ni with β- and βn-decay spectroscopy of ^{84}ga. *Phys. Rev. C*, 88:047301, Oct 2013. 87

[67] S.V. Paulauskas, M. Madurga, R. Grzywacz, D. Miller, S. Padgett, and H. Tan. A digital data acquisition framework for the versatile array of neutron detectors at low energy (vandle). *Nuclear Instruments and Methods in Physics Research Section A: Accelerators, Spectrometers, Detectors and Associated Equipment*, 737:22–28, 2014. 93

[68] Zach Meisel, C.R. Brune, S.M. Grimes, D.C. Ingram, T.N. Massey, and A.V. Voinov. The edwards accelerator laboratory at ohio university. *Physics Procedia*, 90:448454, 2017. 102

[69] Z. Y. Xu, S. Nishimura, G. Lorusso, F. Browne, P. Doornenbal, G. Gey, H.-S. Jung, Z. Li, M. Niikura, P.-A. Söderström, T. Sumikama, J. Taprogge, Zs. Vajta, H. Watanabe, J. Wu, A. Yagi, K. Yoshinaga, H. Baba, S. Franchoo, T. Isobe, P. R. John, I. Kojouharov, S. Kubono, N. Kurz, I. Matea, K. Matsui, D. Mengoni, P. Morfouace, D. R. Napoli, F. Naqvi, H. Nishibata, A. Odahara, E. Şahin, H. Sakurai, H. Schaffner, I. G. Stefan, D. Suzuki, R. Taniuchi, and V. Werner. β-decay half-lives of ^{76,77}Co, ^{79,80}Ni, and ^{81}Cu: Experimental indication of a doubly magic ^{78}Ni. *Phys. Rev. Lett.*, 113:032505, Jul 2014. 111, 114, 118

[70] P. Hosmer, H. Schatz, A. Aprahamian, O. Arndt, R. R. C. Clement, A. Estrade, K. Farouqi, K.-L. Kratz, S. N. Liddick, A. F. Lisetskiy, P. F. Mantica, P. Möller, W. F. Mueller, F. Montes, A. C. Morton, M. Ouellette, E. Pellegrini, J. Pereira, B. Pfeiffer, P. Reeder, P. Santi, M. Steiner, A. Stolz, B. E. Tomlin, W. B. Walters, and A. Wöhr. Half-lives and branchings for β-delayed neutron emission for neutron-rich co–cu isotopes in the r-process. *Phys. Rev. C*, 82:025806, Aug 2010. 111, 114

[71] M. Wang, G. Audi, A.H. Wapstra, F.G. Kondev, M. MacCormick, X. Xu, and B. Pfeiffer. The ame2012 atomic mass evaluation. *Chinese Physics C*, 36(12):1603–2014, dec 2012. 114, 118

[72] M. Pomorski, M. Pfützner, W. Dominik, R. Grzywacz, T. Baumann, J. S. Berryman, H. Czyrkowski, R. Dabrowski, T. Ginter, J. Johnson, G. Kamiński, A. Kuźniak, N. Larson, S. N. Liddick, M. Madurga, C. Mazzocchi, S. Mianowski, K. Miernik, D. Miller, S. Paulauskas, J. Pereira, K. P. Rykaczewski, A. Stolz, and S. Suchyta. First observation of two-proton radioactivity in ^{48}Ni. *Phys. Rev. C*, 83:061303, Jun 2011. 126

[73] M. Wang, G. Audi, A. H. Wapstra, F. G. Kondev, M. MacCormick, X. Xu, and B. Pfeiffer. The ame2012 atomic mass evaluation (ii). tables, graphs and references. *Chin.Phys.C*, 36:1603, 2012. 126

[74] P. gysbers and g. hagen and j.d. holt and g.r. jansen and t.d. morris and p. navrtil and t. papenbrock and s. quaglioni and a. schwenk and s. r. stroberg and k.a. wendt. *Nature Physics*, 15(5), 2019. 126

[75] Meng Wang, G. Audi, F. G. Kondev, W.J. Huang, S. Naimi, and Xing Xu. The AME2016 atomic mass evaluation (II). tables, graphs and references. *Chinese Physics C*, 41(3):030003, mar 2017. 126

[76] Morten Hjorth-Jensen, Thomas T.S. Kuo, and Eivind Osnes. Realistic effective interactions for nuclear systems. *Physics Reports*, 261(3):125–270, 1995. 129, 132

[77] M. Woliska-Cichocka, K.P. Rykaczewski, A. Fijakowska, M. Karny, R.K. Grzywacz, C.J. Gross, J.W. Johnson, B.C. Rasco, and E.F. Zganjar. Modular total absorption spectrometer at the hribf (ornl, oak ridge). *Nuclear Data Sheets*, 120:22–25, 2014. 138

[78] Shin Okumura, Toshihiko Kawano, Patrick Jaffke, Patrick Talou, and Satoshi Chiba. 235u(n, f) independent fission product yield and isomeric ratio calculated with the statistical hauserfeshbach theory. *Journal of Nuclear Science and Technology*, 55(9):1009–1023, 2018. 138

[79] J. Heideman, D. Prez-Loureiro, R. Grzywacz, C.R. Thornsberry, J. Chan, L.H. Heilbronn, S.K. Neupane, K. Schmitt, M.M. Rajabali, A.R. Engelhardt, C.W. Howell, L.D. Mostella, J.S. Owens, S.C. Shadrick, E.E. Peters, A.P.D. Ramirez, S.W. Yates, and K. Vaigneur. Conceptual design and first results for a neutron detector with interaction localization capabilities. *Nuclear Instruments and Methods in Physics Research Section A: Accelerators, Spectrometers, Detectors and Associated Equipment*, 946:162528, 2019. 138

[80] S. Neupane, J. Heideman, R. Grzywacz, J. Hooker, K.L. Jones, N. Kitamura, C.R. Thornsberry, L.H. Heilbronn, M.M. Rajabali, Y. Alberty-Jones, J. Derkin, T.N. Massey, and D. Soltesz. Neutron detection efficiency of the neutron detector with xn tracking (next). *Nuclear Instruments and Methods in Physics Research Section A: Accelerators, Spectrometers, Detectors and Associated Equipment*, 1020:165881, 2021. 138

Vita

Maninder Singh was born on April 1, 1992, in Karnal, India. He completed his primary and secondary education in his hometown in 2009. He got accepted at the University of Delhi, India, for a Bachelor in Physics with Honors program, completed in 2012. He continued his education at the University of Delhi with a Master in Physics, completed in the winter of 2014. He gained theoretical knowledge of basic concepts of Physics and Astronomy with his education in India. He, later on, got the opportunity to work as a researcher at the Indian Institute of Astrophysics (IIA) located in Bengaluru, India, in 2015. He later on got acceptance at the University of Tennessee, Knoxville, for a Ph.D. program in the Physics Department. He completed his Ph.D. under the supervision of Prof. Robert K. Grzywacz with a focus on studying the beta decay of exotic isotopes in Spring 2022. He continued his academic and research endeavors with a postdoctoral fellowship at Los Alamos National Laboratory, USA.